

































## EPOCHS IV: SED Modelling Assumptions and their impact on the Stellar Mass Function at $6.5 \leq z \leq 13.5$ using PEARLS and public JWST observations

THOMAS HARVEY <sup>1</sup>, CHRISTOPHER J. CONSELICE <sup>1</sup>, NATHAN J. ADAMS <sup>1</sup>, DUNCAN AUSTIN <sup>1</sup>,  
IGNAS JUODŽBALIS <sup>1,2</sup>, JAMES TRUSSLER <sup>1</sup>, QIONG LI <sup>1</sup>, KATHERINE ORMEROD <sup>1,3</sup>, LEONARDO FERREIRA <sup>4</sup>,  
QIAO DUAN<sup>1</sup>, LEWI WESTCOTT<sup>1</sup>, HONOR HARRIS<sup>1</sup>, RACHANA BHATAWDEKAR <sup>5</sup>, DAN COE <sup>6</sup>, SETH H. COHEN <sup>7</sup>,  
JOSEPH CARUANA <sup>8</sup>, CHENG CHENG <sup>9,10</sup>, SIMON P. DRIVER <sup>11</sup>, BRENDA FRYE <sup>12</sup>, LUKAS J. FURTAK <sup>13</sup>,  
NORMAN A. GROGIN <sup>14</sup>, NIMISH P. HATHI <sup>14</sup>, BENNE W. HOLWERDA <sup>15</sup>, ROLF A. JANSEN <sup>7</sup>,  
ANTON M. KOEKEMOER <sup>14</sup>, CHRISTOPHER C. LOVELL <sup>16</sup>, MADELINE A. MARSHALL <sup>17</sup>, MARIO NONINO <sup>18</sup>,  
IAN SMAIL <sup>19</sup>, ASWIN P. VIJAYAN <sup>20,21,22</sup>, STEPHEN M. WILKINS <sup>21</sup>, ROGIER WINDHORST <sup>7</sup>,  
CHRISTOPHER N. A. WILLMER <sup>23</sup>, HAOJING YAN <sup>24</sup>, AND ADI ZITRIN <sup>25</sup>

<sup>1</sup>Jodrell Bank Centre for Astrophysics, University of Manchester, Oxford Road, Manchester M13 9PL, UK

<sup>2</sup>Kavli Institute for Cosmology, University of Cambridge, Cambridge, Madingley Road, Cambridge, CB3 0HA

<sup>3</sup>Astrophysics Research Institute, Liverpool John Moores University, 146 Brownlow Hill, Liverpool, L3 5RF

<sup>4</sup>Department of Physics & Astronomy, University of Victoria, Finnerty Road, Victoria, British Columbia, V8P 1A1, Canada

<sup>5</sup>European Space Agency (ESA), European Space Astronomy Centre (ESAC), Camino Bajo del Castillo s/n, 28692 Villanueva de la Cañada, Madrid, Spain

<sup>6</sup>AURA for the European Space Agency (ESA), Space Telescope Science Institute, 3700 San Martin Drive, Baltimore, MD 21218, USA

<sup>7</sup>School of Earth and Space Exploration, Arizona State University, Tempe, AZ 85287-1404

<sup>8</sup>Department of Physics, University of Malta, Msida MSD 2080, Malta; & Institute of Space Sciences & Astronomy, University of Malta, Msida MSD 2080, Malta

<sup>9</sup>Chinese Academy of Sciences South America Center for Astronomy, National Astronomical Observatories, CAS, Beijing 100101, People's Republic of China

<sup>10</sup>2 CAS Key Laboratory of Optical Astronomy, National Astronomical Observatories, Chinese Academy of Sciences, Beijing 100101, People's Republic of China

<sup>11</sup>International Centre for Radio Astronomy Research (ICRAR) and the International Space Centre (ISC), The University of Western Australia, M468, 35 Stirling Highway, Crawley, WA 6009, Australia

<sup>12</sup>University of Arizona, Department of Astronomy/Steward Observatory, 933 N Cherry Ave, Tucson, AZ85721

<sup>13</sup>Physics Department, Ben-Gurion University of the Negev, P. O. Box 653, Be'er-Sheva, 8410501, Israel

<sup>14</sup>Space Telescope Science Institute, 3700 San Martin Drive, Baltimore, MD 21218, USA

<sup>15</sup>Department of Physics and Astronomy, University of Louisville, 102 Natural Sciences Building, Louisville, KY 40292, USA

<sup>16</sup>Institute of Cosmology and Gravitation, University of Portsmouth, Burnaby Road, Portsmouth, PO1 3FX, UK

<sup>17</sup>National Research Council of Canada, Herzberg Astronomy & Astrophysics Research Centre, 5071 West Saanich Road, Victoria, BC V9E 2E7, Canada; & ARC Centre of Excellence for All Sky Astrophysics in 3 Dimensions (ASTRO 3D), Australia

<sup>18</sup>INAF-Osservatorio Astronomico di Trieste, Via Bazzoni 2, I-34124 Trieste, Italy

<sup>19</sup>Centre for Extragalactic Astronomy, Department of Physics, Durham University, South Road, Durham DH1 3LE, UK

<sup>20</sup>Cosmic Dawn Center (DAWN)

<sup>21</sup>Astronomy Centre, Department of Physics and Astronomy, University of Sussex, Brighton, BN1 9QH, UK

<sup>22</sup>DTU-Space, Technical University of Denmark, Elektrovej 327, DK-2800 Kgs. Lyngby, Denmark

<sup>23</sup>Steward Observatory, University of Arizona, 933 N Cherry Ave, Tucson, AZ, 85721-0009

<sup>24</sup>Department of Physics and Astronomy, University of Missouri, Columbia, MO 65211

<sup>25</sup>Department of Physics, Ben-Gurion University of the Negev, P.O. Box 653, Be'er-Sheva 84105, Israel

### ABSTRACT

We utilize deep JWST NIRCcam observations for the first direct constraints on the Galaxy Stellar Mass Function (GSMF) at  $z > 10$ . Our EPOCHS v1 sample includes 1120 galaxy candidates at  $6.5 < z < 13.5$  taken from a consistent reduction and analysis of publicly available deep JWST NIRCcam data covering the PEARLS, CEERS, GLASS, JADES GOOD-S, NGDEEP, and SMACS0723 surveys, totalling 187 arcmin<sup>2</sup>. We investigate the impact of SED fitting methods, assumed star formation histories (SFH), dust laws, and priors on galaxy masses and the resultant GSMF. Whilst our fiducial GSMF agrees with the literature at  $z < 13.5$ , we find that the assumed SFH model has a large impact on the GSMF and stellar mass density (SMD), finding a 0.75 dex increase in the SMD at  $z = 10.5$  between

a flexible non-parametric and standard parametric SFH. Overall, we find a flatter SMD evolution at  $z \geq 9$  than some studies predict, suggesting a rapid buildup of stellar mass in the early Universe. We find no incompatibility between our results and those of standard cosmological models, as suggested previously, although the most massive galaxies may require a high star formation efficiency. We find that the ‘Little Red Dot’ galaxies dominate the  $z = 7$  GSMF at high-masses, necessitating a better understanding of the relative contributions of AGN and stellar emission. We show that assuming a theoretically motivated top-heavy IMF reduces stellar mass by 0.5 dex without affecting fit quality, but our results remain consistent with existing cosmological models with a standard IMF.

*Keywords:* galaxies: photometry, high-redshift, evolution, statistics

## 1. INTRODUCTION

The James Webb Space Telescope (JWST) has pushed backed the redshift frontier when searching for the earliest galaxies. The highly sensitive Near Infrared Camera (NIRCam) on JWST has led to an influx of high redshift galaxy candidates through photometry, in surveys such as CEERS, GLASS, PEARLS, NGDEEP & JADES (Adams et al. 2023; Castellano et al. 2022; Windhorst et al. 2023; Austin et al. 2023; Hainline et al. 2023; Bagley et al. 2023a). The wavelength coverage from 0.6 to  $5\mu\text{m}$ , enables identification of Lyman-break galaxies (LBGs) at redshifts  $z \geq 6.5$  by their photometry. In the first 18 months of science operations, tens of candidates above  $z \geq 10$  have been identified (Adams et al. 2023; Donnan et al. 2022; Atek et al. 2023; Naidu et al. 2022; Naidu et al. 2022; Harikane et al. 2023; Castellano et al. 2022; Finkelstein et al. 2023a; Austin et al. 2023; Hainline et al. 2023; Furtak et al. 2023; Labbé et al. 2023; Pérez-González et al. 2023; Finkelstein et al. 2023b; Leung et al. 2023; McLeod et al. 2023; Willott et al. 2023a), including a spectroscopically confirmed galaxy at  $z = 13.27$  (Curtis-Lake et al. 2023) and candidates at  $z \geq 16$  (e.g. Atek et al. 2023; Yan et al. 2023; Furtak et al. 2023; Hainline et al. 2023).

An immediate result was a potential overabundance of high-redshift galaxies compared to theoretical predictions and extrapolations of *Hubble Space Telescope* (HST)/*Spitzer* results (Naidu et al. 2022; Haslbauer et al. 2022; Mauerhofer & Dayal 2023; Mason et al. 2023). The mere existence of some of the galaxies at the inferred redshifts and stellar masses, ( $\geq 10^{10.5} M_{\odot}$  at  $z \geq 7.5$ ) seem to be in tension with standard  $\Lambda\text{CDM}$  cosmology given the small areas currently probed with JWST (Labbé et al. 2023; Lovell et al. 2023; Boylan-Kolchin 2023). However, spectroscopic observations of some of the highest-mass candidates in Labbé et al. (2023) have reduced their redshifts and stellar masses, or hinted at the presence of an Active Galactic Nuclei (AGN), and hence reduced possible  $\Lambda\text{CDM}$  tension (Kocovski et al. 2023; Fujimoto et al. 2022).

Initial overlap of galaxy candidates between independent studies was poor, but has since improved due to agreement on photometric calibration and reduction techniques (Adams et al. 2023; Rieke et al. 2022). Spectroscopic confirmation exists only for a fraction of potential candidates, but most spectroscopic programs have had a high success rate, along with a few notable low- $z$  interlopers (Robertson et al. 2023b; Curtis-Lake et al. 2023; Arrabal Haro et al. 2023; Tang et al. 2023; Laseter et al. 2023; Fujimoto et al. 2023; Bunker et al. 2023a; Wang et al. 2023a).

The combination of NIRCam’s high sensitivity and infrared (IR) wavelength coverage allows characterisation of the rest-frame optical emission of  $0.5 \leq z \leq 10$  galaxies, which is crucial for accurate stellar mass estimates. A more complete census of the high-redshift Universe is also possible, as galaxies without a strong Lyman-break (so called ‘HST-dark’ galaxies) were often missed in the Ultraviolet (UV) selected samples of pre-JWST studies (Pérez-González et al. 2023). Observations with Spitzer IRAC were available only for the brightest sources due to low sensitivity and angular resolution. Intrinsically UV-faint galaxies are often found to be dusty or evolved systems, and accurate characterisation of this population is essential when measuring the total buildup of stellar mass in the Universe, which is typically done by measuring the Galaxy Stellar Mass Function (GSMF).

Stellar masses are typically estimated from fitting spectral energy distributions to broadband photometry, and inferring a star formation history along with other physical parameters such as metallicity, dust obscuration and ionization state of the gas (e.g., Brinchmann & Ellis 2000; Bundy et al. 2006; Mortlock et al. 2011; Duncan et al. 2014; Mortlock et al. 2015; Grazian et al. 2015; Song et al. 2016; Bhatawdekar et al. 2019). This approach has generally been found to be reliable in the local Universe. At high-redshift there are a number of complicating factors that must be considered, which have different effects but overall act to increase the uncertainty in stellar masses beyond the statistical uncer-

tainty from the fitting (Lower et al. 2020; Wang et al. 2023b). There is a growing consensus that the star formation histories of many high- $z$  galaxies are stochastic and characterised by repeated cycles of a short burst of rapid star formation followed by a temporary period of quiescence (Faucher-Giguère 2018; Looser et al. 2023; Asada et al. 2023; Dressler et al. 2023; Dome et al. 2024). Young, bright stars created in the most recent bursts of star formation can dominate the spectral energy distributions of galaxies and obscure older populations, known as ‘outshining’ and lead to the stellar mass being underestimated by up to 1 dex (Giménez-Arteaga et al. 2023; Endsley et al. 2021; Pérez-González et al. 2023; Papovich et al. 2022; Jain et al. 2024; Giménez-Arteaga et al. 2024). For extremely stochastic SFHs, information loss of the first periods of star formation may occur, leading to large uncertainties in stellar mass (Narayanan et al. 2023; Shen et al. 2023; van Mierlo et al. 2023). Flexible ‘non-parametric’ SFHs, such as those presented in Leja et al. (2019); Tacchella et al. (2022); Robertson et al. (2023b), are able to reproduce these bursty SFHs more accurately at high- $z$ , typically finding systematically larger stellar masses, (Giménez-Arteaga et al. 2023; Jain et al. 2024), and may produce more reliable stellar mass estimates when compared to traditional parametric SFHs, which typically vary smoothly (Carnall et al. 2019, e.g. delayed exponential).

Another assumption is that of a possible universal initial mass function (IMF), which predicts the number of stars as a function of stellar mass (Salpeter 1955). The presence of low-mass stars, which dominate the stellar mass, is inferred entirely from the shape of the assumed IMF in most galaxies. A universal IMF (e.g. Salpeter 1955; Chabrier et al. 2000; Kroupa 2001), which is constant across time and space, has long been assumed in the majority of galaxy studies. Models of the physics of high- $z$  star formation suggest that it may have deviated from the universal IMF above redshift  $z = 8$  (Hopkins et al. 2005; Jermyn et al. 2018; Steinhardt et al. 2021, 2023). Low metallicity, high star formation rates, an increasing CMB temperature and high cosmic ray density could all contribute to heating of star formation regions and lead to a top-heavy IMF at high redshift (Gunawardhana et al. 2011; Clauwens et al. 2016; Papadopoulos et al. 2011). Observations of local elliptical galaxies have also found them to be inconsistent with the universal IMF, and instead find evidence for an IMF gradient, with evidence for a different IMF between younger and older stellar populations (e.g. Weidner et al. 2013, & references therein). Studies such as Steinhardt et al. (2023); Sneppen et al. (2022); Woodrum et al. (2023)

have introduced temperature-dependent IMF models for use in SED-fitting, which can decrease stellar mass estimates by up to 1 dex at constant redshift. Constraining the IMF is extremely difficult, but recent studies are beginning to find possible evidence for a top-heavy IMF in the early Universe (e.g. Katz et al. 2022; Cameron et al. 2023; Mowla et al. 2024). Ultimate conclusions on this are however far from certain.

In the EPOCHS paper series we have presented an independent and consistent reduction of deep JWST observations from available GTO, GO and ERS data including the CEERS, GLASS, SMACS-0723, JADES and PEARLS fields. We found 1165 robust galaxy candidates above redshift  $z = 6.5$ , with a total area of 187 arcmin<sup>2</sup> (Conselice et al., in prep; Adams et al. 2023).

In this paper we present a detailed examination of the inferred physical parameters of our high-redshift sample, with a particular focus on the stellar mass of our galaxy candidates. We derive a galaxy stellar mass function at  $6.5 \leq z \leq 13.5$ , and estimate the stellar mass density in order to trace the buildup of stellar mass in the early Universe. Importantly, we explore the impact of some of the key assumptions used in deriving stellar masses at high redshifts, such as star formation histories and the IMF.

In § 2 we present a brief overview of the data products used in this work and detail our data reduction procedure. § 3 describes our process for catalogue creation and robust sample selection of high- $z$  galaxy candidates. We detail our SED-fitting procedure and the impact of different assumptions on the inferred properties of high- $z$  galaxies in § 4. In § 5 we use our stellar mass estimates to build on the UV luminosity function presented in Adams et al. (2023) and construct a galaxy stellar mass function at redshifts from  $6.5 \leq z \leq 13.5$ . We discuss our findings and make comparisons to the literature in § 6. Finally § 7 summarises the findings of this work and looks at possibilities for future studies.

We assume a standard  $\Lambda$ CDM cosmology with  $H_0 = 70 \text{ km s}^{-1} \text{ Mpc}^{-1}$ ,  $\Omega_M = 0.3$  and  $\Omega_\Lambda = 0.7$ . All magnitudes listed follow the AB magnitude system (Oke 1974; Oke & Gunn 1983). All stellar masses measured in this work use a Kroupa (2002) unless otherwise indicated.

## 2. PRODUCTS AND DATA REDUCTION

This section briefly details the JWST programs and data products used in this analysis. For further details on the fields used please see Austin et al. (2023), Adams et al. (2023) and Conselice et al. (in prep). Table 1 shows the available unmasked areas, JWST NIRCcam filters and  $5\sigma$  depths of each dataset used.

### 2.1. PEARLS

**Table 1.** Table showing the unmasked areas and depths of the observations used in this work. Depths are given at  $5\sigma$  in AB magnitudes, measured in  $0''.16$  radius apertures. Depths are calculated by placing non-overlapping apertures in empty regions of the image, as measured by the **SExtractor** segmentation maps and our image masks. The nearest 200 apertures are used to calculate the Normalised Mean Absolute Deviation (NMAD) to derive local depths for each individual source. Where depths are tiered across mosaics (e.g. HST Advanced Camera for Surveys Wide Field Channel (ACS/WFC) observations in the Hubble Ultra Deep Field (HUDF) Parallel 2) we have listed the depths and areas separately. The four spokes of the NEP-TDF and ten CEERS pointings have uniform depths (within 0.1 mags) with the exception of CEERS P9 which we list separately. Areas are given in arcmin<sup>2</sup> and measured from the mask to account for the masked areas of the image and unused cluster modules. Fields with a ‘\*’ indicate that we have excluded the NIRCam module containing a lensing cluster from our analysis.

Field	Area (arcmin <sup>2</sup> )	HST/ACS_WFC		JWST/NIRCam								
		F606W	F814W	F090W	F115W	F150W	F200W	F277W	F335M	F356W	F410M	F444W
NEP	57.32	28.74	-	28.50	28.50	28.50	28.65	29.15	-	29.30	28.55	28.95
El Gordo*	3.90	-	-	28.23	28.25	28.18	28.43	28.96	-	29.02	28.45	28.83
MACS-0416*	12.3	-	-	28.67	28.62	28.49	28.64	29.16	-	29.33	28.74	29.07
CLIO*	4.00	-	-	28.12	-	28.07	28.21	28.675	-	28.91	-	28.71
CEERS	66.40	28.6	28.30	-	28.70	28.60	28.89	29.20	-	29.30	28.50	28.85
CEERSP9	6.08	28.31	28.32	-	29.02	28.55	28.78	29.20	-	29.22	28.50	29.12
SMACS-0723*	4.31	-	-	28.75	-	28.81	28.95	29.45	-	29.55	-	29.28
GLASS	9.76	-	-	29.14	29.11	28.86	29.03	29.55	-	29.61	-	29.84
NGDEEP HST-S	1.28	29.20	28.80	-	29.78	29.52	29.48	30.28	-	30.22	-	30.22
NGDEEP HST-D	4.03	30.30	30.95	-	29.78	29.52	29.48	30.28	-	30.22	-	30.22
JADES Deep GS	22.98	29.07	-	29.58	29.78	29.68	29.72	30.21	29.58	30.17	29.64	29.99

We incorporate NIRCam observations from the proprietary GTO survey *Prime Extragalactic Areas for Reionization Science* (PEARLS, PI: R. Windhorst & H.Hammel, PID: 1176 & 2738, [Windhorst et al. 2023](#)). We use observations of three fields targeting gravitationally lensed clusters, and one blank field consisting of a mosaic of 8 JWST NIRCam pointings. The gravitationally lensed clusters consist of MACS J0416.1-2403 (hereafter referred to as MACS-0416), El Gordo ([Menanteau et al. 2012](#),  $z \sim 0.87$ , ACT-CL J0102-4915 in the Atacama Cosmology survey, []) and Clio ( $z \sim 0.42$ , Designation GAMA100050 in the GAMA Galaxy Group Catalog v6+, [Robotham et al. 2011](#)). El Gordo and Clio have been visited once with JWST/NIRCam, with the cluster centered in one NIRCam module and the other observing a neighbouring blank field  $\sim 3'$  away ([Griffiths et al. 2018](#)). MACS-0416 has been observed 3 times, resulting in 3 separate parallel observations at different position angles. The PEARLS blank field is the North Ecliptic Pole Time Domain Field ([Jansen & Windhorst 2018](#), (NEP-TDF)). The NEP-TDF is positioned so it can be observed throughout the year, making it ideal for time-domain science and constructing a large deep field. Observations of the NEP-TDF consist of four pairs of overlapping NIRCam pointings (8 pointings total), with each of these four pairs orientated at 90 degree intervals like spokes on a windmill. NIRCam observations of the NEP-TDF, El Gordo and MACS0416 use the standard 8 photometric bands; F090W, F115W,

F150W, F200W, F277W, F356W, F410M and F444W. Clio uses 6 of the 8 previous bands, but lacks F115W and F410M. Within the NEP-TDF field we incorporate HST Advanced Camera for Surveys Wide Field Channel (ACS/WFC) imaging in the F606W filter, collected as part of the GO-15278 (PI: R. Jansen) and GO-16252/16793 (PIs: R. Jansen & N. Grogin) between October 1 2017 and October 31 2022. Mosaics of these data, astrometrically aligned to Gaia/DR3 and resampled on  $0''.03$  pixels, were made available pre-publication by R. Jansen & R. O’Brien (private comm. [O’Brien et al. 2024](#)). For full details of the PEARLS program please see [Windhorst et al. \(2023\)](#).

## 2.2. ERS and GO Data

We incorporate Early Release Science (ERS) and public General Observer (GO) data from SMACS-0723 (PID: 2736, PI: K. Pontoppidan, [Pontoppidan et al. 2022](#)), the *Cosmic Evolution Early Release Science Survey* (CEERS, PID: 1345, PI: S. Finkelstein, see also [Bagley et al. 2023b](#)), the *Grism Lens Amplified Survey from Space* survey (GLASS, PID: 1324, PI: T. Treu, [Treu et al. 2022](#)) and the *Next Generation Deep Extragalactic Exploratory Public Survey* (NGDEEP, PID: 2079, PIs: S. Finkelstein, Papovich and Pirzkal, [Bagley et al. 2023a](#)). We incorporate HST ACS/WFC observations of the Extended Groth Strip (EGS [Davis et al. 2007](#)) into our CEERS dataset in the F606W and F814W filters. This was obtained as part of the *Cos-*

*mic Assembly Near-infrared Deep Extragalactic Legacy Survey* (CANDELS, Grogin et al. 2011; Koekemoer et al. 2011), with updated astrometric alignment to Gaia EDR3 (Brown et al. 2021) by the CEERS team<sup>1</sup> and released as *Hubble Data Release 1*. The addition of these observations compensates for the lack of F090W observations in the CEERS survey.

We also incorporate NIRC*am* imaging of the *Great Observatories Origins Deep Survey South* (GOODS-South) field collected as part of *JWST Advanced Deep Extragalactic Survey* (JADES, PID:1180, PI: D. Eisenstein, Eisenstein et al. 2023a) and released publicly as JADES DR1 (Rieke et al. 2023). In the JADES and NGDEEP fields, which lie on the GOODS-South footprint, we add in existing HST data from F606W and F814W from the most recent mosaic (v2.5) from the Hubble Legacy Fields team (Illingworth et al. 2016; Whitaker et al. 2019).

### 2.3. JWST NIRC*am* Data Reduction

We have uniformly reprocessed all lower-level JWST data products following our modified version of the official JWST pipeline. This is a similar process to that used in Ferreira et al. (2022), Adams et al. (2023), Austin et al. (2023), and in particular Adams et al. (2023) but with updates based on new flat-fielding and techniques for dealing with NIRC*am* imaging artefacts.

We use version 1.8.2 of the official STScI JWST Pipeline<sup>2</sup> (Bushouse et al. 2022) and Calibration Reference Data System (CRDS) v1084, which contains the most up-to-date NIRC*am* calibrations at the time of writing and includes updated flat-field templates for the LW detectors, resulting in improved average depths across a single pointing of  $\sim 0.2$  dex in F444W. Next we subtract templates of wisps, artefacts present in the F150W and F200W imaging, between stage 1 and stage 2 of the pipeline. After stage 2 of the pipeline, we apply the  $1/f$  noise correction derived by Chris Willott<sup>3</sup>, which removes linear features caused by read-noise from the images. We do not use the sky subtraction step included in stage 3 of the pipeline, instead performing background subtraction on individual NIRC*am* frames between stage 2 and stage 3 (‘cal.fits’ files), consisting of an initial uniform background subtraction followed by a 2-dimensional background subtraction using `photutils` (Bradley et al. 2022). This allows for quicker assessment of the background subtraction performance and immediate fine-tuning of configuration parameters. After stage

3 of the pipeline, we align the final F444W image onto a Gaia-derived World Coordinate System (WCS) (Gaia Collaboration et al. 2018; Vallenari et al. 2022) using `tweakreg`, part of the DrizzlePac python package<sup>4</sup>, and then match all remaining filters to this derived WCS, ensuring the individual images are aligned to one another. In some cases (NEP, CEERS), we match to a WCS-frame derived from other space or ground based imaging with a larger FOV, given the low number of Gaia stars in some individual NIRC*am* pointings. We then pixel-match the images to the F444W image with the use of `astropy`, `reproject` (Astropy Collaboration et al. 2013, 2022a; Hoffmann et al. 2021).<sup>5</sup> The final resolution of the drizzled images is  $0''.03/\text{pixel}$ . Comparison of our reduction to the official PEARLS reduction pipeline (Windhorst et al. 2023) is given in Adams et al. (2023), finding excellent agreement in both observed fluxes (within 0.03 (0.01) magnitudes in the blue (red) NIRC*am* photometric filters) and astrometry (within 2 pixels ( $0''.07$ )).

## 3. CATALOGUE CREATION AND SAMPLE SELECTION

Full details of our catalogue creation and sample selection pipeline, called `GALFIND`, is available in Conselice et. al. (in prep). We briefly summarise the procedure used here.

### 3.1. Catalogue Creation

We use the code `SExtractor` (Bertin & Arnouts 1996) for source identification and photometric measurements. We use an inverse-variance weighted stack of the NIRC*am* F277W, F356W and F444W images for source detection in order to reliably identify faint sources and then carry out forced aperture photometry in all photometric bands. This photometry is calculated within  $0.32$  arcsecond diameter circular apertures, correcting for the aperture size with an aperture correction derived from simulated `WebbPSF` point spread functions (PSFs) for each band used (Perrin et al. 2012, 2014). This diameter was chosen to enclose the central/brightest 70 – 80 per cent of the flux of a point source without a large amount of contamination from neighbouring sources. This reduces the reliance on a potentially uncertain PSF model whilst still using the brightest pixels when calculating fluxes.

As `SExtractor` requires all images to be on the same pixel grid, for aligned HST imaging on a different pixel

<sup>1</sup> <https://ceers.github.io/hdr1.html>

<sup>2</sup> <https://github.com/spacetelescope/jwst>

<sup>3</sup> <https://github.com/chriswillott/jwst>

<sup>4</sup> <https://github.com/spacetelescope/drizzlepac>

<sup>5</sup> <https://reproject.readthedocs.io/en/stable/>

grid we use `photutils` to perform forced aperture photometry in the same diameter apertures (Bradley et al. 2022).

We next produce masks for our images by eye to cover diffraction spikes, any remaining snowballs, the cross pattern between SW detectors, image edges (including a  $\sim 50 - 100$  pixel border around detector edges) and any large foreground galaxies. The total amount of unmasked area used in this study is listed alongside the average  $5\sigma$  depths of each field in Table 1.

Following the generation of source catalogues and segmentation maps for each image, we calculate local depths for each source in each filter. This accounts for variation in background and noise across the image. Apertures of  $0''.32$  diameter are placed in empty regions of the image, as calculated from the segmentation map to be  $\geq 1''$  from the nearest source. For each source the nearest 200 apertures are used to calculate the Normalised Mean Absolute Deviation (NMAD) of the fluxes measured in the apertures, which corresponds to the  $1\sigma$  flux uncertainty. We convert this to a  $5\sigma$  depth, displaying the average depth in AB magnitudes for each field in Table 1. Where fields consist of mosaics of multiple pointings we display the average depth across the entire field, but we note that 9/10 CEERS pointings and 4/4 NEP-TDF have depths consistent within 0.1 magnitudes. The exception in CEERS is pointing 9 (P9), which has an additional exposure in F115W and F444W resulting in increased depths of  $\sim 0.2$  mags (Adams et al. 2023). Due to correlated noise, the flux uncertainties calculated by `SExtractor` are underestimated (Schlawin et al. 2020). We replace these uncertainty estimates with the local-depth derived flux errors (Adams et al. 2023).

### 3.2. Sample Selection

To select a sample of high-redshift galaxies we introduce selection criteria based primarily on photometric SED-fitting with `EAZY-py` (Brammer et al. 2008). We aim to select a robust sample of galaxies above  $z \geq 6.5$ , where the Lyman break is within the NIRCcam F090W filter.

We use the default `EAZY` templates (tweak\_fps.QSF.12.v3), along with Set 1 and Set 4 of the SED templates generated by Larson et al. (2022). These additional templates were developed to have bluer rest-frame UV colors than the default templates, as well as stronger emission lines, both of which have been observed in high-redshift galaxies (Finkelstein et al. 2022; Nanayakkara et al. 2022; Cullen et al. 2023; Withers et al. 2023). These templates have young stellar populations, low metallicities and active star formation.

Larson et al. (2022) has shown that they improve the accuracy of photo- $z$  estimates at high redshift.

We run `EAZY-py` initially with a uniform redshift prior of  $0 \leq z \leq 25$ , but then repeat the fitting with a reduced upper redshift limit of  $z \leq 6$ . This allows us to compare the goodness of fit of both a high and low-redshift solution for all galaxies in our sample. We use a minimum flux uncertainty of 10% to account for uncertainties in flux calibrations and aperture corrections (Rieke et al. 2022), as well as potential differences between the synthetic templates and our galaxies.

For reproducibility our selection criteria are designed to be based as much as possible on specific cuts in computed quantities, rather than individual inspection of candidates which can introduce hard to measure bias and incompleteness. To ensure robustness in our sample, our final selection criteria includes a visual review of the cutouts and SED-fitting solutions for all sources by authors TH, DA, NA, & QL but we reject less than 5% of our original sample by eye at this stage, which is much lower than comparable studies (reaching  $\geq 50\%$  in some cases, e.g. Hainline et al. 2023).

Our selection criteria for robust high redshift galaxies are as follows.

1. We require that the bandpass of the lowest wavelength photometric band must be entirely below the Lyman break, given the primary photo- $z$  solution. This sets a lower limit of  $z \approx 6.5$  in most of our fields.
2. We require a  $\leq 3\sigma$  detection in band(s) blueward of the Lyman break.
3. We require a  $\geq 5\sigma$  detection in the 2 bands directly redward of the Lyman break, and  $\geq 2\sigma$  detection in all other redward bands, excluding observations in NIRCcam medium-bands (e.g. F335M, F410M). If the galaxy appears only in the long wavelength NIRCcam photometry (i.e. a F200W or higher dropout), we increase the requirement on the 1st band to  $7\sigma$  detection.
4. The integral of the photo- $z$  PDF is required to satisfy  $\int_{0.90 \times z_{phot}}^{1.10 \times z_{phot}} P(z) dz \geq 0.6$  to ensure the majority of the redshift PDF is located within the primary peak, and that the peak is sufficiently narrow to provide a strong constraint on the redshift.  $z_{phot}$  refers to the redshift with maximum likelihood from the `EAZY-py` redshift posterior.
5. We require the best-fitting `EAZY-py` SED to satisfy  $\chi_{red}^2 < 3(6)$  to be classed as a robust (good) fit.

6. We require a difference of  $\Delta\chi^2 \geq 4$  between the high- $z$  and low- $z$  **EAZY-py** runs. This ensures that the high- $z$  solution is much more statistically probable.
7. If the half-light radius (**FLUX\_RADIUS** parameter in **SExtractor**) is smaller than the FWHM of the PSF in the F444W band, then we require that  $\Delta\chi^2 \geq 4$  between the best-fitting high- $z$  galaxy solution and the best-fitting brown dwarf template. This requirement is designed to remove Milky Way brown dwarf contaminants and is discussed further in § 5.2.2.
8. We require the 50% encircled flux radius from **SExtractor** to be  $\geq 1.5$  pixels in the long-wavelength wideband NIRCcam photometry (F277W, F356W, F444W). This avoids the selection of oversampled hot pixels in the LW detectors as F200W dropouts.

Given our requirement to observe the Lyman break, the lowest redshift at which we select ‘robust’ galaxies with NIRCcam photometry only is  $\sim 6.5$ , where the break falls within the NIRCcam F090W filter. In the fields where HST ACS/WFC imaging is available, we can robustly identify the Lyman break at lower redshifts.

Our selection criteria are similar to other high- $z$  galaxy studies, such as Hainline et al. (2023); Finkelstein et al. (2023a,b); Naidu et al. (2022); Castellano et al. (2022), who also fit galaxies using **EAZY-py**, and select their samples from the rest-UV SNR of their candidates and the resultant redshift PDF and  $\Delta\chi^2$  from the SED fitting. SNR requirements vary between studies, and are also somewhat dependent on the size of the extraction aperture used. Our  $0''.16$  radius apertures are larger than the  $0''.1$  radius apertures used in Finkelstein et al. (2023b), resulting in a number of their candidates being removed from our sample because they do not meet our  $5\sigma$  threshold, despite agreeing on the photo- $z$  solution. Other studies, such as Harikane et al. (2023); Yan et al. (2022), use a combination of color-color cuts and SED-fitting. A comprehensive comparison of the EPOCHS v1 galaxy sample to other studies is given in Appendix A of Adams et al. (2023).

Spectroscopy of high redshift galaxies with NIRSpec (e.g. Wang et al. 2023a; Fujimoto et al. 2023; Bunker et al. 2023a; Curtis-Lake et al. 2023) has shown that many high redshift galaxies have strong emission lines, with  $H\beta + [\text{OIII}]$  reaching observed equivalent widths of up to 2000-3000Å (Withers et al. 2023). For our photometric observations this can result in an excess in the band covering these emission lines of up to  $\sim 1$  dex. The emission line modelling in the SED fitting codes

used span only a limited parameter space in equivalent width and line ratios, so this can result in high  $\chi^2$  values even if the model is a good fit to the rest of the photometry. To avoid removing these galaxies from our sample we introduce a secondary group, referred to as ‘good’ galaxies, which have  $3 < \chi_r^2 < 6$  but meet the rest of our criteria. This applies to a very small fraction of our total sample, with only 23 galaxies meeting our other selection criteria but falling within this  $\chi^2$  range.

#### 4. GALAXY PROPERTIES FROM SED FITTING

The basic properties, redshift distribution, number counts and UVJ colors of the EPOCHS v1 sample are described in detail in Conselice et al. (in prep). The UV properties ( $M_{\text{UV}}$ ,  $\beta$  slopes) of this sample are explored in Austin et al. (in prep). The UV luminosity function is presented in Adams et al. (2023). Here we briefly summarise the basic statistics of the EPOCHS v1 sample, following the selection criteria described in § 3.2.

Across the fields described in § 2, 1214 galaxies pass our initial selection criteria with  $z \geq 6.5$  over a total unmasked area of 187.27 arcmin<sup>2</sup>, comprising one of the largest samples of high- $z$  JWST-selected galaxies. Our visual inspection removes 49 completely, leaving 1165 galaxies, which we refer to as the EPOCHS v1 sample. Of these 1165, 1054 are classed as ‘certain’ and 111 ‘uncertain’ by our visual inspection. In this work we choose to include the visually ‘uncertain’ candidates, in order to avoid potentially underestimating the stellar mass function. Filtering the sample to the  $6.5 < z < 13.5$  redshift range used in this work, our fiducial sample consists of 1120 galaxies.

The next sections detail the **Bagpipes** and **Prospector** SED fitting performed for all galaxies in the EPOCHS v1 sample. We perform this SED fitting only for our **EAZY-py**-selected sample. The purpose of this SED-fitting is to analyse the properties of the stellar and nebular components of these high- $z$  galaxies. We note that whilst the majority of galaxies in the EPOCHS v1 sample do not appear significantly extended beyond our **SExtractor** extraction aperture, all stellar masses quoted in the following results have been corrected by the ratio between the **SExtractor** *FLUX\_AUTO\_F444W* and the aperture corrected *FLUX\_APER\_F444W* fluxes, if it exceeded unity, to account for any residual flux outside the aperture. We use the longest wavelength band to correct stellar masses as this is most representative of the rest-frame optical emission.

##### 4.1. Bagpipes

**Bagpipes** (Bayesian Analysis of Galaxies for Physical Inference and Parameter ESTimation, Carnall et al.

2018, 2019)) is a Python package which uses Bayesian methods to fit galaxy SEDs to photometry. Our fiducial `Bagpipes` run uses the Bruzual & Charlot (2003) 2016 stellar population synthesis models, and a Kroupa (2001) IMF.

`Bagpipes` can construct and fit SEDs with a variety of SFH models, dust models and priors. We perform multiple fits for each galaxy in order to test the consistencies in derived galaxy parameters. For simplicity our approach is to define an initial ‘fiducial’ model, and then swap out individual model components or priors for other choices. Our model parameters, priors and hyper-parameters are detailed in Table 2. This is similar to the approach of Furtak et al. (2021), who define a reference model which is then compared to alternative models. In the rest of this section we further explain our choices of models and priors.

For the star formation history we test both parametric and non-parametric models, which have been shown to impact the stellar mass estimates (Leja et al. 2019; Tacchella et al. 2022). For our fiducial model, we use a parametric lognormal SFH which allows us to recreate the rising SFHs we expect in the early Universe. We compare this SFH with another commonly used parametrization, the delayed exponential. Details of the implementation of these parametric SFHs are available in Carnall et al. (2019). We also test a non-parametric ‘‘continuity’’ SFH model similar to the model added to `Prospector` in Leja et al. (2019). This SFH model fits the star formation rates in fixed time bins, with  $\Delta \log \text{SFR}$  between bins linked by a Student’s  $t$ -distribution. We recreate the methodology of Tacchella et al. (2022), by fitting both a ‘‘continuity’’ model, where the Student’s  $t$ -distribution has hyper-parameters  $\sigma = 0.3$  and  $\nu = 2$ , which weights against rapid changes in star formation rate, as well as a ‘‘continuity bursty’’ model, with  $\sigma = 1$  and  $\nu = 2$ , which allows more stochastic star formation, with rapid bursts and quenching more similar to the SFH inferred at high- $z$ . As is done in Tacchella et al. (2022) we fit 6 SFH bins for both models, with the first bin fixed to a lookback time of 0-10 Myr, the last bin ending at  $z = 20$ , and the other 4 bins are equally log-spaced in lookback time. Leja et al. (2019) showed that this model is relatively insensitive to the number of bins used, as long as the number exceeds 4. Like Tacchella et al. (2022), we assume there is no star formation at  $z > 20$  (Tacchella et al. 2022; Bowman et al. 2018; Jaacks et al. 2019). It is important to note that this model allows but does not require ‘bursty’ SFHs, and smooth or quenched SFHs are also possible if favoured during the fitting.

We include emission lines and nebular continuum based on `CLOUDY` v17.03 (Ferland et al. 2017). We regenerate `CLOUDY` models in order to probe a wider range of the ionisation parameter  $U$  between  $-3 \leq \log_{10} U \leq -1$  using a `CLOUDY` configuration file distributed with `Bagpipes`. For the ionization parameter we use a uniform prior (in log space).

We use the Calzetti et al. (2000) prescription for dust. Bowler et al. (2023) finds that UV-selected high- $z$  galaxies in the ALMA REBELS survey follow the local Calzetti-like  $\text{IRX}-\beta$  relation, so we do not fit a more complex dust law in our fiducial model. The allowed stellar metallicity ranges from  $-2.3 \leq \log_{10} Z_*/Z_\odot \leq 0.70$  with a logarithmic prior, as these galaxies are expected to have low metallicity, but theoretically could enrich their local environments quickly (Langeroodi et al. 2023; Curti et al. 2023).

In order to constrain the redshift parameter space we fix the redshift prior to the PDF from our `EAZY-py` SED-fitting, which we approximate as a Gaussian. The redshift prior draws are capped at  $\pm 3\sigma$ . We use the default sampling method, using the Python package `PyMultiNest` (Feroz et al. 2009; Buchner 2016).

#### 4.2. *Prospector*

In addition to our `Bagpipes` SED-fitting we also fit our sample using the `Prospector` package (Johnson et al. 2021) in order to compare the results of these two commonly used SED fitting tools. `Prospector` allows greater flexibility and control of model parameters than `Bagpipes` at the expense of computational time. `Prospector` uses Bayesian inference to determine galaxy stellar population properties and star formation histories. `Prospector` is built on Flexible Stellar Population Synthesis (FSPS, Conroy & Gunn 2010), using `python-fsps` (Johnson et al. 2023) and the Modules for Experiments in Stellar Astrophysics Isochrones and Stellar Tracks (MIST) stellar isochrones (Choi et al. 2016; Dotter 2016). `Prospector` allows for very flexible star formation histories, including the use of non-parametric SFHs, which have become increasingly popular in the JWST era. Non-parametric SFHs are modelled by splitting star-formation history into a number of temporal bins, with the SFH in each bin linked by a statistical distribution. We generally follow the prescription of Tacchella et al. (2022) for our `Prospector` model. We test both a traditional parametric star formation history as well as the ‘‘continuity bursty’’ non-parametric SFH used in `Bagpipes`. We allow the stellar mass to vary between  $6 \leq \log_{10} M/M_\odot \leq 12$  with a uniform logarithmic prior. For our parametric star formation history we use the ‘delayed- $\tau$ ’ model, where  $\text{SFR}(t) \propto (t - t_s)e^{-(t-t_s)\tau}$ .



**Table 2.** Summary of parameters, hyper-parameters and priors for our **Bagpipes** SED-fitting. The text color corresponds to a specific **Bagpipes** run, where black corresponds to our default ‘fiducial’ setting for each parameter. Parameters and priors for other iterations can be assumed to be the same as given for the ‘fiducial’ bagpipes run unless otherwise specified. The top section of the table lists parameters that are common to all of our **Bagpipes** models, whereas the lower section gives the model-specific parameters for each of our chosen configurations.

<b>Common Parameters</b>			
Parameter		Prior/Value (Min, Max)	Description
$z_{\text{phot}}$		<b>EAZY-py</b> Posterior PDF ( $\pm 3\sigma$ )	Redshift
SPS Model		<b>Bruzual &amp; Charlot (2003)</b> ; <b>BPASS v2.2.1</b>	Stellar population synthesis model
IMF		<b>Kroupa (2001)</b> ; <b>default BPASS IMF</b>	Stellar Initial Mass Function
Dust Law parametrization		<b>Calzetti et al. (2000)</b> ; <b>Salim et al. (2018)</b> <b>Charlot &amp; Fall (2000)</b>	Dust law
$A_V$		Log-uniform: ( $10^{-3}$ , 10); <b>uniform (0, 6)</b>	V-band attenuation (all stars)
SFH		lognormal; <b>“continuity bursty”</b> ; <b>delayed-<math>\tau</math></b>	Star formation history
$\log_{10}(M_*/M_\odot)$		uniform: (5, 12)	Surviving stellar mass
$Z_*/Z_\odot$		log-uniform: (0.005, 5); <b>uniform (0, 3)</b>	stellar metallicity
$Z_{\text{gas}}/Z_\odot$		Fixed to $Z_*$	gas-phase metallicity
$\log_{10} U$		uniform: (-3, -1)	Ionization Parameter
<b>Model Specific Parameters</b>			
Model	Parameter	Prior/Value (Min, Max)	Description
Fiducial	$t_{\text{max}}$	uniform: (10 Myr, 15 Gyr)	Age of Universe at peak SFR
	FWHM	uniform: (10 Myr, 15 Gyr)	FWHM of SFH
<b>delayed-<math>\tau</math> SFH</b>	$\tau$	uniform: (10 Myr, 15 Gyr)	e-folding timescale
	Age	log-uniform: (10 Myr, $t_{\text{univ}}(z_{\text{phot}})$ )	Time since SF began
<b>“continuity bursty” non-parametric SFH</b>	$N_{\text{bins}}$	6 bins (5 fitted parameters)	First bin 0 – 10 Myr, SF begins at $z = 20$ , others distributed equally in $\log_{10}$ lookback time
	$d_{\log_{10} \text{SFR}}$	Student’s-t: $\nu = 2, \sigma = 1.0$	Ratio of $\log_{10}\text{SFR}$ in adjacent bins, coupled by $\sigma$
<b>Charlot &amp; Fall (2000) Dust Law</b>	$n$	clipped normal: $\mu = 0.7, \sigma = 0.3$ (0.3, 2.5)	Power-law slope of attenuation curve ( $A \propto \lambda^{-n}$ ) For <b>Calzetti et al. (2000)</b> $n \approx 0.7$
	$\eta$	clipped normal: $\mu = 2, \sigma = 0.3$ (1, 3)	$A_{V, < 10\text{Myr}}/A_V$ ratio between young and old stars
<b>Salim et al. (2018) Dust Law</b>	$\delta$	clipped normal: $\mu = 0, \sigma = 0.1$ (-0.3, 0.3)	Deviation from <b>Calzetti et al. (2000)</b> slope
	$\beta$	uniform (0, 5)	Strength of 2175Å bump
<b>BPASS SPS Model</b>			No additional components
<b>Uniform <math>A_V</math> Prior</b>			No additional components
<b>Uniform <math>Z_*</math> Prior</b>			No additional components

We note that by default **Prospector** provides the total stellar mass formed, rather than the surviving stellar mass. Post-fitting we recalculate the return fraction within **Prospector** for the full posterior in order to derive a surviving stellar mass distribution for each galaxy. We allow the V-band optical attenuation due to dust to vary between 0 and 6 magnitudes, with a uniform prior,

assuming a **Calzetti et al. (2000)** law also used in our ‘fiducial’ **Bagpipes** run.

We model IGM attenuation following **Madau (1995)**. Following **Tacchella et al. (2022)** and due to possible line-of sight variations in the optical IGM attenuation, we allow the IGM opacity to vary with a clipped Gaussian prior distribution centered on 1, clipped at 0 and

2, and with a dispersion of 0.3. The stellar metallicity is allowed to vary between  $-4 \leq \log_{10} Z/Z_{\odot} \leq 0.16$  with a uniform prior. We do not link the gas-phase metallicity, which is also free to vary with the same range and prior. Gas-phase metallicity is expected to differ from stellar metallicity at some stages of galaxy evolution (e.g. following significant gas accretion into a galaxy, lowering gas-phase metallicity) and decoupling them permits more flexibility in the stellar and nebular emission line modelling.

We use a [Kroupa \(2001\)](#) IMF for consistency with our **Bagpipes** SED fitting, but as **Prospector** allows tabulated IMFs we also test the impact of a top-heavy IMF on the derived stellar masses. Top-heavy IMFs are predicted at high- $z$ , and there is preliminary evidence for a top-heavy IMF in extreme nebular dominated galaxies at high- $z$  ([Cameron et al. 2023](#)). The results for different choices of IMF are detailed in § 4.5.

We run **Prospector** using nested sampling with **dynesty** ([Speagle 2020](#)), using the default sampling settings with the exception of switching from uniform sampling to the more robust random walk, to efficiently probe the multi-dimensional parameter space. Since **Prospector** is computationally expensive to run, we fit only a subset of our galaxy sample, prioritising those galaxies which are high-redshift or massive. Specifically we fit all galaxies with  $z_{\text{phot}}$  (from **EAZY-py**) above  $z \geq 8.5$ , or with a fiducial **Bagpipes** stellar mass of  $\log_{10}(M_{\star}/M_{\odot}) \geq 9.0$ .

#### 4.3. Stellar Mass Comparisons

[Figure 1](#) shows a comparison of the derived galaxy properties of our fiducial **Bagpipes** run for all sources in our sample to our other **Bagpipes** results. The details of the models compared are shown in [Table 2](#). As discussed in § 4.1, we compare models with different priors, SPS models and SFH parametrizations. The top plot shows the systematic mass offset found when varying the dust law and priors, while the second row shows the same offset for parametric and non-parametric SFHs, as well as a BPASS SPS model ([Stanway & Eldridge 2018](#)). For each **Bagpipes** model we show the *Locally Weighted Scatterplot Smoothing* fit (LOWESS, [Cleveland 1979](#)). The LOWESS estimator is a non-parametric fitter for noisy data, and shows the overall trend between the mass discrepancy and fiducial stellar mass.

We allow the redshift to vary within the **EAZY-py** posterior PDF for each **Bagpipes** fit, resulting in only small changes in redshift between individual **Bagpipes** results. 99.6% of photo- $z$  estimates fall within 15% of our fiducial **Bagpipes** redshift.

In the following sections we compare the consistency of the derived stellar masses between our fiducial and alternative **Bagpipes** models, as shown in [Figure 1](#). We also include some limited discussion of other inferred galaxy properties, such as star formation rate, or dust content where they vary significantly from our fiducial model.

In [Figure 3](#) and [Figure 4](#) we show examples of the photometry, best-fitting **Bagpipes** & **Prospector** SEDs, and posterior redshift and stellar mass estimates for a selection of high-mass and or discrepant galaxies in our sample.

##### 4.3.1. Impact of Priors

The first comparison we make is a substitution of the default logarithmic prior on the V-band dust extinction,  $A_V$ , to a uniform prior. A uniform prior favors higher dust extinctions, and the largest difference to the fiducial model is seen in galaxies with  $A_{V, \text{fid}} < 0.2$  mag, where the dust content is poorly constrained. We see good agreement in photo- $z$ , along with a few extreme outliers, which is unsurprising given the informative redshift prior from **EAZY-py** we use. The stellar mass offset is shown in light blue in the top plot of [Figure 1](#) and shows good agreement within the posterior uncertainties. Galaxies with higher levels of dust are found to be significantly younger and more star-forming with a uniform dust prior, suggesting the inferred star formation histories are dependent on the dust prior. Comparison of the best-fitting  $\chi^2$  values shows that both models are equally well-fitted to the photometry.

We also test the impact of our metallicity prior, which is logarithmic in our fiducial **Bagpipes** model. This favours low metallicity, which we expect in the early Universe. Here we exchange this prior for a uniform distribution which favours higher metallicity, shown in orange in the top plot of [Figure 1](#). We see little overall impact on the stellar mass from the metallicity prior, with individual galaxies scattering up to 0.5 dex and the majority consistent with results from our fiducial **Bagpipes** run.

Overall the impact of the dust and metallicity priors alone appears to have only a small systematic effect on the derived galaxy masses. However, in a small number of individual cases masses can scatter by  $\sim 0.5$  dex with little difference in the goodness of fit.

##### 4.3.2. The Assumed Dust Law

Our fiducial **Bagpipes** model assumes a simple one-component [Calzetti et al. \(2000\)](#) dust law. The slope of the dust law is known to vary in some galaxies, and numerous alternative models (e.g. [Charlot & Fall 2000](#); [Salim et al. 2018](#)) including additional parameters

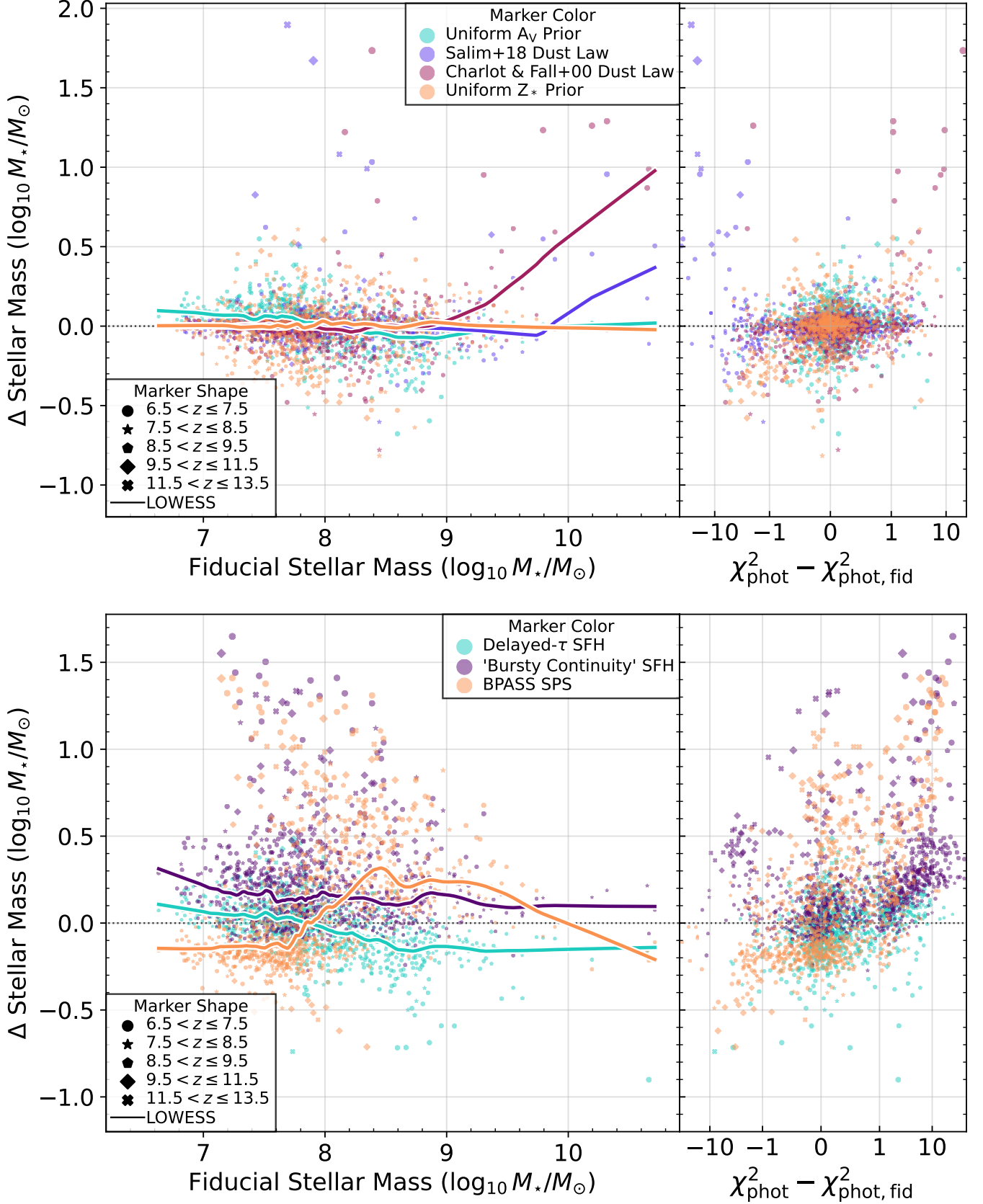


**Figure 1. Top)** Comparison of the observed stellar mass offset between our fiducial **Bagpipes** model and alternative models for the entire EPOCHS v1 sample, as a function of fiducial stellar mass. The alternative models considered vary priors on the metallicity and dust attenuation, as well as the assumed dust law. Marker shapes show the redshift bin for each galaxy, based on the fiducial redshift, and each **Bagpipes** model considered is shown in a different color. The colored lines show the *Locally Weighted Scatterplot Smoothing* fit (LOWESS, Cleveland 1979). The right-hand plots show the stellar mass offset as a function of  $\Delta\chi^2$ , between the two fits. **Bottom)** Same as the upper plot, but the alternative models vary the assumed star formation history or stellar population synthesis model instead.

have been suggested. Charlot & Fall (2000) fit a two-component dust law, with different amounts of extinction for young ( $\leq 10$  Myr) and old stellar populations, to account for dust in stellar birth clouds. The resultant deviations in stellar mass are shown in magenta in the top plot of Figure 1, with a significant deviation at the highest stellar masses, which can be seen in the LOWESS trend. For galaxies with a fiducial stellar mass of  $\geq 10^{10} M_{\odot}$ , the majority are found to have  $\geq 1$  dex larger stellar masses with the Charlot & Fall (2000) dust law. However for these galaxies the goodness of fit is considerably poorer, with  $\Delta\chi^2 \geq 10$  with the Charlot & Fall (2000) model.

Despite the same prior, the dust attenuation ( $A_V$ ) posteriors are quite different between the two models, due to the degeneracy between  $A_V$  and slope. Galaxies with moderate dust extinction in the fiducial results ( $\leq 1$  mag) are typically found to have very little dust extinction on the old stellar population, but the most dust-obscured galaxies ( $A_V > 2$ ) have significantly greater extinction ( $1.5\times$  more on average). The majority of galaxies favor a steeper slope ( $n$ ) for the attenuation power-law than given by Calzetti et al. (2000), in this mode with a distribution centered on  $n \approx 1.3$ , which is  $2\sigma$  from the prior value of 0.70.

Salim et al. (2018) allow a deviation in slope compared to the Calzetti et al. (2000) and an additional UV bump at 2175 Å. The UV bump in the Salim et al. (2018) model is driven primarily by Polycyclic Aromatic Hydrocarbon (PAH) emission, which is expected when emission is strongly reprocessed. We replace the Calzetti et al. (2000) dust law with the Salim et al. (2018) model, and fit for these additional components, as shown in Table 2. We find that the inferred stellar mass can increase by  $>1$  dex in some cases, particularly at the highest fiducial stellar mass, but the average offset (see the LOWESS fit in Figure 1) is smaller than for the Charlot & Fall (2000) case. In a number of cases the goodness of fit for the Salim et al. (2018) model is considerably better than our fiducial model, with  $\delta\chi^2 \leq -10$  in a number of galaxies.

#### 4.3.3. Comparison to ‘delayed’ SFH

To test the consistency of galaxy stellar mass estimates with different parametric star formation histories, we replace our ‘lognormal’ SFH with another commonly used SFH; a delayed- $\tau$  SFH. We find systematically slightly lower stellar masses above  $10^8 M_{\odot}$ , but reasonable agreement at the lowest stellar masses. This is likely due to the log-uniform prior on age used in the delayed- $\tau$  model, which results in a younger stellar population. Comparison of the goodness of fit via the  $\chi^2$

parameter suggests the models typically have slightly poorer fits than the fiducial model, but in some cases the stellar masses are reduced by  $\sim 0.5$  dex with very little impact on the goodness of fit.

#### 4.3.4. Comparison to ‘continuity bursty’ SFH

Here we replace our fiducial Bagpipes ‘lognormal’ SFH with a ‘continuity bursty’ SFH model described in detail in § 4.1. We reproduce the result of Tacchella et al. (2022) that this SFH increases the galaxy stellar mass, finding an average increase of 0.2 dex. The stellar mass discrepancy between the two models is shown in purple in the lower figure of 1. In individual cases the increase in stellar mass can reach  $\approx 1$  dex, with only small changes in photo- $z$ . The largest offsets in stellar mass are typically seen for galaxies with a fiducial stellar mass of  $10^8 M_{\odot}$ , with the highest fiducial stellar mass galaxies ( $\geq 10^{10} M_{\odot}$ ) seeing considerably smaller increases.

We see the largest discrepancies in stellar mass between the two models when the  $\chi^2$  significantly favours the fiducial model, suggesting the higher stellar mass estimate of the ‘continuity bursty’ model may not be accurate in these cases. However there are a small number of galaxies in which the offset exceeds 1 dex with minimal  $\chi^2$  difference, and even a few galaxies where the offset exceeds 0.5 dex and the ‘continuity bursty’ model is significantly preferred. An example of the discrepancy between the stellar mass PDFs of our fiducial and the ‘continuity bursty’ model can be seen for the individual galaxy SED of *JADES-Deep-GS:9075* shown in Figure 4, where there is a 1.3 dex difference between the stellar mass estimates, with only a difference of  $\Delta\chi^2$  between the two solutions.

Star-formation rates (SFRs) are typically higher, however the model does not reproduce the highest SFR estimates of the fiducial model. Individual inspection of these highly-star forming galaxies show that the ‘continuity bursty’ model struggles to reproduce SFRs high enough to match the measured  $H\beta+[OIII]$  equivalent widths inferred from the photometry. Despite the greater flexibility (and number of fitted parameters), the ‘continuity bursty’ model has a higher  $\chi^2$  than our fiducial model for the majority of galaxies. This may suggest that the fitting procedure is struggling to accurately constrain the SFH in the non-parametric case.

#### 4.3.5. Comparison to BPASS SPS Models

By default Bagpipes uses the 2016 version of Bruzual & Charlot (2003)’s (BC03) stellar population synthesis (SPS) models. However Bagpipes can also employ *Binary Population and Spectral Synthesis* (BPASS, Stanway & Eldridge 2018) models. Specifically we use mod-

els generated with v2.2.1 of BPASS, with the default IMF (slope of 1.35,  $300 M_{\star}$ ). The IMF parametrization of this SPS model differs slightly from the Kroupa (2001) IMF used in the BC03 models, causing an intrinsic offset in stellar mass. However as shown in orange in the lower plot of Figure 1, the comparison of the mass estimates is more complex. At the lowest and highest stellar masses ( $\log_{10} M_{\star}/M_{\odot} \leq 7.5$  and  $\log_{10} M_{\star}/M_{\odot} \geq 10$ ), we see systematically lower stellar masses than the fiducial **Bagpipes** model, which is what we would expect based the IMF difference alone. However for the majority of the sample, which falls between these two mass extremes, we see a significantly larger offset in stellar masses, which increases with redshift, as shown by the LOWESS trend.

The SFRs and redshifts are broadly correlated, with some outliers. However the ages show a large scatter, and higher mass-weighted ages (MWA) are preferred in the majority of cases when using BPASS, which may be more reasonable that the young ages ( $(\text{MWA}) \sim 20\text{Myr}$ ) inferred with our fiducial **Bagpipes** results. In particular, there are a significant subset of galaxies found to have a  $\geq 2$  dex shift in mass-weighted age.

The best-fit  $\chi^2$  shows some scatter, where fits with low  $\chi^2$  in the fiducial **Bagpipes** results typically having a similar or worse fit, but some galaxies with higher  $\chi^2$  having significantly improved. For these galaxies with improved  $\chi^2$  ( $\Delta\chi^2 > 5$ ), the main difference is that the best-fitting SED reproduces the observed rest-UV fluxes more closely. Interestingly, this subset of galaxies with significantly improved  $\chi^2$  also typically have considerably higher MWA using BPASS than BC03, with their recreated SFHs suggesting a constant SFH, rather than the recent burst preferred when fitting with the BC03 SPS models.

#### 4.3.6. Other Comparisons

Numerous other **Bagpipes** models were tested, and we have presented in detail the results of a subset of them above. Here we summarise the effects of a few other variations which we do not include in Figure 1.

1. Fixed redshift to **EAZY-py** max  $P(z)$ : Little overall effect on stellar masses or star formation rates, with some individual scatter. This is the expected behaviour as the majority of redshifts are consistent within the **EAZY-py** posterior uncertainty, given that we use this as a prior in our fiducial model.
2. “continuity” non-parametric SFH model’: This variation tests the other non-parametric SFH model introduced in Leja et al. (2019) and Tacchella et al. (2022), which more tightly constrains the SFR in neighbouring time bins to force more smoothly varying star forma-

tion histories than the “continuity bursty” model. We find overall similar behaviour to the “continuity bursty” model, with systematically higher masses and higher mass-weighted age. The models typically have worse  $\chi^2$  statistics than the “continuity bursty” model fits potentially indicating that more stochastic star formation histories are preferred for the majority of galaxies, as suggested in the literature (Faucher-Giguère 2018; Looser et al. 2023; Asada et al. 2023; Endsley et al. 2023a).

#### 4.4. Comparison to Prospector

In this section we compare our fiducial **Bagpipes** model to our results from **Prospector**. Figure 2 shows a comparison of the stellar masses derived from **Bagpipes** and **Prospector**. We compare our ‘fiducial’ **Bagpipes** model, as described in § 4.1, to our parametric SFH **Prospector** model. These models are generally similar with a few key differences, but both provide a baseline for comparison to our other models. We also compare our non-parametric SFH models to each other, which both employ the same “continuity bursty” SFH, with the same time bins and priors. We use the same Kroupa (2001) IMF for both **Bagpipes** and **Prospector**, so we do not expect any different in stellar mass estimates due to the IMF parametrization.

For the comparison of the parametric SFH models (delayed- $\tau$  for **Prospector**, lognormal for **Bagpipes**), we see systematically larger photo- $z$  and stellar mass estimates with **Prospector**. Whilst in the **Prospector** model we allow the IGM attenuation to vary, which could impact photo- $z$  estimates, we do not see the same offset with the non-parametric SFH model, where the IGM attenuation is also allowed to vary. Both SED-fitting tools are given the same redshift prior from **EAZY-py**. We can see for both example galaxy SEDs in Figure 4 that **Prospector** instead prefers higher- $z$  solutions than **Bagpipes** because it is inferring the presence of Lyman- $\alpha$  emission. Whilst Lyman- $\alpha$  emitters have been found at  $z \geq 9$  (e.g. Bunker et al. 2023b), we do not expect to observe Lyman- $\alpha$  from the majority of galaxies at these redshifts due to the attenuation from neutral hydrogen during the Epoch of Reionization, and a systematic photo- $z$  offset from **Prospector** is likely for galaxies without Lyman- $\alpha$  emission. However given that we see a photo- $z$  offset primarily for the ‘parametric SFH’ only, Lyman- $\alpha$  emission is unlikely to be the only cause of the offset as the **Prospector** SEDs in Figure 4 show Lyman- $\alpha$  emission for both SFH models. This offset will generally cause a slight increase in stellar mass estimates, as a more distant galaxy must be intrinsically brighter. We see a median increase of 0.43 dex in stellar mass.

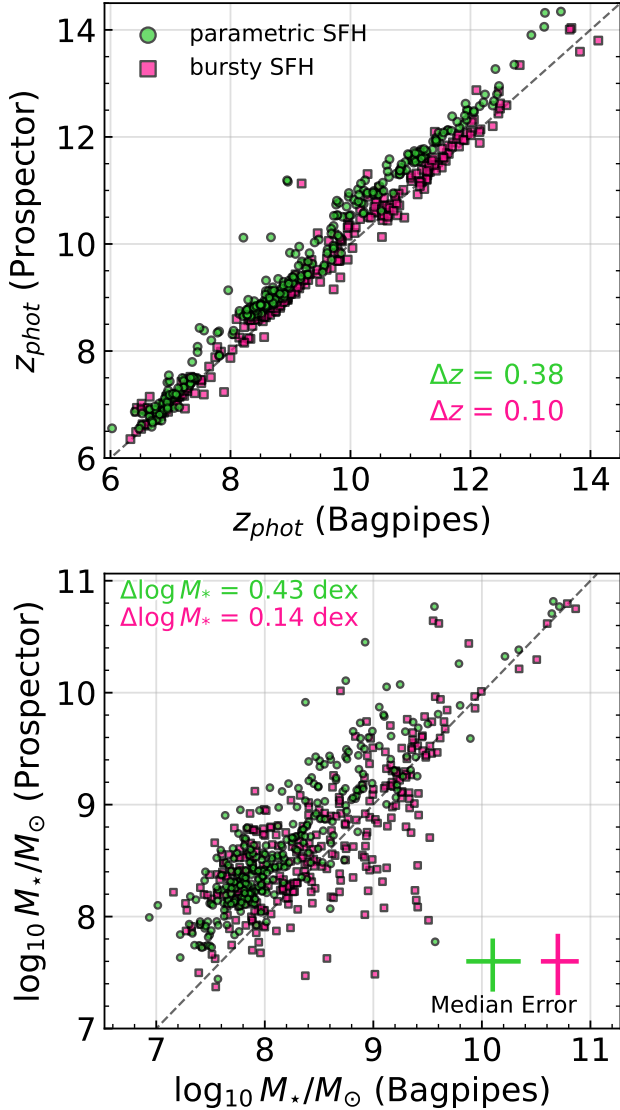


**Figure 2.** (top) Comparison of redshift estimates between Bagpipes and Prospector, both with the same Gaussian photo- $z$  prior from EAZY-py. Photo- $z$  estimates are systematically larger in Prospector when comparing the parametric SFH models. Median photo- $z$  offset for each model is shown on the plot. (bottom) Comparison of derived stellar mass estimates between Prospector and Bagpipes for both parametric and non-parametric SFH models. Median stellar mass offset is shown on the plot, as is the average uncertainty for both stellar mass estimates.

For the “continuity bursty” SFH models we see better agreement in redshift, with a median offset of only  $\delta z = 0.1$ . Stellar mass estimates are also more consistent on average, although we see large scatter, with individual mass differences reaching  $\approx 1.5$  dex.

We typically see comparable  $\chi^2$  for both the parametric and non-parametric Prospector SFH models, in contrast to the result with Bagpipes. It is possible that

the nested sampling with `dynesty` in Prospector provides a more robust constraint on the binned SFH than the nested sampling in Bagpipes, and may warrant further investigation.

#### 4.5. Top-heavy IMF

As discussed in § 1, one possibility to explain the high inferred stellar masses of high- $z$  galaxies is a ‘top heavy’ IMF, which results in the production of more high mass stars compared to a local IMF, and lowers the inferred mass-to-light ratios in high- $z$  galaxies. We use Prospector to investigate the impact of varying the initial mass function on the inferred stellar mass of a subset of the EPOCHS v1 sample. We implement the modified Kroupa (2001) IMF suggested by Steinhardt et al. (2023), which assumes a gas temperature evolution  $T_{gas} \propto (1+z)^2$ . We produce two modified IMFs, one with  $T_{gas} = 45\text{K}$ , which we use for  $8 \leq z \leq 12$ , and one with  $T_{gas} = 60\text{K}$ , which we use at  $z \geq 12$ . A standard Kroupa (2001) IMF would have  $T_{gas} = 20\text{K}$  in this parametrization, and given the broken-power-law shape this modification results in an increasingly top-heavy IMF with increasing gas temperature. Whilst it is theoretically possible to produce a unique IMF for each galaxy by assuming a  $z - T_{gas}$  relationship, we avoid doing this for simplicity. We otherwise leave unchanged the Prospector configuration in order to directly compare the impact of the IMF.

In Figure 5 we show the results of modifying the IMF on the stellar mass estimates. We compare the masses derived with a standard Kroupa (2001) IMF to the two modified IMF models, finding significant decreases in stellar mass with very little change in the quality of the fits. Noting that due to the computational intensity of Prospector fitting we only fit a subset of our full sample, and calculate the median decrease in mass for both SFH models and HOT IMFs. For the  $z > 12$  sample where we use the HOT 60K IMF we include our full parent sample, however for the  $z < 12$  model we fit only galaxies with either  $z \geq 8.5$  or fiducial Bagpipes stellar mass  $\log_{10} M_{*,\text{fid}} > 9.5$ . In terms of numbers, there are 221 galaxies in the HOT 45K IMF group, and 21 galaxies in the HOT IMF 60K group. Given that this IMF model is predicted to be applicable in the region of  $8 \leq z \leq 12$  (Steinhardt et al. 2023), and the lack of mass-dependence in our results, we do not expect the excluded lower mass galaxies at  $8 \leq z \leq 8.5$  to significantly impact our findings.

For the non-parametric “delayed” SFH model, we find a median decrease in stellar mass of 0.33 dex for the  $z \leq 12$  (HOT 45K IMF) galaxy sample. For the  $z \geq 12$  sample, we find a median decrease of 0.46 dex. For the

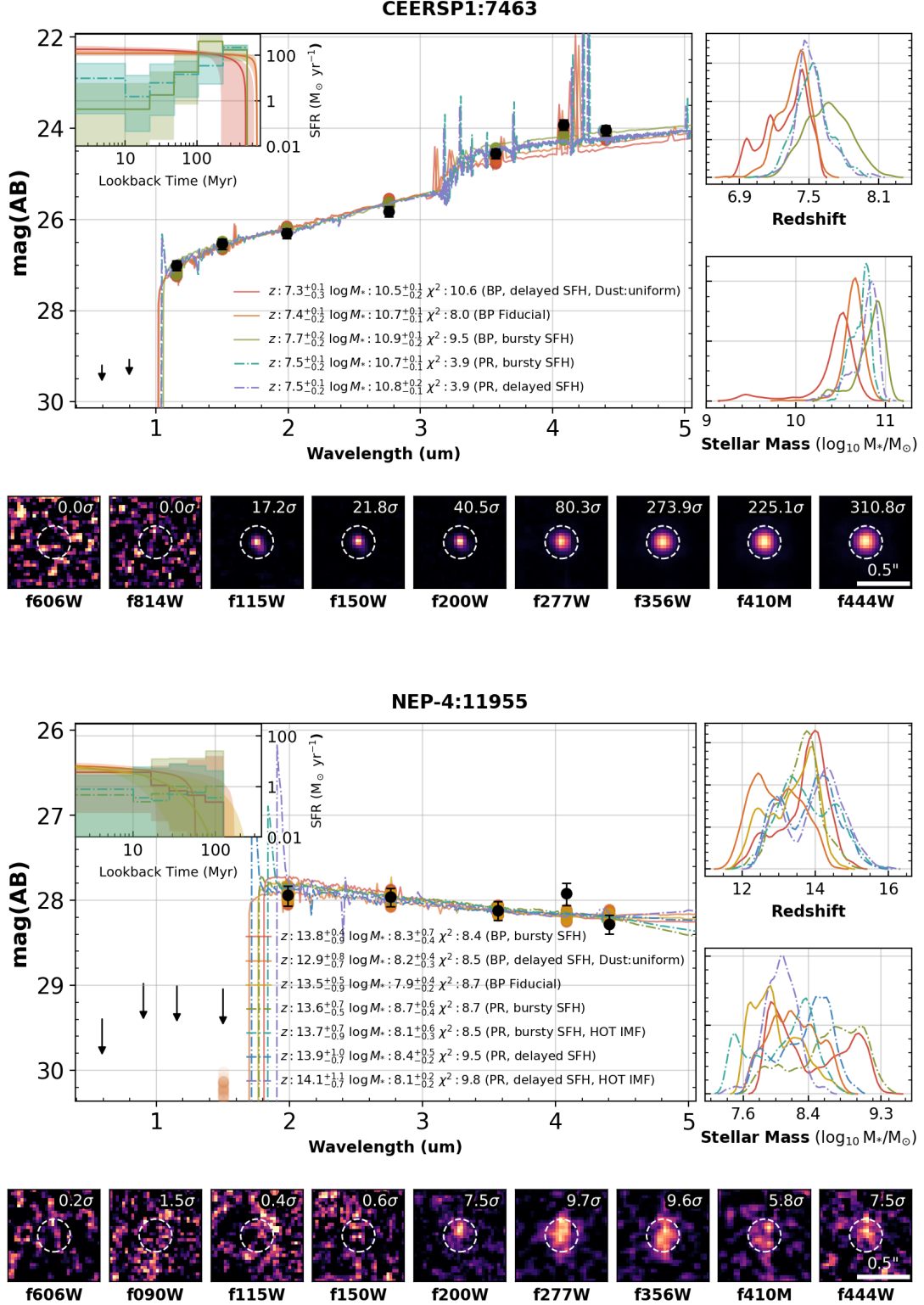


**Figure 3.** Bagpipes (labelled BP) and Prospector SEDs (labelled PR) for two of the galaxies in the EPOCHS v1 sample. The top row shows the galaxy labelled *7463-CEERSP1* with one of the largest fiducial stellar masses in the sample, which is a ‘Little Red Dot’ also identified by [Labbé et al. \(2023\)](#); [Kokorev et al. \(2024\)](#). The bottom row shows *11955-NEP-4*, one of the more massive galaxies found at  $z \geq 10$ , although the range of stellar mass estimates shows how difficult it is to constrain stellar mass at these redshifts. We label the different SED fits by how they differ to our fiducial Bagpipes SED-fitting prescription, with a lognormal SFH, Calzetti et al. (2000) dust model, logarithmic priors on age, dust and metallicity, Bruzual & Charlot (2003) SPS model and a Kroupa (2001) IMF. For each alternative model we also give the redshift, stellar mass and  $\chi^2$  for the fit. On the right of each SED plot we show the posterior redshift and stellar mass PDF distributions and the best-fit SFH history is shown as an inset axes on the upper left.

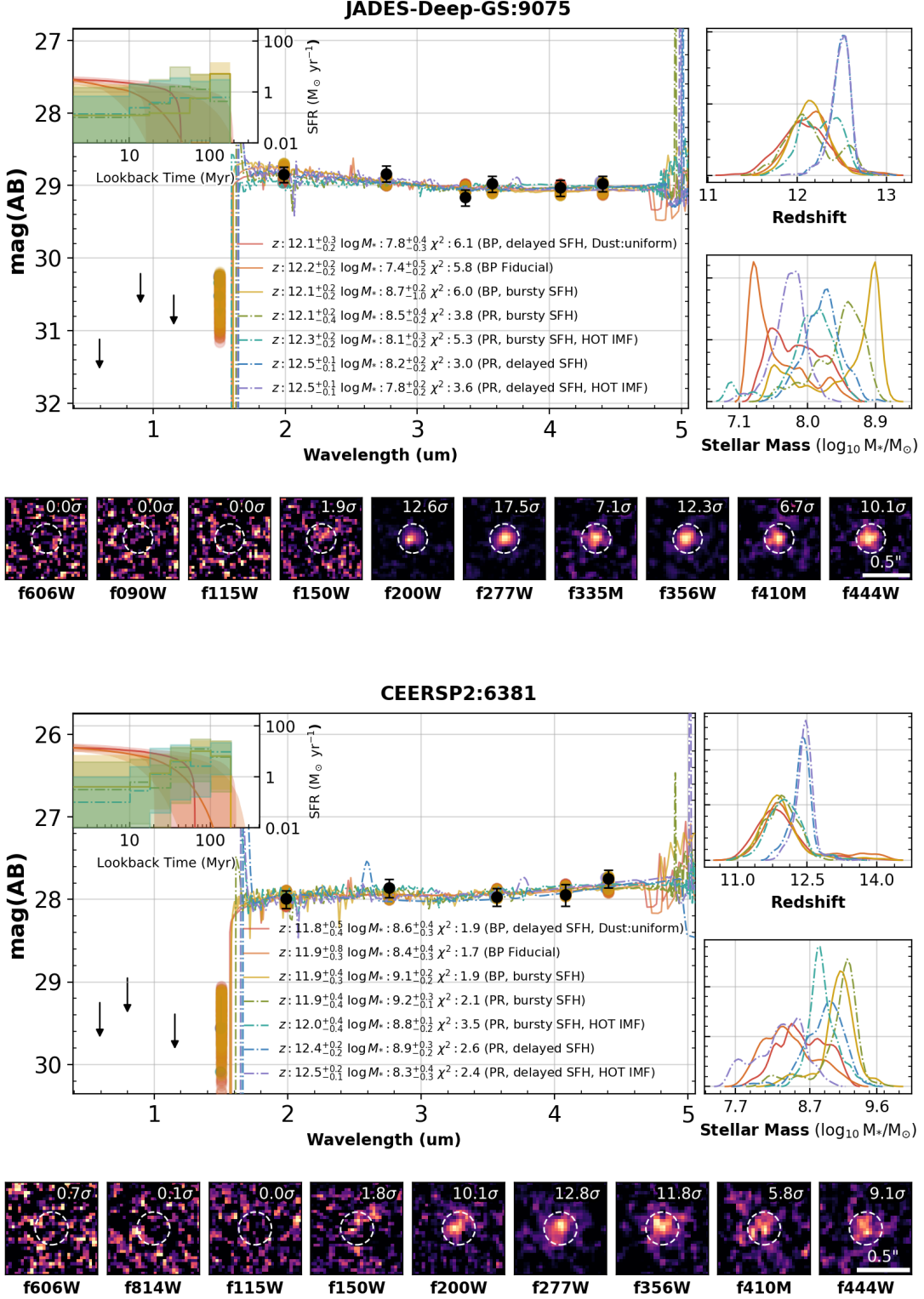


**Figure 4.** The same as [Figure 3](#) except these galaxies are shown to demonstrate the stellar mass discrepancies observed between different *Bagpipes* and *Prospector* SED fits, depending on the chosen star formation history, SED fitting tool, dust law, and IMF. *JADES-Deep-GS:9075* was observed with NIRSspec as part of [Bunker et al. \(2023a\)](#) (NIRSspec ID 00002773), finding  $z_{\text{spec}} = 12.63$ , meaning that *Bagpipes* and *Prospector* slightly underestimate the redshift in most cases.



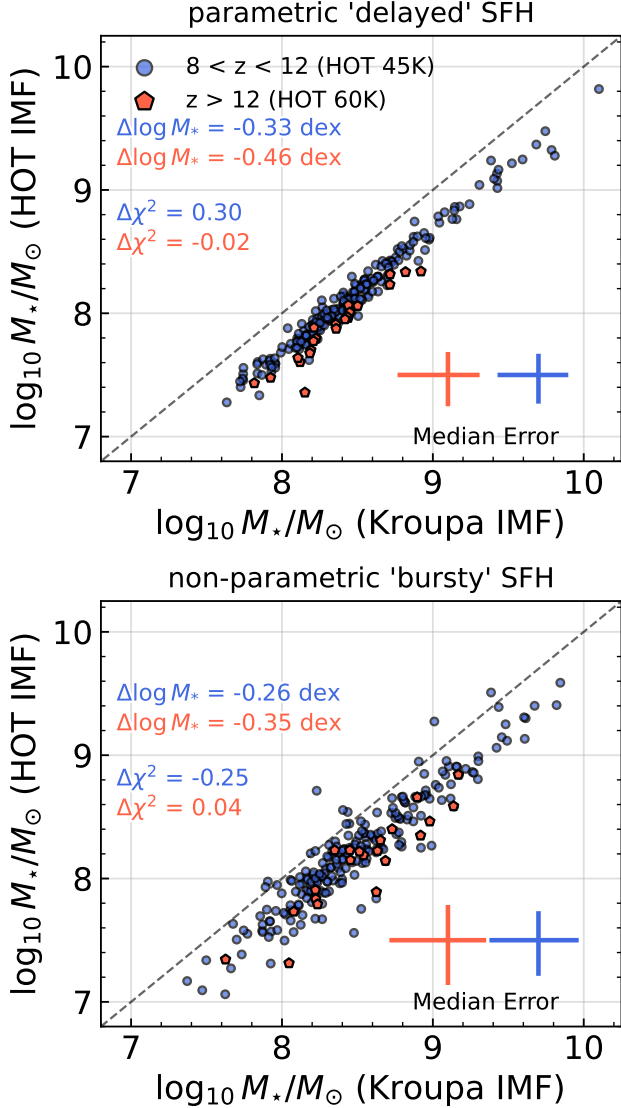


**Figure 5.** (top) Effect of modified top-heavy IMF on galaxy masses using a parametric delayed- $\tau$  SFH, for both the HOT 45K IMF (at  $8 < z < 12$ ) and HOT 60K IMF (at  $z > 12$ ) from Steinhardt et al. (2023). Overlaid on the plot are the median stellar mass and  $\chi^2$  offsets, showing that these IMF models systematically reduce the stellar mass with no impact on the goodness of fit. (bottom) Effect of modified IMF on galaxy masses using a non-parametric “continuity bursty” SFH for both HOT models.

“continuity bursty” SFH model, we find a median stellar mass decrease of 0.26 dex for the  $z \leq 12$  sample (HOT 45K IMF) and a decrease of 0.36 dex for the  $z \geq 12$  sample (HOT 60K IMF). As expected, we see a larger decrease in stellar mass for the HOT 60K model, which is more ‘top-heavy’ than the HOT 45K model.

For the galaxies with the largest fiducial **Bagpipes** stellar masses, which have the most tension with  $\Lambda$ CDM,

we show the possible decrease in stellar mass using a top-heavy HOT IMF in Figure 12.

## 5. GALAXY STELLAR MASS FUNCTIONS

The **Bagpipes** and **Prospector** fitting we perform in § 4.3 explores the consistency of stellar mass estimates on an individual galaxy basis. In order to explore the overall effect of a particular choice of SED fitting tool and model we look at the overall distribution of galaxy masses via the Galaxy Stellar Mass Function (GSMF). We focus primarily on constructing a GSMF from our fiducial **Bagpipes** results, and then demonstrate the effect of changing this to an alternative **Bagpipes** or **Prospector** model.

We make a further cut to our galaxy sample here, removing the fields of El Gordo, SMACS-0723 and Clio. The depths and available filters of these datasets mean that they do not contribute significant volume to our GSMF estimates, but increase the redshift uncertainties (Adams et al. 2023). This reduces the number of galaxies used in the GSMF to 1092, and the total area used to  $175 \text{ } r^2$ .

The GSMF measures the abundance of galaxies of different masses at a given redshift. A stellar mass function  $\Phi(M, z)\Delta M$  is formally defined as the number density of galaxies in a mass bin  $\delta M$  at a given redshift  $z$ . The evolution of the shape and normalisation of the stellar mass function traces the global abundance of baryons across cosmic time, and hence indirectly traces star formation. The integral of the stellar mass function over mass gives the galaxy stellar mass density, which is the cumulative formed stellar mass per unit volume at a given epoch.

We construct a galaxy stellar mass function (GSMF) from different mass estimates in order to investigate possible evolutions of the GSMF at high redshift. To derive the GSMF we use the  $1/V_{\text{max}}$  methodology (Rowan-Robinson & McCrea 1968; Schmidt 1968):

$$\phi(M)d\log(M) = \frac{1}{\delta M} \sum_i \frac{1}{C_i V_{\text{max},i}} \quad (1)$$

with associated uncertainty

$$d\phi(M) = \frac{1}{\delta M} \sqrt{\left( \sum_i \frac{1}{C_i V_{\text{max},i}} \right)^2} \quad (2)$$

where  $\delta M$  is the bin width in stellar mass,  $C_i$  is the completeness of the galaxy in bin  $i$ , and  $V_{\text{max},i}$  is the total observable volume of the galaxy across all the fields. We use Equation 2 to calculate the uncertainty in the bin, except in the case where there are the bin has very low occupancy ( $N \leq 4$ ) where we instead directly calculate the Poisson confidence interval with a

more accurate estimator based on the  $\chi^2$  distribution  $I = [0.5\chi_{2N,a/2}^2, 0.5\chi_{2(N+1),1-a/2}^2]$  (Ulm 1990; Adams et al. 2023), which avoids uncertainties such as  $1 \pm 1$ , which appear infinite on a log-scale.

We iteratively shift the galaxy SED from the fiducial `Bagpipes` SED fitting in small steps of  $\Delta z = 0.01$  before recalculating the bandpass-averaged fluxes in the available NIRCcam and HST filters for a given field. With these fluxes we test if the galaxy would still be selected at every redshift step given our selection criteria detailed in § 3.2. For the selection criteria which are dependent on SNR requirements we base the detection strength on the average depth for each field, as given in Table 1. This allows us to calculate a  $z_{\max}$  and  $z_{\min}$  redshift for each galaxy in each field, capped at the edges of each redshift bin. Accounting for a minimum redshift is essential for accurately measuring the detectable volume given our requirement for the shortest wavelength filter bandpass to fall blueward of the Lyman break. We convert these maximum and minimum redshifts within each bin to a volume by

$$V_{\max,i} = \sum_{\text{fields}} \frac{4\pi}{3} \frac{A_s}{4\pi \text{ sr}} (d_{z_{\max}}^3 - d_{z_{\min}}^3) \quad (3)$$

where  $d_{z_{\max/\min}}$  are the co-moving distances at the maximum/minimum detectable redshifts (capped at bin edges).  $A_s$  are the survey areas, which are given in Table 1. For the purposes of constructing a GSMF we exclude the Clio, El Gordo and SMACS-0723 fields due to their shallow depth or lack of key broadband photometry (e.g. F115W).

The only field containing a significant lensing cluster that we include in the GSMF is the MACS-0416 field. We exclude the cluster itself, and assume there is no significant magnification for our galaxy candidates in the surrounding NIRCcam pointings. None of our candidates show evidence of strong lensing, and we do not expect weak lensing by foreground neighbours to significantly affect our sample.

We account for the posterior stellar mass uncertainties using a Monte Carlo bootstrap methodology to bootstrap our GSMF. We draw stellar mass estimates for each galaxy from the posterior stellar mass probability distribution functions and compute 1000 independent realisations of the galaxy stellar mass function from these posterior PDFs. We compute the 16th, 50th and 84th percentiles of the distribution in order to quantify the uncertainty introduced by our stellar mass estimates, and indirectly by the uncertainties on the photometry. Typically these uncertainties are smaller than the Poisson error, but can be large at the highest mass where individual objects near bin edges can have a large

impact. We require a bin to be occupied in more than 20% of realizations to avoid highly uncertain bins which have very low occupancy.

### 5.1. Detection Completeness

We carry out completeness simulations on JWST data by inserting simulated galaxies with an exponential light profile (Sérsic index of  $n = 1$ ) as galaxies at high- $z$  are typically not concentrated (see Ferreira et al. 2022; Ferreira et al. 2023; Ormerod et al. 2024) and with absolute UV magnitudes ranging from -16 to -24 in the detection image (inverse variance weighted stack of F277W, F356W and F444W). We then run `SExtractor` on them using the same configuration as our normal catalogue creation pipeline in order to measure the fraction recovered as a function of apparent magnitude.

The magnitude range was swept in steps of 0.2, with 1000 sources inserted into the image at a time in order to prevent introducing artificial overdensities. We assume a size - luminosity relation of  $r \propto L^{0.5}$  (Grazian et al. 2012), with reference size set to  $r = 800$  pc at  $M_{\text{UV}} = -21$ , the maximum available size was on the order of 1000 pc. The inclination angle of these sources was assumed to be uniformly random. We sweep a redshift range of 6.5 to 13.5 in steps of 0.5 to account for the changes in angular diameter distance and obtain a 2D dependence of completeness on redshift and absolute magnitude.

The above procedure was carried out on all fields considered in this paper. Given that we perform our detection on a stacked image of the LW bandpasses, our detection completeness is  $> 90\%$  across the redshift ranges and apparent magnitudes of our high- $z$  sample, and the overall completeness is dominated by the impact of our selection criteria.

### 5.2. Selection Completeness and Contamination

To estimate the contamination and completeness of our sample selection as a function of stellar mass we use version 1.2 of the JADES Extragalactic Ultra-deep Artificial Realization (`JAGUAR`) catalogue of synthetic galaxies released by the JADES Collaboration (Williams et al. 2018). We choose this model for our completeness simulations as the catalogues and spectra are readily available, and Wilkins et al. (2023a) have shown that the `JAGUAR` model reproduces the observed color evolution of galaxies at high redshift.

`JAGUAR` is an empirical model based on observational constraints on the mass and luminosity functions at  $z \leq 10$  from HST (Tomczak et al. 2014; Bouwens et al. 2015; Stefanon et al. 2017). Mock spectra and photometry are generated using `BEAGLE` (Chevallard & Charlot

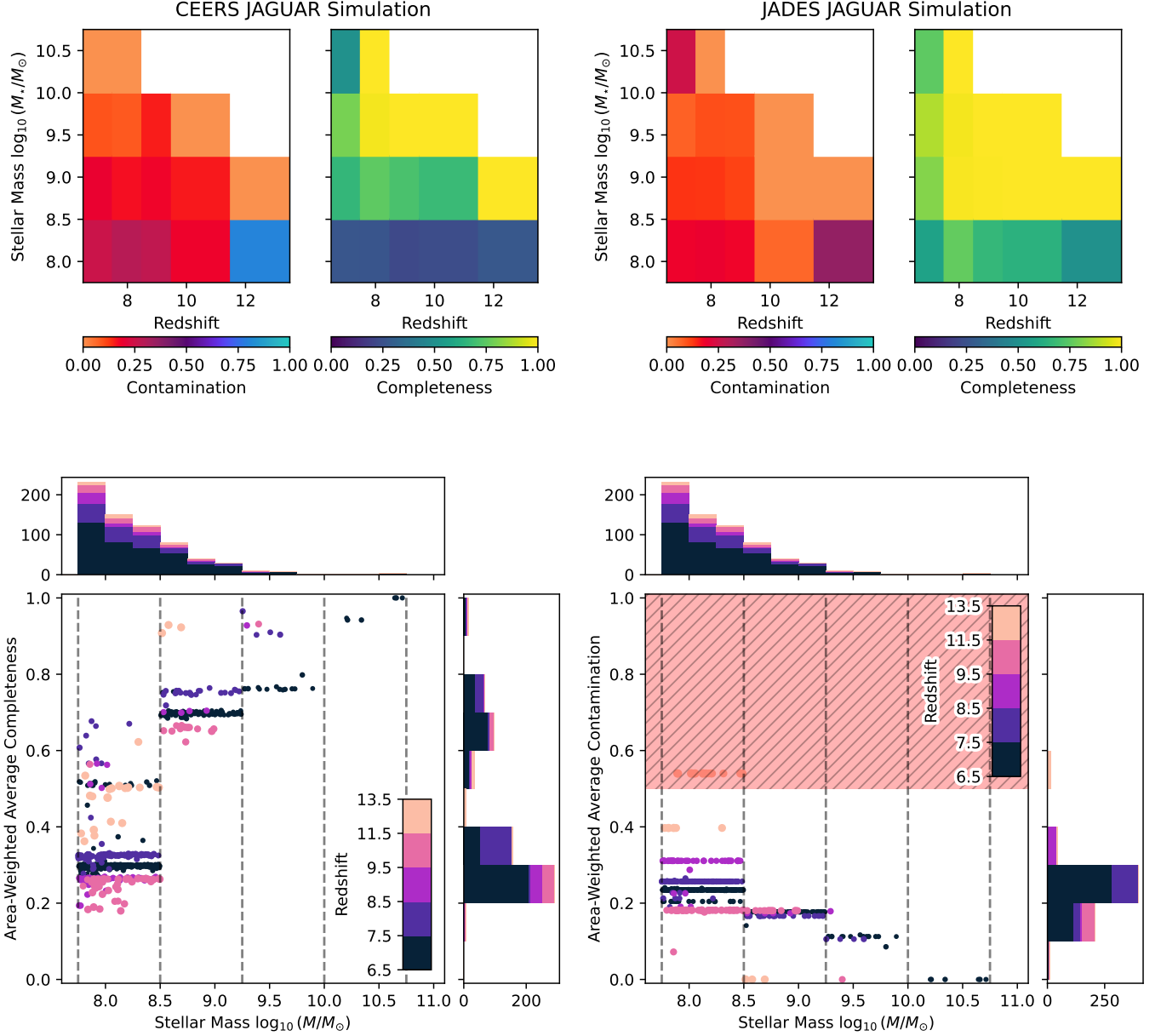


**Figure 6.** **Top)** Selection completeness as a function of redshift and stellar mass for two example fields from our sample, based on our fiducial `Bagpipes` SED fitting and full selection procedure. Completeness and contamination are labelled as fractions, where  $1 = 100\%$ . **Bottom)** Total area-weighted completeness and contamination for each of our galaxies as a function of stellar mass, colored by redshift bin. We see higher completeness and lower contamination at higher mass. The red shaded region in the contamination plot shows our 50% contamination limit.

2016). We combine 5 different realisations of the simulation in order to improve the statistics for rare high- $z$  and high-mass sources. We filter the mock catalogues to the sources which are detectable given the average depths of our observations. This ranges between  $8 \times 10^5$  and  $1.2 \times 10^6$  realistic mock galaxies, which we run through our full galaxy selection procedure.

We generate mock observations from these catalogues by estimating  $1\sigma$  errors in the measurements based on the average depths of our JWST reductions in each field (see Table 1). We then perturb the catalogue photometry in flux space within a Gaussian centered on the catalogue measurement and width equal to the  $1\sigma$  error in that filter. We then run the galaxies through our full selection procedure to measure how well our pipeline re-

covers the true redshifts of the sources. This allows us to compare the robustness of our selection criteria given the differing depths and filters in each set of observations.

We test our ability to reconstruct the stellar masses of the JAGUAR galaxies by fitting their perturbed photometry with our Bayesian SED-fitting using `Bagpipes`. We estimate completeness and contamination for each redshift and mass bin in our mass function by testing the recovery of simulated galaxies into the correct bin. Completeness is defined as the number of galaxies which our pipeline places in the correct redshift and mass bin, divided by the total number of simulated galaxies within that bin. Contamination is defined as the number of galaxies we place in the incorrect bin, divided by the total number of galaxies in the bin. As an example, if there are 100 simulated galaxies in a given redshift/mass bin, and our selection criteria selects 50, of which 10 are actually from a different bin, then the completeness would be 50% (50/100) and the contamination would be 20% (10/50).

We see reasonable agreement between the true stellar mass and our inferred stellar mass. Initially 50% of galaxies fall within the correct stellar mass bin used in construction of the galaxy stellar mass function. In order to account for the different choice of IMF and SFH parametrization between the JAGUAR SEDs and our `Bagpipes` fitting, we derive a corrective scaling factor by which we scale the JAGUAR masses in order to increase the agreement between the mass estimates to 65%. As we bootstrap the GSMF using the stellar mass PDFs, we find that 80% of galaxies will contribute to the correct mass bin. The average offset between our recovered stellar mass and the simulated mass is 0.02 dex, with a standard deviation of 0.28 dex. Only 2% of the time is the deviation between the scattered and recovered masses greater than 0.75 dex, which is the bin width used in the stellar mass functions.

Figure 6 shows the completeness and contamination for the CEERS and JADES fields, which make up a significant fraction of our total volume.

To derive a single estimate of completeness and contamination for each galaxy, we calculate the area-averaged completeness and contamination for each galaxy in our sample, based on the fields in which the galaxy is found to be observable in when we calculate  $V_{\max}$ . The bottom row of Figure 6 shows the total completeness, including both detection and selection, for each galaxy as a function of stellar mass. Completeness is strongly dependent on the stellar mass of the galaxy, and at masses below  $\approx 10^8 M_{\odot}$  we are  $\leq 50\%$

complete in the majority of our area, and dependent on the derived completeness corrections.

In order to reduce the possible effects of contamination on our derived mass functions, we exclude objects where the estimated contamination fraction is  $\geq 50\%$ . In the cases where no simulated galaxies fall within a given bin, which occurs only for the highest mass bins where we expect high completeness, we do not apply any correction factor. We also assume 100% completeness when the total number of simulated galaxies in a mass-redshift bin is  $\leq 5$  due to the high uncertainty in deriving correction factors with low statistics.

Multiple classes of interlopers with photometry similar to high-redshift galaxies can contaminate estimates of the GSMF. In this section we detail our methodology to remove common types of interlopers, including low- $z$  galaxies, brown dwarfs, and AGN.

### 5.2.1. Low- $z$ Galaxies

The misclassification of low- $z$  galaxies as high- $z$  through catastrophic errors in photo- $z$  are commonly caused by misidentification of different spectral features, e.g. confusion of the Lyman and Balmer breaks, or strong rest-frame optical emission lines contributing to multiple wideband photometric observations, giving the appearance of continuum emission (e.g. the  $z = 16$  candidate in Donnan et al. (2022); Arrabal Haro et al. (2023), which we do not select with as a robust high- $z$  galaxy with our EAZY-py SED fitting and selection criteria).

Firstly, we compare our EAZY-py photo- $z$  estimates with spectroscopic redshifts (spec- $z$ 's) in Adams et al. (2023). In summary, we typically find  $> 90\%$  accuracy (within 15%). With our EAZY-py photo- $z$ 's, which we use as an informative prior for `Bagpipes` and `Prospector`, we do not observe the systematic photo- $z$  overestimation observed in other studies (Fujimoto et al. 2023; Arrabal Haro et al. 2023).

We are able to fully test the rate of catastrophic photo- $z$  failure using our JAGUAR completeness and contamination simulations. The rate of contamination increases as we approach our  $5\sigma$  detection limits in the rest-frame UV, and the vast majority of the contaminants have  $< 8\sigma$  detections in the rest-frame UV. If we parametrize in terms of stellar mass, the highest rates of contamination are seen at lower stellar mass where individual galaxies have less impact on the GSMF. Candidates with SNR close to our selection limit are also those most commonly rejected in our manual inspection of all candidates, providing another layer of protection against possible interlopers.

We restrict the redshift range and fields used when constructing the GSMF to exclude uncertain high- $z$  candidates. We do not include observations of El Gordo, Clio or SMACS-0723 when constructing the GSMF because they are shallow and show high rates of contamination in our JAGUAR simulations. Clio and SMACS-0723 also lack observations in F115W, which Trussler et al. (2023) shows lead to inaccurate photometric redshifts at  $8 < z < 10$ . Despite our sample containing galaxies at  $z \geq 14$ , we do not attempt to measure the GSMF above  $z \geq 13.5$  because we lack the appropriate medium band observations (or spectroscopy) to remove interlopers such as the  $z = 16$  candidate in Donnan et al. (2022). Below redshift 13.5 we have seen high accuracy in photo- $z$  estimates when compared to NIRSpec spectroscopy (e.g. Curtis-Lake et al. 2023; Bunker et al. 2023a; Arrabal Haro et al. 2023; Wang et al. 2023a).

### 5.2.2. Brown Dwarfs

Y and T-type brown dwarfs within the Milky Way can masquerade as high-redshift galaxies due to the appearance of a Lyman-break like dropout caused by strong molecular absorption in the optical, coupled with bright near-infrared emission. When mistaken for high- $z$  galaxies brown dwarfs can have a large impact on the galaxy stellar mass function due to their high inferred stellar masses.

We fit the photometry of all of our galaxy candidates with the synthetic Sonora Bobcat brown dwarf templates (Marley et al. 2021) using a simple  $\chi^2$  minimization to scale the flux of the templates to each candidate. We fit all the provided templates to each candidate, selecting the best-fitting template for each galaxy. We remove candidates from our sample which are both better fit by a brown dwarf template than a galaxy template, and show a PSF-like morphology (50% encircled flux radius in F444W < F444W PSF FWHM). This removes 59 candidates in total (4% of the total sample). Figure 7 shows an example of several brown dwarf candidates which would otherwise have been selected as high- $z$  galaxy candidates.

None of the brown dwarf candidates selected in Hainline et al. (2023) are contained within our robust galaxy sample in the Goods-South or CEERS fields. As a check of our selection criteria we confirm that all of Hainline et al. (2023)'s candidates located within the footprint of our datasets (GOODS-South, CEERS) are selected as brown dwarfs by our brown dwarf selection criteria.

### 5.2.3. Active Galactic Nuclei

Given the apparent prevalence of high- $z$  AGN detected by multi-wavelength and spectroscopic studies it is likely there is a population of galaxies containing AGN

within this sample. Our modelling does not fit AGN components to the photometry, so if galaxies contain a significant AGN component it is likely we will overestimate the stellar mass. In particular, obscured AGN with red colors (e.g. Kocevski et al. 2023; Labbé et al. 2023) can mimic strong Balmer breaks, leading to inference of an aged stellar population and high stellar mass. Known as LRDs, a number of studies have found numerous candidates up to  $z \leq 9$  (see e.g. Greene et al. 2023; Furtak et al. 2023; Furtak et al. 2023; Barro et al. 2023; Matthee et al. 2023; Labbe et al. 2023; Kokorev et al. 2024). Pérez-González et al. (2024) uses MIRI observations of LRDs to suggest that the characteristic photometry is driven mostly by stellar emission, and that LRDs are mostly compact and highly obscured starburst galaxies with young stellar ages. Other studies have struggled to distinguish between AGN and stellar models (Barro et al. 2023) or favour an AGN model (Noboriguchi et al. 2023). Further spectroscopic or MIRI observations can break the degeneracy between AGN and old stellar populations. We attempt to perform additional SED fitting using *Prospector* by including an AGN component, which models AGN emission lines for the most massive galaxies in our sample ( $M_\star \geq 10^{9.5} M_\star$ ). In almost all cases the AGN fraction is less than 10%, and we see no reduction in stellar mass due to the inclusion of AGN component. The addition of an AGN model does not statistically improve the fit for these galaxies, although we can not strongly exclude the presence of AGN in some of our candidates as the AGN model within *Prospector* models only obscured AGN (Leja et al. 2018). Further fitting with a wider range of AGN models, which is outside the scope of this paper, is required to constrain the potential contribution of AGN emission to the observed photometry. Given the uncertainty around the true nature of these sources, we choose not to remove them from our sample. We discuss the impact of LRDs on the GSMF in Appendix A.

We do however remove two galaxies from our sample which are spectroscopically confirmed as AGN, or with significant AGN components within the photometry. This includes the AGN within the CEERS field presented in Larson et al. (2023).

### 5.3. Cosmic Variance

Cosmic variance is the field-to-field variance of the distribution of galaxies at a given redshift due to galaxy clustering. Empirical measurements of cosmic variance do not exist at  $z \geq 7$ . Estimates of cosmic variance from simulations (e.g. *Bluetides*, Bhowmick et al. 2020) are available, but the accuracy of these estimates is difficult to measure given the limited cosmological volume

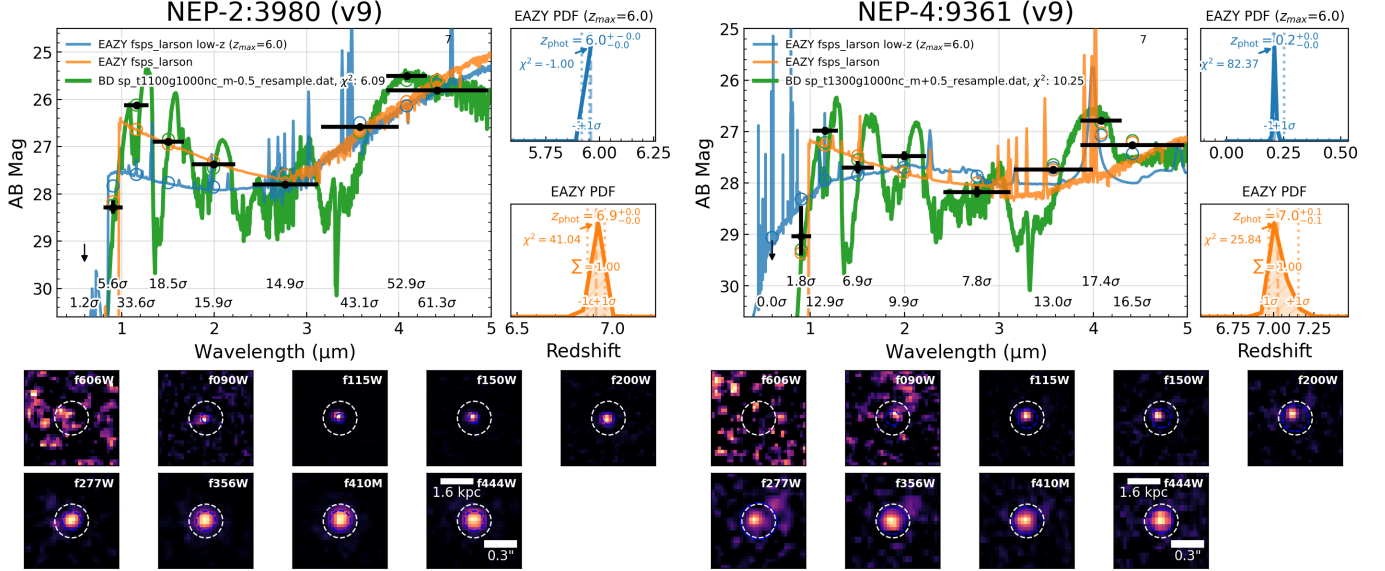


**Figure 7.** Two example SEDs from our sample of 59 brown dwarf candidates (in green) selected with the Sonora Bobcat models, shown along with their best-fitting high- $z$  galaxy SEDs (in orange). The low redshift galaxy solution (with an upper redshift limit of  $z \leq 6$ ), which is used in our robust galaxy selection criteria, is shown in blue. The redshift posteriors from **EAZY-py** are shown for both the high and low redshift galaxy models, and are overlaid with the statistics used within our selection criteria, indicating the  $\chi^2$  and integral of the primary PDF peak. The cutouts of both brown dwarf candidates are shown below the best-fitting SEDs, demonstrating their compact PSF-like morphology. The cutouts are  $0''.9$  across, as shown with the scalebar and the white circle shows the extraction aperture used for SED-fitting ( $0''.16$  radius) The scalebar showing physical size in kpc is calculated at the best-fitting galaxy photo- $z$  and is not applicable to the brown dwarf solution. The coordinates for these brown dwarf candidates are  $17\text{h}23\text{m}12.36\text{s} +65\text{d}49\text{m}38.8\text{s}$  and  $17\text{h}21\text{m}53.00\text{s} +65\text{d}49\text{m}20.82\text{s}$  respectively.

and dependence on the assumed cosmology and galaxy formation physics. [Bhowmick et al. \(2020\)](#) argues that cosmic variance will be a dominant source of uncertainty at these redshifts, as galaxies are predicted to be highly clustered ([Bhowmick et al. 2018](#)).

We caution that the following methodology provides only an approximation of the true cosmic variance as the underlying quantities, such as the galaxy bias, are not well-quantified at  $z \geq 7$  and are generally extrapolated from wider area clustering results at lower redshift or taken from N-body simulations ([Moster et al. 2010](#)). We estimate the uncertainty on the GSMF due to cosmic variance following the prescription of [Driver & Robotham \(2010\)](#), combining the cosmic variance from different surveys using the volume weighted sum of squares from [Moster et al. \(2011\)](#). We treat nearby pointings as one observation and sum their areas (e.g. the multiple pointings of CEERS or the NEP, which are not widely separated enough on the sky to be considered independent). We add the uncertainty in quadrature to [Equation 2](#).

We compute a cosmic variance estimate for each galaxy individually based on which of our fields they are found to be detectable in. Given that this work com-

bins multiple widely separated fields for the majority of our sample cosmic variance is small compared to studies incorporating only a single field. We see little difference in cosmic variance across our redshift bins. In the best case, where a galaxy is detectable across every field, the average cosmic variance across all redshift bins is found to be 18%. The highest cosmic variance estimates are for faint galaxies which, given our selection criteria, are only detectable in the JADES GOODS-South field, where we find a cosmic variance of 42%.

#### 5.4. Fitting the GSMF

The overall scientific consensus is that the stellar mass function at high- $z$  is well-described by the *Schechter* function ([Schechter 1976](#)), given in logarithmic form in [Equation 4](#).

$$\Phi(d \log M) = \ln(10) \Phi^* e^{-10^{\log M - \log M^*}} \times (10^{\log M - \log M^*})^{\alpha+1} d \log M \quad (4)$$

The Schechter function, which consists of a power-law with an exponential fall-off, is parameterised by 3 parameters:  $\alpha$ ,  $M^*$ , and  $\Phi^*$ .  $\alpha$  controls the slope of the low-mass end of the SMF, while  $M^*$  gives the turnover

point at which the function turns from a power-law to an exponential fall-off.  $\Phi^*$  controls the overall scaling of the SMF, and is the only parameter that has been confidently shown to evolve with cosmic time (Popesso et al. 2023). Stellar mass functions are sometimes split into star-forming and quiescent, with a division in specific star formation rate (sSFR). SMFs for quiescent galaxies are often parameterised by double Schechter functions (Weigel et al. 2016).

Before JWST the mass function was constrained up to  $z \approx 9$  using HST WFC3/IR, Spitzer/IRAC and ground-based data (*Visible and Infrared Survey Telescope for Astronomy* (VISTA), *United Kingdom Infrared Telescope* (UKIRT)) observations of the HUDF, CANDLES, *Cluster Lensing and Supernova survey with Hubble* (CLASH) and *Hubble Frontier Fields* (HFF) surveys (Stark et al. 2013; Bradač et al. 2014; Duncan et al. 2014; Bouwens et al. 2016; Song et al. 2016; Stefanon et al. 2017; Bhatawdekar et al. 2019; Kikuchihara et al. 2020). These studies generally agree that the mass function steepens out to  $z \approx 10$ , with the low-mass slope,  $\alpha$ ,  $\rightarrow -2$ . Duncan et al. (2014); Bhatawdekar et al. (2019); Stefanon et al. (2021) find that the stellar mass to halo mass ratio in galaxies ( $M_\star$ - $M_h$ ) shows no evolution over  $6 \leq z \leq 10$  despite a 3 dex increase in overall stellar mass, suggesting that stellar and halo mass grew together during reionization. Pre-JWST, the accuracy of stellar mass functions at these redshifts is limited by the uncertainty in stellar mass estimates from Spitzer data, where the broadband photometry can be affected by strong nebular emission causing scatter in stellar mass estimates, which is compounded by the limited number of spectroscopically confirmed galaxies at these redshifts (Roberts-Borsani et al. 2016; Strait et al. 2020). Previously, measurements of the mass function above  $z \geq 6$  have relied on UV-selected samples of galaxies, with mass indirectly inferred through a calibrated  $L_{UV}$ - $M_\star$  relationship (Song et al. 2016; Harikane et al. 2016) rather than direct measurements of the rest-frame optical wavelengths. Photometric mass-selected samples above  $z \geq 2$  all have significant mass uncertainties at higher redshift (Retzlaff et al. 2010; Laigle et al. 2016; Weaver et al. 2022). Many studies combine ground and space-based observations in order to probe the entire mass function, although combining these datasets robustly is difficult due to systematics between different surveys, including differing selection functions, SED fitting techniques, detection bands, and survey depths.

We derive a mass function for 5 redshift bins:  $6.5 \leq z < 7.5$ ,  $7.5 \leq z < 8.5$ ,  $8.5 \leq z < 9.5$ ,  $9.5 \leq z < 11.5$  and  $11.5 \leq z < 13.5$ , which covers a time period of  $\sim 500$  Myr. We cover a mass range from  $7.75 \leq$

$\log_{10} M_\star/M_\odot \leq 11.5$  in steps of  $0.75 \log_{10} M_\star/M_\odot$ . Our lower mass limit is driven by our completeness simulations, and the bin width is chosen to ensure adequate statistics in the majority of bins. Given the quantisation of our completeness correction to each stellar mass/redshift bin, we ensure our mass bins are wide enough to ensure our SED fitting places galaxies within the correct mass bin, so that the completeness corrections are calculated correctly. by ensuring that we can recover the masses of the simulated galaxies to within the correct stellar mass bin. We fit the GSMF using Bayesian methods; specifically Markov-Chain Monte Carlo via the `emcee` package (Foreman-Mackey et al. 2013).

For our highest redshift bin ( $11.5 \leq z < 13.5$ ), we do not attempt to fit the mass function for a number of reasons; firstly given the low number of available data point points a meaningful fit is not possible without fixing multiple parameters, and secondly due to the increasing uncertainties in stellar mass estimates and reliability of candidates at these redshifts. Furthermore the stellar mass estimates are less reliable when there is less rest-frame optical photometry available during SED fitting. Our JAGUAR simulations also suggest that this bin has high contamination at lower mass, with many galaxies below  $10^{8.5} M_\odot$  having  $\geq 50\%$  average contamination across the fields they are detectable in.

We use wide uniform priors on  $\Phi^*$ ,  $M^*$  and  $\alpha$ , with  $-8 \leq \log \Phi^* \leq -2$ ,  $8.0 \leq \log M^* \leq 12.5$  and  $-3.5 \leq \alpha \leq -1.0$  in our MCMC fitting procedure and run until it has converged before taking 50,000 independent draws from the posterior. We calculate the median posterior, the  $\pm 1\sigma$  uncertainty from the 16th/84th percentiles as well as the maximum likelihood draw.

### 5.5. Mass Functions at $6.5 < z < 13.5$

Table 3 gives our tabulated GSMF for each redshift bin, as well as the associated 68% ( $1\sigma$ ) uncertainties. We also list the median number of galaxies which contribute to each mass bin, as well as the average completeness and contamination estimates. As discussed in § 5, bootstrapping the GSMF means that the estimates for completeness, contamination, and occupation shown are only averages as they will vary in each realization of the GSMF.

Figure 8 shows our derived GSMF (red circles) and associated Schechter fit for each redshift bin, with a comparison to relevant literature results. For the lower redshift bins, which have the most comparisons in the literature, we split our comparison into observational and simulated results to aid readability. The shaded regions shown represent the 68% ( $1\sigma$ ) uncertainty combining

the cosmic variance, Poisson error, and bootstrapping via the mass PDFs. Mass bins with  $\leq 50\%$  completeness are plotted without a black border. We also show GSMF estimates without completeness corrections applied with red diamonds. We convert the GSMF estimates from the literature to a Kroupa (2001) where necessary, using the assumptions of Madau & Dickinson (2014).

The uncertainty regions are likely underestimated; (Wang et al. 2023b) argue the statistical uncertainties encoded in the posterior distributions used for bootstrapping the GSMF do not represent the true uncertainty on the stellar mass estimates due to underlying modelling assumptions, such as the SPS model, IMF, nebular modelling and assumed SFH. We explore the impact of these assumptions on the GSMF further in § 6.5.6, showing that alternative GSMF estimates fall outside the uncertainty region.

Table 4 gives the maximum likelihood and median posterior estimates for our Schechter function parameters for each redshift bin. Uncertainties correspond to the 16\84th percentile of each parameter distribution. Table 5.5 shows the contours which correspond to the 68% ( $1\sigma$ ) and 95% ( $2\sigma$ ) confidence levels.

Table 5.5 shows the covariance of the Schechter parameters for each GSMF fit. A range of parameters are able to fit our GSMF estimates, demonstrating the highly covariant nature of the Schechter parameters. We note that the confidence intervals for the turnover mass,  $M^*$ , and the normalization,  $\phi^*$ , appear somewhat unconstrained at the high and low ends respectively. The lack of constraint on  $M^*$  is a consequence of the wide stellar mass bins used and consequential low number of overall mass bins. Wherever we find  $M^* > 11.5$ , the GSMF is fit by a pure power-law only, and there is no reason to continually extend the prior outside the range where we have available data to constrain  $M^*$ .

Figure 10 shows the redshift evolution of these Schechter parameters, with a comparison to those derived in the literature. It is difficult to measure any significant redshift evolution, given the large uncertainty and covariance of the results. We observe some evidence of evolution of the low-mass slope  $\alpha$ , which steepens toward higher redshift in all but the highest redshift bin.

In Figure 10 and Table 5.5 we see that often our highest-likelihood Schechter function does not coincide with the median posterior, despite the model being fully-converged and a large number of posterior sample drawn.

## 5.6. Stellar Mass Density

The stellar mass density measures the cumulative build-up of stellar mass across cosmic time. This is given by the integration of the stellar mass function  $\phi(M, z)$  at a given epoch (redshift) between two limiting masses, as shown in Equation 5. Care must be taken when comparing different estimates of the stellar mass density (SMD), as the choice of IMF means mass estimates must be converted; for example, to convert from a Chabrier et al. (2000) IMF to a Salpeter (1955) IMF masses must be multiplied by a factor of 1.64 (Madau & Dickinson 2014).

$$\rho_*(M, z) = \int_{M_l}^{M_u} M \phi(M, z) dM \quad (5)$$

The upper and lower integration limits  $M_u$  and  $M_l$  are normally taken to be  $10^{13} M_\odot$  and  $10^8 M_\odot$  (see e.g. Davidzon et al. 2017; Bhatawdekar et al. 2019; Weaver et al. 2022).

We perform the integration given in Equation 5, where  $\phi(M, z)$  is the best-fitting Schechter function fit for each redshift bin. We make use of the `quad` function from SciPy (Virtanen et al. 2020), integrating between  $10^8 M_\odot$  and  $10^{13} M_\odot$ . We compare the integration of both the maximum likelihood fit as well as the median posterior fit. For comparison we also integrate the best-fitting Schechter functions from the literature in each redshift bin, converting to a Kroupa (2001) IMF if necessary.

Figure 11 shows our estimate for the stellar mass density at  $6.5 \leq z \leq 11.5$  from integration of the GSMF derived from our fiducial `Bagpipes` mass functions. We show comparisons to observational SMD results at  $z \geq 5.5$ . Estimates of the stellar mass density at  $z \leq 5$  can be found in the literature Madau & Dickinson (2014); Driver et al. (2018). We also tabulate our SMD values in Table 5.

We integrate all independent posterior draws in order to propagate our mass function uncertainties into the stellar mass density. We show comparisons to predictions and measurements of the cosmic star formation rate density (SFRD,  $\psi$ ) using Equation 6 from Madau & Dickinson (2014) in order to estimate the inferred stellar mass density:

$$\rho_*(z) = (1 - R) \int_z^\infty \psi \frac{dz}{H(z')(1+z')} \quad (6)$$

The return fraction  $R$  is estimated as 0.423 under the assumptions of Madau & Dickinson (2014) for a Kroupa (2001) IMF (a well-mixed closed-box model with constant IMF and metal yield and instantaneous recycling of metals). We integrate the predictions of Madau & Dickinson (2014), Oesch et al. (2018) and the UV luminosity density derived results of Adams et al. (2023), as well as other JWST-era measurements. For Adams



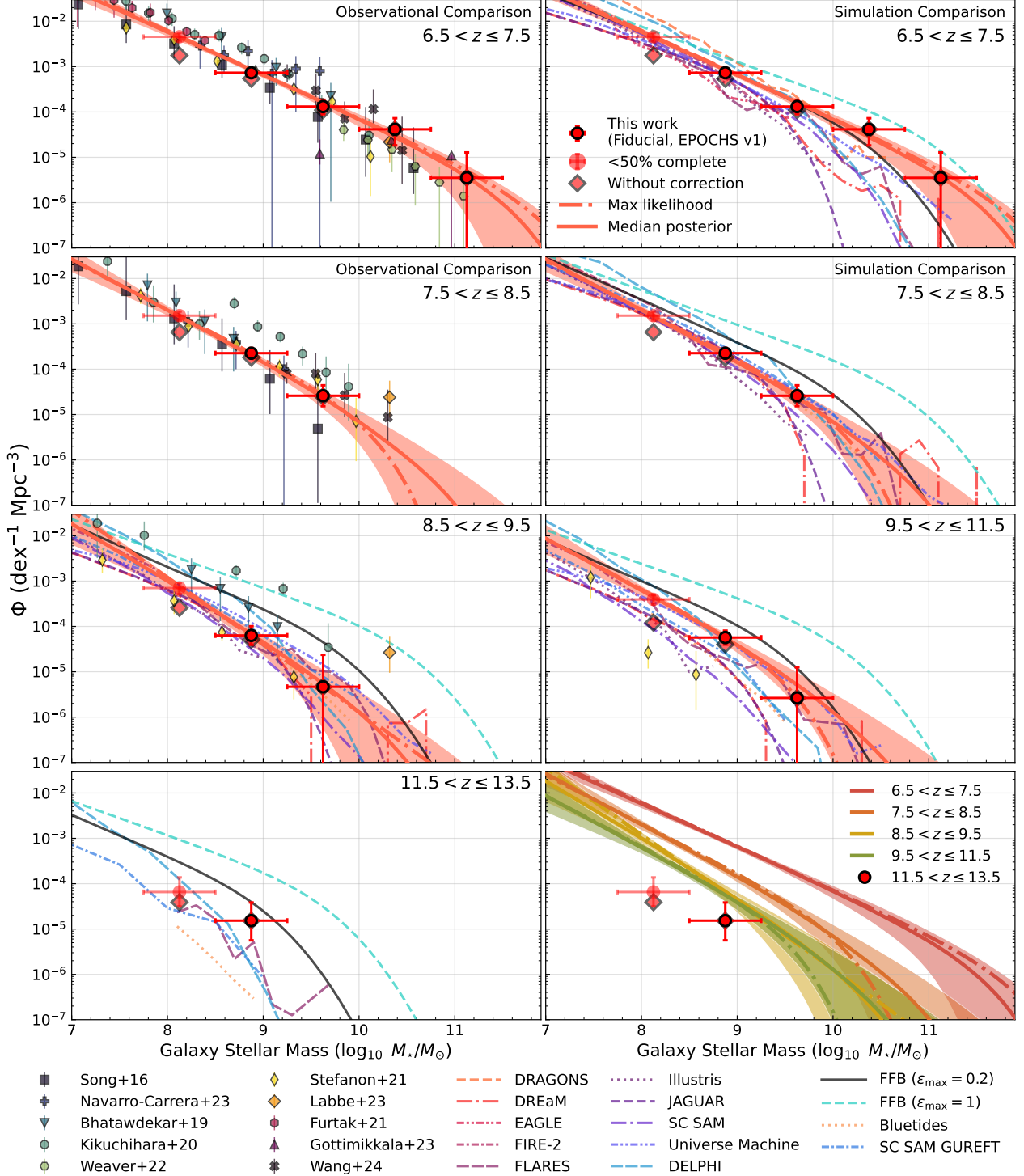


**Figure 8.** Galaxy Stellar Mass Functions (red markers) and the best fitting Schechter functions (red solid and dash-dot lines indicating the median and maximum likelihood draws from the fit posterior, and the 16<sup>th</sup> and 84<sup>th</sup> percentiles are shown by the red shaded region) for the EPOCHS v1 sample derived from the fiducial `Bagpipes` masses and photometric redshifts. We do not fit the  $z \sim 12.5$  bin due to low statistics, uncertain stellar masses and the potential for high contamination. The bottom-right plot shows a comparison of the best-fitting Schechter functions for all redshift bins. Comparison to the following simulations are shown; *BLUETIDES* ( $z \leq 13$ , Feng et al. (2016); Wilkins et al. (2017)), *DRAGONS* ( $z \leq 7$ , Mutch et al. (2016)), *DREaM* ( $z \leq 10$ , Drakos et al. (2022)), *EAGLE* ( $z \leq 7$ , Furlong et al. (2015); Schaye et al. (2015)), *FIRE-2* ( $z \leq 10$ , Ma et al. (2018)), *FLARES* ( $z \leq 15$ , Lovell et al. (2021); Wilkins et al. (2023b)), *Illustris* ( $z \leq 10$ , Genel et al. (2014)), *Jaguar* ( $z \leq 10$ , Williams et al. (2018)), *DELPHI* ( $z \leq 20$ , Mauerhofer & Dayal (2023)), *Santa Cruz SAM (GUREFT)* ( $z \leq 17$ , Yung et al. (2019, 2023)), *Universe Machine* ( $z \leq 10$ , Behroozi et al. (2019)) and the Feedback Free Burst model of Li et al. (2023) (FFB,  $\epsilon_{\max} = 0.2$ ,  $5 \leq z \leq 20$ ). We also show the SMF upper limit from Li et al. (2023), assuming a maximum star formation efficiency ( $\epsilon_{\max}$ ) of unity. Comparisons to observational results from Song et al. (2016), Bhatawdekar et al. (2019) (disc-like galaxies), Kikuchi et al. (2020), Stefanon et al. (2021), Furtak et al. (2021), Weaver et al. (2022), Navarro-Carrera et al. (2023), Gottumukkala et al. (2023) and Wang et al. (2024). The observational results have been converted to a Kroupa (2001) IMF where necessary. In a minority of cases there is  $\Delta z \leq 0.5$  between the redshift of our SMF and literature comparisons.

**Table 3.** Tabulated GSMF from our fiducial **Bagpipes** SED-fitting. We give the average number of galaxies in each bin as well as the estimated average completeness and contamination estimates based on our **JAGUAR** simulations, along with the median redshift (in brackets) and stellar mass for all the objects in a given bin. See § 5.2 for the definition of completeness and contamination used in this work. This table is available for download at <https://github.com/tHarvey303/EpochsIV>.

Redshift Bin	$\log_{10}(\frac{M_*}{M_\odot})$	Med( $\log_{10} M_*$ )	$\Phi$ ( $10^{-4} \text{dex}^{-1} \text{Mpc}^{-3}$ )	Comp (%)	Cont (%)	$N_{gal}$
6.5 < z ≤ 7.5 (6.94)	$8.125 \pm 0.375$	8.07	$49.65^{+10.69}_{-10.29}$	31	23	273
	$8.875 \pm 0.375$	8.75	$7.37^{+1.79}_{-1.57}$	70	18	103
	$9.625 \pm 0.375$	9.47	$1.32^{+0.53}_{-0.42}$	79	10	18
	$10.375 \pm 0.375$	10.40	$0.64^{+0.46}_{-0.35}$	60	0	5
	$11.125 \pm 0.375$	10.81	$0.04^{+0.09}_{-0.04}$	100	0	1
7.5 < z ≤ 8.5 (8.02)	$8.125 \pm 0.375$	8.09	$16.06^{+3.68}_{-3.48}$	35	25	109
	$8.875 \pm 0.375$	8.73	$1.64^{+0.60}_{-0.45}$	75	17	30
	$9.625 \pm 0.375$	9.45	$0.17^{+0.17}_{-0.08}$	91	11	4
8.5 < z ≤ 9.5 (8.86)	$8.125 \pm 0.375$	8.02	$8.16^{+2.30}_{-2.13}$	28	30	40
	$8.875 \pm 0.375$	8.71	$0.50^{+0.35}_{-0.20}$	70	17	8
	$9.625 \pm 0.375$	9.48	$0.05^{+0.10}_{-0.05}$	93	18	1
9.5 < z ≤ 11.5 (10.40)	$8.125 \pm 0.375$	8.10	$4.53^{+1.12}_{-1.00}$	26	18	42
	$8.875 \pm 0.375$	8.73	$0.64^{+0.25}_{-0.19}$	65	18	16
	$9.625 \pm 0.375$	9.42	$0.03^{+0.10}_{-0.02}$	93	0	1
11.5 < z ≤ 13.5 (11.94)	$8.125 \pm 0.375$	8.09	$2.13^{+0.99}_{-0.90}$	34	40	5
	$8.875 \pm 0.375$	8.70	$0.22^{+0.22}_{-0.12}$	90	0	5

**Table 4.** Best-fitting Schechter function parameters and uncertainties derived from fitting the derived GSMF. We give both the median posterior parameter values (with  $1\sigma$  uncertainties derived from the 16<sup>th</sup> – 84<sup>th</sup> percentiles), as well as the values corresponding to the maximum likelihood draw from the posterior (given in brackets). This table is available for download at <https://github.com/tHarvey303/EpochsIV>.

Redshift Bin	$\alpha$	$M^*$	$\log_{10} \phi^*$
6.5 < z ≤ 7.5	$-1.94^{+0.10}_{-0.10}(-1.97)$	$11.57^{+0.63}_{-0.85}(11.89)$	$-5.98^{+0.87}_{-0.69}(-6.33)$
7.5 < z ≤ 8.5	$-2.12^{+0.18}_{-0.17}(-2.07)$	$10.82^{+1.11}_{-1.07}(10.05)$	$-6.31^{+1.45}_{-1.36}(-5.24)$
8.5 < z ≤ 9.5	$-2.26^{+0.31}_{-0.30}(-2.48)$	$10.47^{+1.15}_{-1.18}(11.81)$	$-6.63^{+1.78}_{-1.50}(-8.93)$
9.5 < z ≤ 11.5	$-2.15^{+0.26}_{-0.22}(-2.10)$	$10.51^{+1.18}_{-1.10}(9.48)$	$-6.58^{+1.61}_{-1.48}(-5.16)$

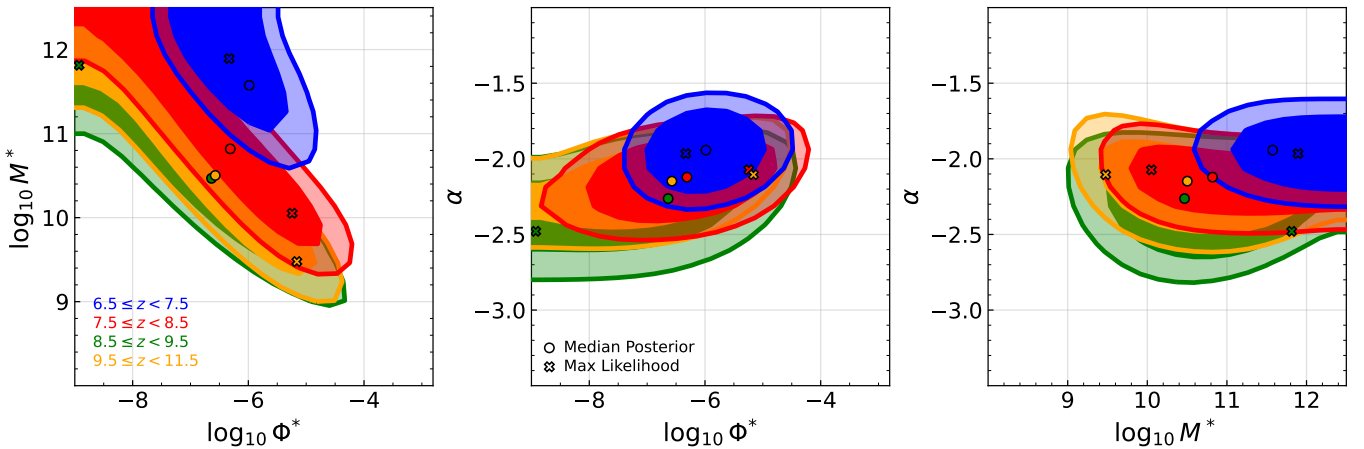


**Figure 9.** Confidence intervals for our best-fitting Schechter parameters for all fitted redshift bins. Overlaid are the locations of the median posterior value (filled circles) and maximum likelihood draw (filled crosses). Filled (shaded) regions show the 68% (95%) confidence levels.

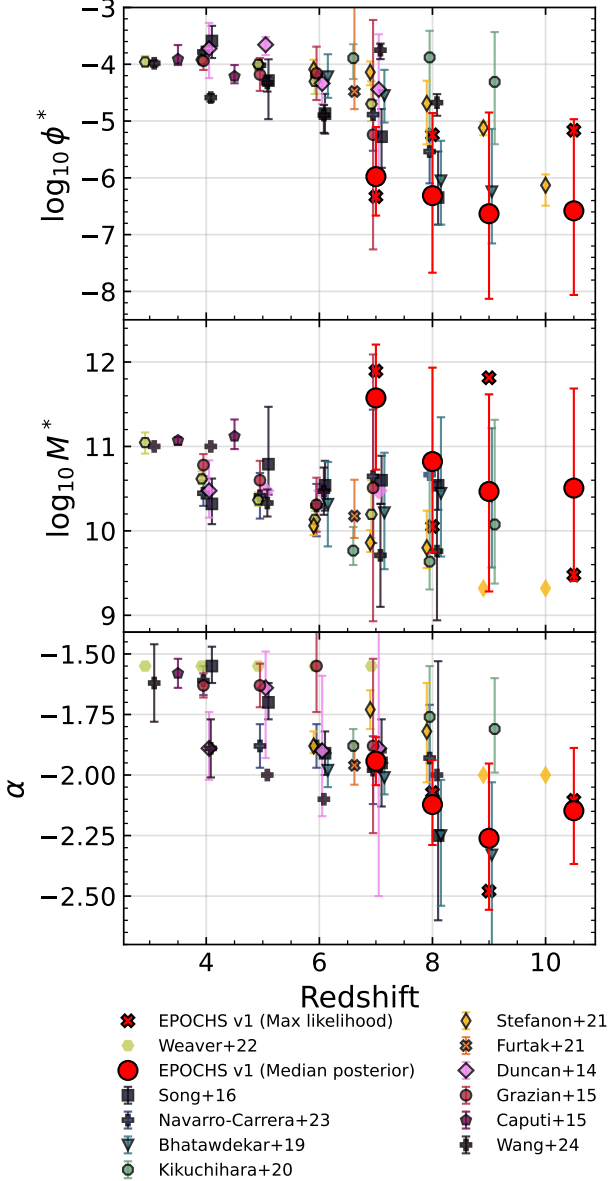


**Figure 10.** Evolution of best-fitting Schechter function parameters with redshift, with the results of this study shown by the red circles (median posterior) and red crosses (maximum likelihood). Comparisons to Duncan et al. (2014), Grazian et al. (2015), Caputi et al. (2015), Song et al. (2016), Bhatawdekar et al. (2019), Kikuchihara et al. (2020), Stefanon et al. (2021), Furtak et al. (2021), Weaver et al. (2022), and Navarro-Carrera et al. (2023) are shown. Markers showing literature values without black outlines were fixed during fitting.  $M^*$  values have been adjusted to reflect a Kroupa (2001) IMF.

et al. (2023) we propagate uncertainties in the inferred stellar mass density via a Monte Carlo integration of their SFRD measurements and uncertainties. Star formation is assumed to begin at  $z = 20$ , but the results

**Table 5.** Stellar mass density results from our fiducial *Bagpipes* SED fits calculated from the integral of the Schechter function for each redshift bin. Values with uncertainties come from the 16th, 50th and 84th percentiles of the posterior, and values in brackets are for the highest likelihood Schechter function. This table is available for download at <https://github.com/tHarvey303/EpochsIV>.

Redshift Bin	$\rho_*$ ( $\log_{10} M_{\odot} \text{ Mpc}^{-3}$ )
$6.5 < z \leq 7.5$	$6.36^{+0.14}_{-0.17}$ (6.42)
$7.5 < z \leq 8.5$	$5.52^{+0.14}_{-0.13}$ (5.51)
$8.5 < z \leq 9.5$	$5.03^{+0.18}_{-0.18}$ (5.02)
$9.5 < z \leq 11.5$	$4.93^{+0.18}_{-0.15}$ (4.85)

are relatively insensitive to the exact formation redshift as long as it exceeds the redshift  $z \geq 13.5$  limit used in this work.

The inferred stellar mass density is heavily dependent on the best-fitting Schechter function, and therefore indirectly dependent on the GSMF and stellar mass estimates. For the alternative GSMF estimates in § 6.5.6, we find that the use of the “continuity bursty” SFH, or stellar masses derived with our *Prospector* fitting, can increase the stellar mass density at redshift 10.5 by up to 0.75 dex, which is shown with a dashed errorbar. Similar variations are possible in the other redshift bins, but for simplicity we do not show every alternate GSMF and SMD derived for all redshift bins.

## 6. DISCUSSION

We have presented our fiducial GSMF using *Bagpipes* at redshifts  $6.5 \leq z \leq 13.5$ , finding a steep low mass slope ( $\alpha \lesssim -1.95$  and a high stellar mass exponential cutoff ( $M^* \gtrsim 10.5$ ) in all redshift bins. We have also estimated the stellar mass density implied by our results, finding an apparent flattening of the stellar mass density at  $z > 9$ . In the following section we will discuss our results in context of theory and previous work. This includes examining the uncertainties in the GSMF derived from our other SED fitting results, as well as considering how a modified top-heavy IMF or contamination by hidden AGN would affect our results.

### 6.1. Massive Galaxies in the Early Universe

Numerous studies have reported an excess of galaxies with high inferred stellar mass at high-redshift (Labbé et al. 2023; Endsley et al. 2023b; Akins et al. 2023; Xiao et al. 2023). If galaxies of the inferred masses do exist in the number densities implied by these studies, this could represent a challenge to  $\Lambda$ CDM cosmology or our understanding of high-redshift galaxy astrophysics, given the available timescale and available gas reservoirs (Labbé et al. 2023; Lovell et al. 2023; Boylan-Kolchin 2023).

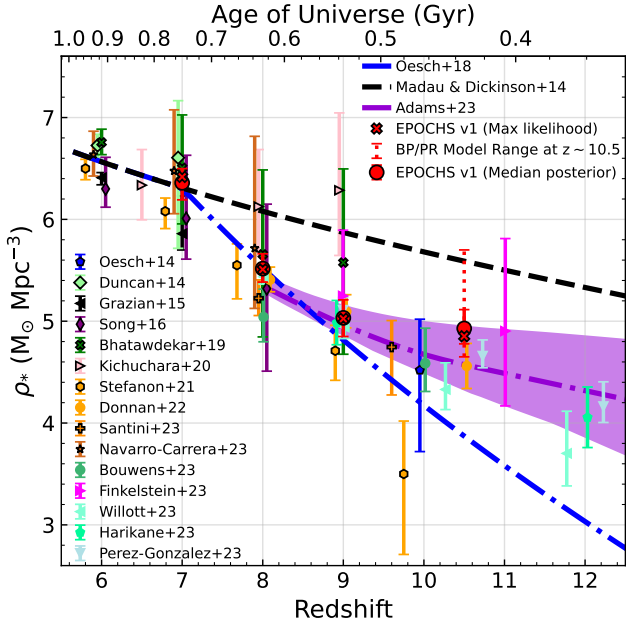


**Figure 11.** Stellar mass density as a function of redshift derived from the integration of the *Bagpipes* fiducial GSMF. Markers with black borders show comparisons to observational SMD results from Oesch et al. (2014); Duncan et al. (2014); Grazian et al. (2015); Song et al. (2016); Bhatawdekar et al. (2019); Kikuchihara et al. (2020); Weaver et al. (2022); Stefanon et al. (2021). Markers with colored borders show the results of integrating the SFRD predictions of JWST-era studies, which includes Donnan et al. (2022); Santini et al. (2022); Bouwens et al. (2023); Finkelstein et al. (2023b); Willott et al. (2023a); Harikane et al. (2023); Pérez-González et al. (2023). Where necessary we convert literature results to a Kroupa (2001) IMF. Markers may be shifted by up to  $\Delta z = 0.1$  for clarity. We also show the theoretical predictions of the Madau & Haardt (2015) (constant star formation efficiency) and Oesch et al. (2018) (DM halo evolution) models. The purple shaded area shows the integral of the SFRD presented by Adams et al. (2023) for our sample, which is consistent with the SMD derived from our *Bagpipes* SED fitting. The red dotted errorbar at  $z \sim 10.5$  shows the SMD range we find using different SED fitting tools and models, calculated from the Schechter fits in § 6.5.6. We do not show the range of models at every redshift, but it typically exceeds the uncertainty derived from the fit itself.

In order to test whether our derived stellar mass and redshift estimates are in tension with  $\Lambda$ CDM we use the Extreme-Value Statistics (EVS) approach, presented in Lovell et al. (2023) and available online<sup>6</sup>. We follow the methodology of Lovell et al. (2023) throughout this section. Given the total available area of our survey (187

<sup>6</sup> [github.com/christopherlovell/evstats](https://github.com/christopherlovell/evstats)

arcmin<sup>2</sup>) we have computed the halo distribution PDF and corresponding stellar mass PDF.

A universal baryon fraction of 0.16 is assumed based on cosmological results (Planck Collaboration et al. 2016), and we compute the EVS limits for a range of stellar fractions (fraction of baryons which form stars). In Figure 12 we show the stellar fraction upper limit of unity with a dashed line, as well as the more realistic predictions for stellar fraction, following a simple truncated lognormal PDF with  $\mu = e^{-2}$ ,  $\sigma = 1$ , with a dotted line and shaded contours. Overlaid on Figure 12 we show the SED-fitting derived redshifts and corrected stellar masses for our sample. We correct our derived stellar masses for Eddington bias (Eddington 1913) following  $\ln M_{Edd} = \ln M_{obs} + \frac{1}{2} \epsilon \sigma_{\ln M}^2$ .  $\ln M_{obs}$  is the stellar mass estimate,  $\sigma_{\ln M}$  is the uncertainty in the stellar mass taken from the posterior PDF, and  $\epsilon$  is the local slope of the halo mass function. Jespersen et al. (2024) looks at the impact of cosmic variance on the predictions of EVS, as this is not accounted for in the method of Lovell et al. (2023) we use here. Given that our sample consists of multiple widely-separated fields, we do not believe cosmic variance will play a significant role on this EVS analysis.

No galaxies in our sample fall above the limit imposed by a stellar fraction of unity, shown with a black line, which would require more stellar mass than the available baryons to form stars. The majority of the EPOCHS v1 sample are not in tension with the EVS limits and are shown with greyscale hexbins on Figure 12, shaded according to number density within the bin. For galaxies with redshift and stellar mass estimates which place them in possible tension with the EVS limits assuming a realistic stellar fraction (more than  $1.5 \times$  the mean value of the lognormal distribution, shown by the dashed-dot line in Figure 12) we overlay the individual mass measurements as points on Figure 12. For each of these galaxies we show the ‘fiducial’ *Bagpipes* photo- $z$  and stellar mass, as well as the maximum and minimum stellar mass estimate for that galaxy in our *Bagpipes* and *Prospector* fitting, including the modified IMF results we discuss in § 4.5. We link individual mass estimates for the same object with dotted lines. In the majority of cases, whilst the maximum stellar mass estimate may suggest a possible tension, the minimum and often the fiducial mass estimates are not in tension.

It is worth noting that all galaxies which show a possible tension at redshift  $z \leq 8$  in this figure are classed as ‘little red dots’ (LRDs), which are discussed further in § 5.2.3 and potentially contain a significant AGN component we do not account for. It is clear from Figure 12 that none of our candidates are in tension with the pre-

dictions of  $\Lambda$ CDM, as seen by the lack of sources above the solid black line, however a number of objects do require very high stellar fractions at these redshifts. The galaxies which require the highest star formation efficiencies seem to be found at  $z \sim 7 - 8$ , rather than the higher redshift probed in this study. This has also been found for HST-dark galaxies observed as part of FRESCO, where the galaxies with highest implied stellar mass densities are between  $5 \geq z \geq 6$  (Xiao et al. 2023).

Further evidence for the compatibility of our results with standard cosmological models can be seen in Figure 8, where we are below the SMF upper limit calculated by Li et al. (2023) in all redshift bins, which is shown with a black line. Li et al. (2023) present a bursty SFH model consisting of a series of feedback-free bursts (on timescales of  $\sim 10$  Myr per burst) for galaxies in halos above a given mass/redshift cutoff, resulting in higher star formation efficiency, cosmic SFR density and stellar mass density above  $z \geq 8$ . The upper limit shown is computed assuming a maximum star formation efficiency ( $\epsilon_{\max}$ ) of unity. Our fiducial GSMF results at  $z \approx 7$  are close to the FFB predictions with  $\epsilon_{\max} = 0.2$ , but fall below this value at higher redshifts.

Wang et al. (2024) have shown that stellar masses of high mass galaxies are typically overestimated by  $\sim 0.4$  dex when  $> 1\mu\text{m}$  rest-frame emission is not used in SED fitting, which requires MIRI observations in this redshift regime. As MIRI observations are not used in this study, the degeneracies in age-attenuation and the relative contributions of strong emission lines and the stellar continuum observed by Wang et al. (2024) are not constrained, possibly leading to an overestimation in stellar mass. Outshining and stochastic star formation are however still likely to have an effect on stellar masses derived from SED fitting, even when MIRI data is used (Narayanan et al. 2023; Shen et al. 2023), and the derived discrepancy in stellar mass without MIRI will likely depend on the assumed SFH, dust law and parameter priors, as we have shown they can also systematically change stellar mass estimates. Wang et al. (2024) also find that high mass galaxies at  $6 \leq z \leq 8$  may require a higher star formation efficiency ( $\epsilon \sim 0.3$ ) than the local Universe, but they do not find any incompatibility with standard cosmological models.

In Figure 3 we show examples of the photometry, best-fitting *Bagpipes* & *Prospector* SEDs, and posterior redshift and stellar mass estimates for a few of the most massive galaxies in the EPOCHS v1 sample at a range of redshifts. For the galaxy labelled *CEERS1:7463*, which is representative of the LRDs we observe, the inferred star formation history for the

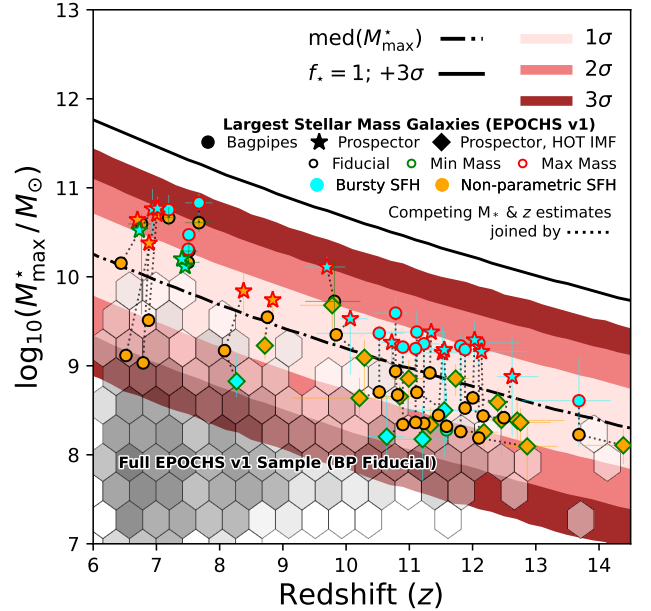


**Figure 12.** Photometric redshifts and stellar mass estimates for the EPOCHS v1 galaxy sample. We split the sample into two components, with the majority of galaxies shown by the grayscale hexbins. For the most massive galaxies we show individual datapoints in order to investigate possible tension with  $\Lambda$ CDM. We use the Extreme-value Statistics (EVS) methodology of Lovell et al. (2023) to calculate both the upper stellar mass limit assuming a stellar fraction of unity (shown with a black line), as well as a more realistic stellar fraction distribution parametrized by a truncated log-normal distribution with  $\mu = e^{-2}$  and  $\sigma = 1$  (median shown with a dash-dot line, colored contours show 1-3 $\sigma$  range). We assume a baryon fraction of 0.16 as predicted by Planck Collaboration et al. (2016) and use our full survey area of 187 arcmin<sup>2</sup> in the EVS calculation. For galaxies in the EPOCHS v1 sample with a stellar mass estimate greater than  $1.5\times$  the limit for a realistic stellar fraction (dash-dot line) we show the maximum, minimum and fiducial stellar mass and redshift estimates for our *Bagpipes* and *Prospector* fits, joined with a dotted black line. The shape and color of the points references the SED-fitting tool, SFH and IMF used, as explained by the inset legend. No galaxies exceed the maximum stellar mass predicted by  $\Lambda$ CDM, although some galaxies do require a high stellar fraction, particularly the ‘little red dots’ with high inferred masses at  $z \sim 7$ .

non-parametric SED fits suggest the bulk of stellar mass was formed  $\sim 100$ -200 Myr ago, which may put it and some of the other high-mass LRD galaxies in greater tension at  $\Lambda$ CDM at earlier points in their star formation histories, if the integrated SFH is considered. However we discuss in § 6.3, the masses and star formation histories of the LRDs are highly uncertain, particularly when their contribution of AGN is not considered.

### 6.2. Comparison of our sample to other studies

The study by [Labbé et al. \(2023\)](#) found a collection of unexpectedly massive, high-redshift galaxies in the CEERS field. These objects typically have blue colors in the short wavelength NIRCcam filters, but extremely red colors at longer wavelengths. We have cross-matched their 13 candidates to our catalogue in order to compare our derived masses and redshifts. In the following text we give both the ID in our catalogue followed by the ID given in [Labbé et al. \(2023\)](#) for the sources we discuss here. 11 of their candidates appear within our catalogue, of which 7 are selected by our selection criterion and are among the most massive galaxies we find. The two sources we do not recover appear to be blended with neighbouring sources in our `SExtractor` segmentation maps. Of the four that we detect but do not select, *5346\_CEEERSP6 (11184)* falls within our image mask (close to the detector gap in the NIRCcam SW observations), and the other three fail our signal to noise requirement in the rest-frame UV ( $\geq 5$  sigma). One of these, *2683\_CEEERSP3 (13050)*, has been spectroscopically confirmed as a broadline AGN by [Kocevski et al. \(2023\)](#) at  $z = 5.6$ . We do not detect *37888* or *39575*, which are among the lowest mass candidates presented in [Labbé et al. \(2023\)](#). We do not consider 2 of the selected galaxies in this study as their best-fitting redshift from `EAZY-py` is marginally below our  $z \geq 6.5$  limit. For these galaxies, *8750\_CEEERSP3 (7274)* and *2499\_CEEERSP1 (25666)*, we find lower redshift solutions than [Labbé et al. \(2023\)](#), with  $6.03^{+0.36}_{-0.14}$  and  $6.45^{+0.10}_{-0.18}$  vs their  $7.77^{+0.05}_{-0.06}$  and  $7.93^{+0.09}_{-0.16}$ . For four of the remaining five our photo- $z$  estimates agree well with [Labbé et al. \(2023\)](#), but for *1516\_CEEERSP2 (21834)*, we find a significantly higher photo- $z$  solution of  $10.4^{+1.3}_{-0.6}$  with `EAZY-py`. However our fiducial `Bagpipes` results, which incorporate the `EAZY-py` photo- $z$  posterior as a prior, suggest a photo- $z$  closer to  $8.63^{+0.24}_{-0.32}$ , which is in agreement with their result of  $8.54^{+0.32}_{-0.51}$ . For these five galaxies, our stellar mass estimates are on average a factor of  $2.1 \times$  (0.32 dex) smaller than [Labbé et al. \(2023\)](#), which is mostly due to the differing choice of IMF. [Madau & Dickinson \(2014\)](#) suggests a scaling factor of  $\approx 1.49 \times$  to convert a stellar mass estimate from [Salpeter \(1955\)](#) to [Kroupa \(2001\)](#), which does not account for the full discrepancy between our mass estimates.

The most massive candidate presented by [Labbé et al. \(2023\)](#), *7463\_CEEERSP1 (38094)*, with a stellar mass of  $\log_{10}(M_*/M_\odot) = 10.89^{+0.09}_{-0.08}$  is the second most massive galaxy in our sample, with a fiducial `Bagpipes` mass of  $10.65^{+0.09}_{-0.10}$ . Given that our sample contains  $5 \times$  the area of the dataset used in [Labbé et al. \(2023\)](#), this may

suggest that the CEERS field is overdense. As a comparison we compute the GSMF implied by the results of [Labbé et al. \(2023\)](#), assuming 100% completeness. The results of this are shown in [Figure 8](#). Their implied datapoint at both redshift 8 and 9 lies above our best-fitting Schechter functions, due to a combination of a smaller cosmic volume and higher stellar masses than our results. [Wang et al. \(2024\)](#) shows that the stellar masses of high- $z$  galaxies selected with the same color criteria as [Labbé et al. \(2023\)](#) are reduced by  $\sim 0.4$  dex when rest-frame  $> 1 \mu\text{m}$  observations from MIRI are included in SED fitting, suggesting that the stellar masses derived without MIRI data for the most massive galaxies in this work and in [Labbé et al. \(2023\)](#) may be systematically overestimated.

Although our source detection is done at the longest available wavelengths, our JWST sample is primarily selected in the rest-frame UV due to our Lyman-break criteria. Galaxies with weak UV emission may not be selected or even detected in our sample, whilst still containing significant stellar mass. Highly obscured galaxies like Submillimeter Galaxies (SMGs), which have high stellar masses, will not be included in our selection criteria, although they are thought to have a low spatial density (e.g. [Smail et al. 2023](#)).

Whilst high- $z$  galaxies are predicted to be relatively compact ([Roper et al. 2022](#); [Shen et al. 2024](#)), the high resolution of JWST and relatively small extraction apertures used also means we are more sensitive to compact, high-surface brightness sources than extended, low-surface brightness sources. If a population of extended, diffuse galaxies exists at these redshifts they are likely to be excluded from this sample.

### 6.3. Contamination of the GSMF by hidden AGN

As discussed in [§ 5.2.3](#), obscured high- $z$  AGN can impact the high-mass end of the GSMF at  $z = 7 - 8$  by masquerading as galaxies with evolved stellar populations and therefore higher masses. [Kokorev et al. \(2024\)](#) presents candidate LRDs in both the CEERS and GOODS-South fields, which covers the NGDEEP and JADES-Deep observations. We compare their catalogue to our high- $z$  galaxy sample, finding 5(3) of their CEERS (GOODS-South) candidates in our robust sample. They are all at  $z \leq 8$  in our sample, with IDs *1080\_CEEERSP9*, *2184\_CEEERSP1*, *4842\_CEEERSP6*, *7463\_CEEERSP1*, *7520\_CEEERSP5*, *6169\_JADES-Deep-GS*, *31738\_JADES-Deep-GS* and *36222\_JADES-Deep-GS*. It is worth noting that some of these galaxies in CEERS were first found in [Labbé et al. \(2023\)](#) and are discussed in [§ 6.2](#). We detect almost all of the  $z \geq 6.5$  galaxies from [Kokorev et al. \(2024\)](#) in the CEERS and

GOODS-South fields (18 and 10 respectively), but for the galaxies that do not appear in our final sample we either find a lower redshift solution (below our  $z \geq 6.5$  cutoff), or we do not robustly detect the Lyman break to  $5\sigma$ , meaning they do not meet our selection criteria. We see good agreement in redshift, with a maximum offset of  $\Delta z \approx 0.4$ , and a mean offset of  $\Delta z \approx 0.14$ . These galaxies are found to have high stellar masses in our SED-fitting, with a median stellar mass of  $\log_{10} M_*/M_\odot = 10.30$  in our fiducial `Bagpipes` results, with five of them forming the most massive galaxies in our fiducial sample. It is likely that at least some of these objects do contain AGN, which would lower the inferred stellar masses and hence lower the high-mass end of the GSMF. Further observations with NIRSpect or MIRI are essential to ascertain the true nature of these sources. In [Appendix A](#) we recompute the  $z = 7$  GSMF without any LRDs and show that these sources dominate the high mass end of the GSMF. [D’Silva et al. \(2023\)](#) has shown that accounting for the contribution of AGN lowers the cosmic star formation rate density by 0.4 dex at  $z \geq 9.5$ , which will also lower the inferred stellar mass density, and finds that a significant fraction of the LRDs are hidden AGN.

#### 6.4. Impact of Modified IMF

Our implementation of a modified top-heavy IMF in `Prospector` has been shown to reduce masses by up to  $\sim 0.5$  dex for galaxies at  $z \geq 12$  (HOT 60K) when compared to a standard [Kroupa \(2001\)](#) IMF, as shown in [Figure 5](#). The decrease in mass seen is also found to be dependent on the star formation model, with a larger decrease in stellar mass found when assuming a parametric “delayed” SFH model (0.46 dex) than when assuming a non-parametric “continuity bursty” SFH model (0.35 dex). Comparison of the best-fitting models has also shown that the  $\chi^2$  is almost unaffected by the change in IMF, suggesting the modified IMF models can match the observed photometry of the galaxies as well as the original data. We see similar results, with smaller decreases in stellar mass ( $\approx 0.3$  dex), for the modified IMF model used at  $8 < z < 12$  (HOT 45K).

There are a number of comparable studies which also look at the impact of a top-heavy IMF on the masses of high redshift galaxies. The most direct comparison can be made to the results of [Steinhardt et al. \(2023\)](#) as we have used the same top-heavy IMF model with a different SED fitting tool. Their results are based on some of the earliest JWST observations and they only fit a small number of galaxies. Direct comparison of their results to the default `EAZY-py fsp`s templates is also impacted by other differences between the two template

sets, including the re-parametrization of the IMF from [Chabrier et al. \(2000\)](#) to [Kroupa \(2001\)](#) and different assumptions for SFH and nebular emission. Our implementation changes only the IMF, with everything else modelled in the same way. They observe decreases of  $0.5 - 1$  dex in stellar mass, whereas our implementation sees smaller decreases, typically from  $0.3 - 0.5$  dex. The reason for this discrepancy is unclear, but it may be possible that the other differences between the standard `EAZY-py` templates and their models have a larger effect on the stellar mass than expected, or that the change in IMF in our modelling resulted in different star formation histories that acted to somewhat decrease the impact of the modified IMF.

[Woodrum et al. \(2023\)](#) also look at other top-heavy modifications to commonly used IMF parametrizations using `Prospector`. They look at a modification to the [Chabrier et al. \(2000\)](#) IMF, rather than the [Kroupa \(2001\)](#) we use, but they find comparable reductions in stellar mass (between 0.38 and 0.5 dex). They also see no change in the goodness of fit when using a modified IMF.

Whilst we have shown that a modified top-heavy IMF can decrease the stellar masses of high- $z$  galaxies, with no change in the simulated photometry, our analysis of the  $\Lambda$ CDM limits on the growth of stellar mass in [§ 6.1](#) does not require a non-standard IMF in order to be compatible with  $\Lambda$ CDM. In [Figure 1](#) we have shown that the stellar masses can vary significantly with other SED fitting assumptions (dust law, assumed SFH), before any IMF change is considered. For the galaxies with high stellar masses across all the models we consider, it is not possible to distinguish between a modified IMF or simply a high star formation efficiency based on photometry alone.

#### 6.5. Comparing the measured GSMF with other observations and theory/simulations

In [Figure 8](#), we compare our GSMF estimates to a wide-range of observational and theoretical/simulation based predictions of the GSMF. Here we briefly discuss our GSMF estimates for each of the redshift bins. In order to make direct comparisons where necessary all results have been converted to use a [Kroupa \(2001\)](#) IMF.

The overall evolution of the derived Schechter parameters and a comparison to the results derived by other studies can be seen in [Figure 10](#). Whilst the Schechter parameters are highly covariant, and our results typically have large uncertainties, we observe an evolution in  $\alpha$  and  $\phi^*$  compared, with both parameters decreasing compared to the results at  $z \sim 4$  of [Caputi et al. \(2015\)](#), [Duncan et al. \(2014\)](#) and [Grazian et al. \(2015\)](#).

We see little evolution of  $M^*$  within the large range of uncertainties.

#### 6.5.1. Redshift $z=7$ GSMF

We derive a mass function at  $z \sim 7$  primarily as a proof of concept of our method. We do not take advantage of galaxy lensing in this work, so any reasonable mass completeness limit is higher than previous studies, nor do we have the area of wide-field studies like Weaver et al. (2022) in order to detect rare, bright and high mass galaxies. However with JWST we have seen a surprising excess of UV-faint LRD like objects with high inferred stellar masses, as discussed in § 6.3. The majority of these sources were previously undetected with HST due to relatively weak Lyman-breaks, and so do not appear in pre-JWST stellar mass estimates. Their inclusion in our GSMF has resulted in an excess at the high mass end of the GSMF when compared to other observational studies, and consequently a higher and poorly constrained estimate of  $M^*$ , as we see little evidence for any exponential turnover. The highest mass GSMF data-points of Weaver et al. (2022) fall within our  $1-\sigma$  uncertainty region, but our results are significantly above the measurements of Stefanon et al. (2021). At the low-mass end we fall below the results of Kikuchi-hara et al. (2020) and Navarro-Carrera et al. (2023), but agree within the uncertainties of Furtak et al. (2021) and Bhatawdekar et al. (2019). Stefanon et al. (2021); Kikuchi-hara et al. (2020); Bhatawdekar et al. (2019) and Furtak et al. (2021) are all based on HST+Spitzer observations of the Hubble Frontier Fields, and incorporate lensing, which means they probe the low mass end of the GSMF more accurately than this study. Our low mass slope  $\alpha = -1.94_{-0.1}^{+0.1}$  is in good agreement with Furtak et al. (2021), but steeper than the results Stefanon et al. (2021) and Kikuchi-hara et al. (2020). At the time of writing, Navarro-Carrera et al. (2023), Gottumukkala et al. (2023) and Wang et al. (2024) are the only other studies to incorporate JWST observations into their GSMF estimates. We see reasonable agreement with the results of Navarro-Carrera et al. (2023) as our data is within their GSMF uncertainties. This work relies almost entirely on JWST observations, whereas they combine deep JWST observations of small volumes ( $\leq 20$  arcmin<sup>2</sup>) with HST and ground-based catalogues. This ground-based data allows them to find more rare, high-mass galaxies than our study, but at lower masses the small volumes probed with their JWST data are potentially vulnerable to cosmic variance. Reliance on ground-based and HST data also limits the maximum redshift they can probe to  $z \leq 8$ . Wang et al. (2024) uses PRIMER observations with NIRCcam and MIRI to mea-

sure the GSMF, notably finding that the use of MIRI observations systematically reduces stellar masses measured with SED fitting. We see good agreement in the measured GSMF within the uncertainties of both studies, despite this work not incorporating MIRI data or correcting for any systematic offset in mass arising from the lack of restframe  $> 1\mu\text{m}$  observations. Our GSMF does extend to higher stellar mass than the result of Wang et al. (2024), resulting in a higher value for  $M^*$ , as can be seen in Figure 10.

Gottumukkala et al. (2023) examine the contribution of high-mass, dusty galaxies at  $3 < z < 8$  to the GSMF using data from the CEERS survey. Given that our GSMF probes a wider galaxy population, we do not expect to see overlap at all stellar masses. We see good overlap at the highest stellar masses  $M_{\odot} \sim 10^{10.5}$ , where our SMF estimate is dominated by dusty LRD galaxies (as discussed in § 6.3).

When we compare to predictions from models and simulations, we see agreement with the majority of models at the low-mass end but a significant excess at higher masses that is not reproduced by any of the models. We find in particular that the JAGUAR model we use for our completeness simulations shows a more rapid decline at high stellar mass than the other models, but given that we are not reliant on our completeness correction in this mass regime this does not impact our estimate of the GSMF. We are closest to the prediction of *Universe Machine* (Behroozi et al. 2019) at the highest stellar mass bin.

#### 6.5.2. Redshift $z=8$ GSMF

Our fiducial GSMF estimate at  $z \sim 8$  shows reasonable agreement with most predictions. As we do not bootstrap in redshift when constructing the GSMF, we do not account for galaxies scattering between redshift bins, and for example a galaxy found to be at  $z = 7.49$  with Bagpipes would contribute only to the  $z = 7$  GSMF, even in a significant fraction of the redshift PDF is above  $z \geq 7.50$ . This does not affect the majority of galaxies within our sample, but it does explain some of the discrepancy between our results and the implied results of Labbé et al. (2023), shown in purple in Figure 8 assuming 100% completeness. The LRD galaxies of Labbé et al. (2023) which we also select are all found to be at  $z \leq 7.5$ , meaning they do not contribute at all to our estimate of the  $z = 8$  GSMF. The best-fitting redshift for these objects in some cases is quite close to this boundary however, meaning that these objects could theoretically contribute to the  $z = 8$  GSMF instead, which would boost the high-mass end significantly. Our GSMF is also lower than the results of Kikuchi-hara



et al. (2020), which incorporates strong gravitational lensing in order to probe to lower stellar mass. Our GSMF agrees with the results of Song et al. (2016); Bhatawdekar et al. (2019); Stefanon et al. (2021), and appears to validate the majority of pre-JWST GSMF estimates. We can also draw a comparison to the results of Wang et al. (2024), whose GSMF results at  $z = 8$  are systematically above our results, but within the derived uncertainties of both studies.

We see good agreement with most theoretical predictions of the GSMF at this redshift, with *Universe Machine* (Behroozi et al. 2019), *SC SAM GUREFT* (Yung et al. 2023) and *FLARES* (Lovell et al. 2021; Wilkins et al. 2023b) having the most similar results.

### 6.5.3. Redshift $z=9$ GSMF

Our GSMF estimate at  $z \sim 9$  is below the results of Bhatawdekar et al. (2019) and Kikuchihara et al. (2020), but within the uncertainties of Stefanon et al. (2021). We are below the implied result of Labbé et al. (2023), which is derived from two galaxies in their sample in this redshift bin, but assuming 100% completeness. We include one of these galaxies in our GSMF at this redshift, as the other does not meet our selection criteria, as we do not detect the Lyman break at  $5\sigma$ . We additionally include one other candidate from their sample in this GSMF, as our fiducial *Bagpipes* photo- $z$  places it within this redshift bin, rather than the  $z \sim 8$  redshift bin based on their photo- $z$ . For both of their galaxies we do include in this redshift bin we find  $\sim 0.4$  dex lower stellar masses, meaning they contribute to a lower stellar mass bin. Our reliance on the rest-frame UV to robustly detect sources is one limitation of this work, although the increased depth of JWST observations when compared to HST has reduced this in some fields. We investigated less-stringent constraints on the Lyman-break, but found that this dramatically increased rates of contamination within our sample. When compared to simulations, *FLARES* and *Universe Machine* are close to our GSMF estimate, but almost all the predictions are within our posterior region. Interestingly, in this redshift bin we are below the predictions of two recent JWST-era studies; Mauerhofer & Dayal (2023) and Li et al. (2023), both of which incorporate higher star formation efficiencies than typical models.

### 6.5.4. Redshift $z=10.5$ GSMF

At  $z \sim 10.5$  observational comparisons can be made only to the pre-JWST results of Stefanon et al. (2021). In comparison to their results we find a significant excess of high mass galaxies in our observations. Our results show that above  $z \geq 10$  JWST observations are essential to accurately sample the high- $z$  galaxy population.

Our results are above the majority of theoretical and simulation-derived predictions, but do show good agreement with *Universe Machine* (Behroozi et al. 2019) and *FLARES* (Lovell et al. 2021; Wilkins et al. 2023b).

### 6.5.5. Redshift $z=12.5$ GSMF

In our highest redshift bin,  $11.5 < z \leq 13.5$  which covers only  $\approx 80$  Myr, there are no published observationally-derived results and few theoretical or simulation-based GSMF comparisons at this redshift. Pre-JWST estimates of the GSMF were not possible at this redshift, and even with JWST our GSMF estimate is also uncertain due to the difficulty in accurate stellar mass estimates as well as the possible contribution of contaminants. At  $z = 12.5$  the longest wavelength NIRCcam filter falls within the rest-frame UV, which is dominated by young stars, leading to highly uncertain star formation histories and stellar masses. As we explored briefly in § 4.5, the more likely possibility of a top-heavy IMF or exotic stellar populations in these early galaxies further increases the systematic uncertainties in the stellar mass estimates. An example of three galaxies within this redshift bin is shown in the lower plot of Figure 3 and in Figure 4, and the range of stellar mass estimates ( $\sim 0.8 - 1$  dex) for different *Bagpipes* and *Prospector* with very little difference in the fitted rest-UV spectra shows the difficulty in estimating stellar mass at these redshift. Previous studies at lower redshift with HST and Spitzer have found that stellar masses estimated by HST alone, with no measurement of the rest optical emission, typically underestimate stellar masses by 0.62 dex, compared to measurements including HST and Spitzer NIR observations (Furtak et al. 2021). At this redshift range, our JWST NIRCcam observations are probing comparable rest-frame UV wavelengths to HST observations at  $z \sim 6 - 7$ , and it possible that our stellar masses are also underestimated unless there is a significant change in stellar populations or IMF. The possibility of more stochastic star formation histories at this redshift compared to  $z \sim 6 - 7$  may also lead to outshining, which further increases the stellar mass discrepancy (Narayanan et al. 2023).

We note that several galaxies in this bin have been excluded from the GSMF in this case due to our requirement that the contamination is less than 50%. The inclusion of these possible contaminants would result in an  $\approx 0.3$  dex increase in the lowest mass bin. The results of this are shown in Appendix C. Whilst we do not attempt to fit the GSMF, we can make approximate comparisons to the few available predictions. We see the closest agreement with *DELPHI* (Mauerhofer & Dayal 2023) and are within  $1.5\sigma$  of *FLARES* (Lovell

et al. 2021; Wilkins et al. 2023b) in the higher mass bin, but have an excess of  $\approx 10^8 M_\odot$  galaxies when comparing to *FLARES* and *SC SAM GUREFT* (Yung et al. 2023). Our results are significantly above the predictions of *BLUETIDES* (Feng et al. 2016; Wilkins et al. 2017) at all stellar masses. Our fiducial GSMF prediction is slightly below the prediction of Li et al. (2023) with maximum star formation efficiency  $\epsilon_{\max} = 0.2$ , and significantly below the upper limit of  $\epsilon_{\max} = 1$ .

#### 6.5.6. Alternative GSMF Estimates

Following on from the comparison of galaxy stellar mass estimates with different choices of SFH and priors in § 4.3, it is possible to estimate the GSMF for any of the different SED-fitting models. A full comparison of the derived GSMF for every model, given the many possible combinations of possible IMF and SFH models, is beyond the scope of this work, but we give a representative example of the GSMF derived at  $z \sim 10.5$  for the models which show the most variation in stellar mass when compared to our fiducial *Bagpipes* fitting. Here we choose to investigate the GSMF dependence on the chosen SFH model and SED fitting tool, rather than the choice of parameter prior or dust law. This is because in § 4.3, there was larger variation in stellar mass with little variation in  $\chi^2$  for these alternative models. Additionally, as discussed, the use of non-parametric SFHs is more common in the literature (e.g. Tacchella et al. 2022; Giménez-Arteaga et al. 2023; Jain et al. 2024; Giménez-Arteaga et al. 2024) for high- $z$  galaxies due to problems such as outshining.

We derive these GSMF estimates using the same method as described in § 5 for the fiducial *Bagpipes* GSMF, replacing the stellar mass PDFs, best-fitting SEDs and redshift estimates with those of the chosen model. § 6.5.6 shows a comparison of the fiducial *Bagpipes* GSMF to a GSMF derived from the “continuity bursty” non-parametric SFH model, which increases the stellar mass estimates by 0.2 dex on average, but  $\geq 1$  dex in some cases. This results in the largest change in the overall GSMF when compared to the fiducial *Bagpipes* result.

We also show mass functions derived from our *Prospector* SED-fitting, which are offset above our fiducial *Bagpipes* GSMF for both the parametric and non-parametric results. These results are somewhat comparable to the spread seen in the *Bagpipes* results, although the low-mass end of the GSMF in the “continuity bursty” SFH model produces a shallower slope than the other models. Crucially we can see that the derived GSMFs are in tension with each other, and do not typically fall within the confidence intervals across

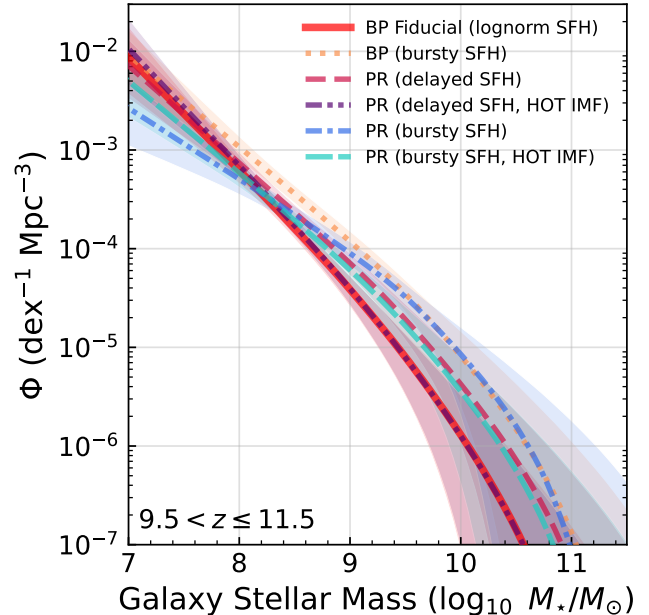


**Figure 13.** GSMF Schechter parametrization for the  $z \sim 10.5$  redshift bin derived for our fiducial *Bagpipes* SED-fitting compared to alternative GSMF estimates. We show the GSMF derived using *Bagpipes* with the non-parametric “continuity bursty” SFH (labelled ‘bursty’) as well as for two GSMFs derived using *Prospector* SED-fitting for a parametric and non-parametric SFH. We also show for comparison the GSMF inferred with the alternative top-heavy IMF model. The derived GSMF is clearly dependent on the choice of model and SED fitting tool, with the “continuity bursty” SFH model typically shifting the GSMF towards higher stellar mass. These Schechter functions are tabulated in Appendix B.

the majority of the stellar mass range. This is consistent with Wang et al. (2023b), who argue that the stellar mass uncertainties are typically underestimated by SED fitting procedures.

The change in inferred stellar mass we observe with a modified IMF does not appear to vary strongly with stellar mass, so the the impact on the GSMF can generally be seen as a shift towards lower stellar mass of 0.3 – 0.4 dex. This is comparable in magnitude and opposite in direction to the shift seen when moving from *Bagpipes* to *Prospector* when using a parametric SFH, which results in little overall change in the resulting GSMF.

Resolved SED fitting from Giménez-Arteaga et al. (2023) has found that the higher stellar masses inferred by the non-parametric SFHs can better account for the out-shining of older stellar populations in bright, actively star forming galaxies. How widespread the issue of outshining is among our sample is unknown, but if it is common then the masses and resulting GSMF of the

“continuity bursty” SFH model may more accurately recover the true stellar populations of these early galaxies.

These results demonstrate the overall systematic uncertainty different assumptions cause in the GSMF which are not represented by the uncertainty contours. Most GSMF estimates do not consider the overall uncertainty introduced by the assumptions of their modelling, which often dwarfs the statistical uncertainty in the fit itself. The variation in the derived GSMF can also significantly impact the implied SMD, as discussed in the next section.

### 6.6. *Stellar Mass Density Evolution in the Early Universe*

The growth of stellar mass density in the early Universe is highly uncertain. Some observational studies (e.g. Oesch et al. 2014; Stefanon et al. 2021; Willott et al. 2023a) have found a sharp decline in stellar mass density at  $z \geq 8$ , whereas others see a flatter evolution (Kikuchihara et al. 2020; Bhatawdekar et al. 2019). On the theoretical side, Oesch et al. (2018) uses dark matter halo evolutionary models to predict a deviation from the constant star formation efficiency (CSFE) model of Madau & Haardt (2015), which follows a significantly steeper slope at  $z \geq 7$ .

Our results from our fiducial **Bagpipes** model fall between the predictions of Madau & Haardt (2015) and Oesch et al. (2018). We see a flatter evolution with redshift than predicted with (Oesch et al. 2018), but an overall lower stellar mass density than the CFSE model of Madau & Haardt (2015). For our other GSMF estimates at  $z = 10.5$ , shown in § 6.5.6, we find that  $\rho_*$  increases by up to 0.75 dex, which would bring it closer to the constant star formation efficiency prediction of Madau & Haardt (2015). Whilst we do not show the SMD scatter measured in other redshift bins, we typically see the same behaviour at  $z > 7$ , with our fiducial **Bagpipes** SMD result producing lower  $\rho_*$  estimates than our alternative models. With our fiducial **Bagpipes** results we see significant evolution of the GSMF between  $z = 7$  and  $z = 8$ , with  $\rho_*$  decreasing by  $\sim 0.85$  dex. However we see a significantly flatter evolution in the SMD derived from the “continuity bursty” model GSMF, with a decrease of only  $\sim 0.4$  dex across the same redshift range. This is due partly to the overall increase in stellar mass estimates observed with this SFH model when compared to our fiducial model, as detailed in § 4.3, but is also due to the scattering of the high-mass LRD galaxies scattering between the  $z = 7$  and  $z = 8$  redshift bins due to uncertain photo- $z$  estimates, which significantly impacts the GSMF at higher stellar masses.

We see a good agreement between the integration of the star formation rate density of Adams et al. (2023), which uses the same sample, and our fiducial SMD results. There are very few JWST-era GSMF estimates to directly compare against, and so we have computed the inferred stellar mass density based on the integral of the cosmic star formation rate density of other studies. We note however the numerous works showing the increased scatter in mass-to-light ratios observed due to bursty star formation (Santini et al. 2022; Asada et al. 2023), which will impact the assumptions made to convert these UV luminosity densities into stellar mass densities.

In Figure 11 we show the overall stellar mass density range we find when we use a different SED fitting tool or star formation history model (dotted red uncertainty). This is significantly larger than the statistical uncertainty in the stellar mass density from our fiducial **Bagpipes** results. A change of up to 0.75 dex at  $z \approx 10.5$  is possible, when only the SED fitting tool or SFH model is varied and the overall sample is unchanged. More significant variations are possible between the results of independent studies, which also have to consider differences in reduction, source detection, photo- $z$  estimation, selection procedure, cosmic variance, and completeness corrections. Not accounting for the contribution of AGN to the observed photometry may cause overestimation of the stellar mass density at high-redshift (D’Silva et al. 2023).

The range of stellar mass densities possible with our alternative GSMF estimates at  $z \sim 10.5$  is mostly above the  $1\sigma$  range of Adams et al. (2023). A discrepancy between the integrated star formation rate density and stellar mass density measured for the same sample could hint at a different IMF, since the assumed return fraction is strongly dependent on the chosen IMF, and the SMF and UVLF probe different stellar populations with different characteristic stellar mass. However there are a number of other possible issues with the conversion of the UVLF into a SMD estimate; the conversion of UV flux to SFR ( $\kappa_{UV}$ ), is often assumed to be a constant factor but actually dependent on the age and metallicity Madau & Dickinson (2014), as well as the other assumptions used to calculate the return fraction (closed-box model, constant IMF & metal yield and instantaneous recycling of metals) which may not be valid at high-redshift.

As we show in § 4.3, in some cases discrimination between models or priors based on the goodness of fit may be possible, but in others (e.g. assumed SFH model), significant scatter in stellar mass estimates are possible with no difference in  $\chi^2$ . Other studies which use only

one method for measuring stellar mass estimates will underestimate the overall uncertainty in the derived GSMF and stellar mass density estimates.

## 7. CONCLUSIONS

In this paper we present an investigation into the properties of the EPOCHS v1 sample of 1120 high-redshift galaxies at  $6.5 \leq z \leq 13.5$  taken from a uniform reduction of 187 arcmin<sup>2</sup> of JWST data, including the GTO program PEARLS as well as other public ERS/GO JWST programs.

We examine the consistency of galaxy properties, including stellar mass, under different assumptions and using different SED fitting tools, including `Bagpipes` and `Prospector`. In particular we examine the impact of different SFH parametrizations as well as switching between a parametric and non-parametric SFH models. We also investigate the possible reduction in stellar mass when assuming a top-heavy IMF. We then use this sample and our range of stellar mass estimates to construct possible realisations of the galaxy stellar mass function. Lastly we integrate our mass function estimates to probe the buildup of stellar mass in the early Universe via the stellar mass density.

The major conclusions from this study are as follows:

1. We find that the stellar mass of high-redshift galaxies can depend strongly on assumed models, their priors and the SED fitting package used. In particular the estimated stellar mass can increase by  $>1$  dex when a parametric SFH is exchanged for a non-parametric SFH, with no change in the goodness of fit. Higher stellar mass discrepancies are seen at  $z > 10$  due to a lack of rest-optical emission.
2. We find that the assumption of a modified top-heavy [Kroupa \(2001\)](#) IMF, which may more accurately model the hot star-forming regions within high- $z$  galaxies, can reduce stellar mass estimates by up to 0.5 dex with no impact on the goodness of fit.
3. Whilst some of the stellar mass estimates imply a high star formation efficiency, in our analysis of the most massive galaxies in our sample using the Extreme-Value Statistics methodology of [Lovell et al. \(2023\)](#) we do not find any galaxies which are incompatible with the existing  $\Lambda$ CDM cosmology. The largest stellar mass estimates are typically found when fitting the non-parametric SFH models, and often can be significantly reduced with an alternative model. We not require a top-heavy IMF
4. Across all of the fitted models, the highest mass galaxies in our sample are ‘Little Red Dots’, with inferred masses of  $>10^{10} M_{\odot}$  at  $z \approx 7$ . These galaxies dominate the highest mass bins of our galaxy stel-

lar mass function (GSMF) estimates, so understanding their true stellar populations and accounting for the likely contribution of AGN ([Greene et al. 2023](#); [Furtak et al. 2023](#); [Furtak et al. 2023](#)) will be essential to more accurately constrain further GSMF estimates.

5. With the GSMF derived from our fiducial `Bagpipes` results, we typically see good agreement with existing constraints on the GSMF at  $z \leq 9.5$ . At the limits of HST+Spitzer ( $z \geq 10$ ) we see an excess of galaxies when compared to pre-JWST observations, but our GSMF results fall within predictions of simulations and theory.
5. The systematic variation in stellar mass estimates we find can dramatically impact the inferred galaxy stellar mass function and therefore the stellar mass density. We show that the choice of star formation history model or SED fitting tool can cause up to a 0.75 dex shift in the overall stellar mass density at  $z \approx 10.5$  with the same sample of galaxies. We predict larger offsets between independent samples, where different reductions, selection techniques and photo- $z$  estimates will increase the uncertainties.
6. We see a flatter evolution of the cumulative stellar mass density than predicted by dark matter halo evolution models, whilst the slope of our results is more consistent with constant star formation efficiency models. Our results suggest that significant stellar mass had already formed at  $z \geq 11.5$ .

This is only the beginning of GSMF estimates at  $z > 10$ , and the use of ultra-deep observations (the second NGDEEP epoch ([Bagley et al. 2023a](#)), the JADES Origins Field ([Eisenstein et al. 2023b](#); [Robertson et al. 2023a](#)) and others) and magnification by lensing clusters (PEARLS, UNCOVER, CANUCS; [Windhorst et al. 2023](#); [Bezanson et al. 2022](#); [Willott et al. 2023b](#)) will help constrain the GSMF at stellar masses below our completeness limit of  $\sim 10^8 M_{\odot}$ , whilst widefield surveys (e.g. PRIMER, UNCOVER, Cosmos-Webb; [Dunlop et al. 2021](#); [Bezanson et al. 2022](#); [Kartaltepe et al. 2021](#)) will add area and rare higher-mass sources. Deep MIRI F560W or F770W observations (e.g. the MIRI HUDF survey, [Norgaard-Nielsen & Perez-Gonzalez 2017](#)) will be crucial to provide better constraints on stellar mass estimates at these redshifts by extending the wavelength range further into the rest-frame optical, although the sensitivity of MIRI decreases rapidly with increasing wavelength (e.g. [Wang et al. 2024](#)). More complete NIR-Spec coverage is also important to identify interlopers, confirm photometric redshifts and distinguish between AGN emission and star forming galaxies.

All of the raw JWST data used in this work are the same as used in [Adams et al. \(2023\)](#) and can be accessed via this MAST DOI: DOI 10.17909/5h64-g193.

All proprietary data from the PEARLS program will all become accessible over 2024. Catalogues for all high- $z$  galaxies will be published with the EPOCHS I paper (Conselice et. al., in prep). The fiducial GSMF and SMD results from this work are available on [GitHub](#), and results for our alternative models will be made available upon request.

1 TH, CC, NA, DA, QL, JT, LW acknowledge support  
 2 from the ERC Advanced Investigator Grant EPOCHS  
 3 (788113), as well as two studentships from the STFC.

4 AZ acknowledges support by Grant No. 2020750  
 5 from the United States-Israel Binational Science Foun-  
 6 dation (BSF) and Grant No. 2109066 from the  
 7 United States National Science Foundation (NSF); by  
 8 the Ministry of Science & Technology, Israel; and  
 9 by the Israel Science Foundation Grant No. 864/23.  
 10 RAW, SHC, and RAJ acknowledge support from NASA  
 11 JWST Interdisciplinary Scientist grants NAG5-12460,  
 12 NNX14AN10G and 80NSSC18K0200 from GSFC. CCL  
 13 acknowledges support from the Royal Society under  
 14 grant RGF/EA/181016. The Cosmic Dawn Center  
 15 (DAWN) is funded by the Danish National Research  
 16 Foundation under grant No. 140. CNAW acknowledges  
 17 funding from the JWST/NIRCam contract NASS-0215  
 18 to the University of Arizona. M.N. acknowledges INAF-  
 19 Mainstreams 1.05.01.86.20. CNAW acknowledges sup-  
 20 port from the NIRCam Development Contract NAS5-  
 21 02105 from NASA Goddard Space Flight Center to the  
 22 University of Arizona.

23 This work is based on observations made with  
 24 the NASA/ESA *Hubble Space Telescope* (HST)  
 25 and NASA/ESA/CSA *James Webb Space Telescope*  
 26 (JWST) obtained from the Mikulski Archive for  
 27 *Space Telescopes* (MAST) at the *Space Telescope Sci-*  
 28 *ence Institute* (STScI), which is operated by the Asso-  
 29 ciation of Universities for Research in Astronomy, Inc.,  
 30 under NASA contract NAS 5-03127 for JWST, and  
 31 NAS 5-26555 for HST. The authors thank all involved  
 32 with the construction and operation of JWST, without  
 33 whom this work would not be possible. We also thank  
 34 the PI's and teams who designed and executed the  
 35 ERS, GTO and GO programs used within this work,  
 36 including PEARLS (1176, 2738), SMACS-0723 (2737),  
 37 GLASS (1324), CEERS (1345), JADES (1180, 1210,  
 38 1895, 1963) and NGDEEP (2079).

39 This work makes use of `astropy` (Astropy Collabo-  
 40 ration et al. 2013, 2018, 2022b), `matplotlib` (Hunter  
 41 2007), `reproject`, `DrizzlePac` (Hoffmann et al. 2021),  
 42 `SciPy` (Virtanen et al. 2020) and `photutils` (Bradley  
 43 et al. 2022).

## APPENDIX

### A. $Z = 7$ STELLAR MASS FUNCTION WITHOUT ‘LITTLE RED DOTS’

As discussed in § 6.3, the ‘Little Red Dots’ (LRDs) dominate the high mass end of our GSMF at  $z = 7$ . As the contribution of AGN to their photometry is still somewhat uncertain, and likely differs on an individual basis between galaxies, in the main results of this paper we do not remove LRDs from the GSMF estimates, or account for any

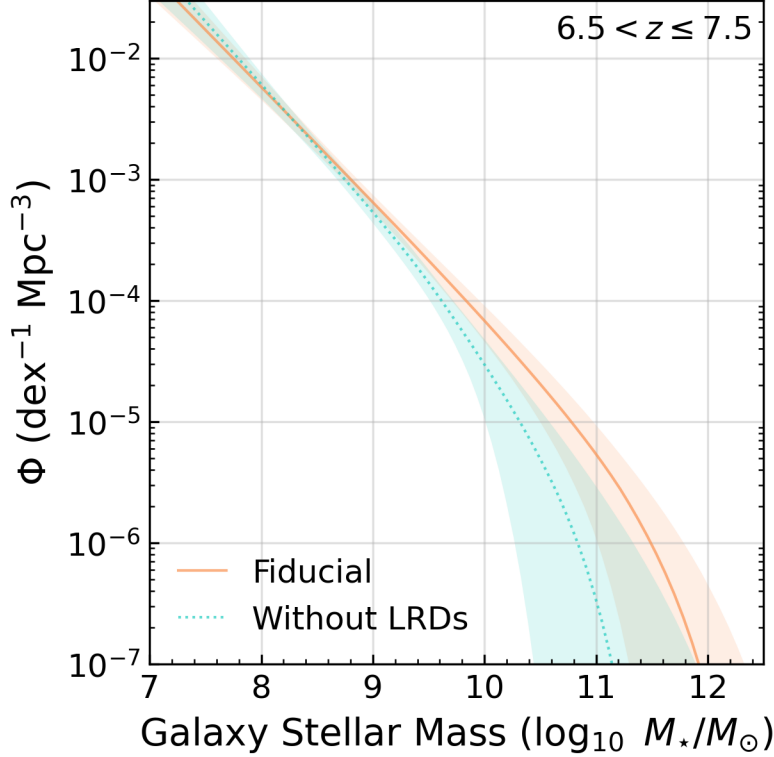


**Figure 14.** Galaxy Stellar Mass Function at  $6.5 < z \leq 7.5$ , excluding all ‘Little Red Dots’, compared to our fiducial **Bagpipes** results.

possible AGN emission. In this Appendix we briefly present the alternative case, where we remove all objects which meet the color-color selection criteria of [Kokorev et al. \(2024\)](#) and reconstruct the  $z = 7$  GSMF.

When we apply their ‘*red2*’ color selection, compactness criterion and SNR requirements to our robust sample, we find 34 galaxies which meet these cuts. There are 13 in the NEP-TDF, 17 in CEERS, 3 in the JADES DR1 field, and 1 in the NGDEEP field. The median redshift is 7.16, with all candidates falling between  $z = 6.5$  (our redshift cut) and  $z = 8.7$ . The median fiducial **Bagpipes** stellar mass is  $\log_{10} M_*/M_\odot = 8.90$ , with a maximum stellar mass of  $\log_{10} M_*/M_\odot = 10.70$ .

We exclude these 34 candidates from our sample and reconstruct the stellar mass function at  $z = 7$ . No other changes are made to our GSMF construction or fitting procedures. [Figure 14](#) shows the GSMF derived without including any ‘Little Red Dots’. Compared to the fiducial GSMF, this removes the two highest mass bins entirely, which demonstrates our reliance on these galaxies at the high mass regime. In terms of the derived Schechter parameters, the exponential mass cutoff  $M^*$ , which is not well constrained, decreases from  $11.57^{+0.63}_{-0.85}$  to  $10.64^{+1.25}_{-0.98}$  when we exclude the LRDs. The median posterior  $\phi^*$  and  $\alpha$  for the GSMF without LRDs are  $-5.40^{+1.34}_{-1.43}$  and  $-2.04^{+0.18}_{-0.13}$  respectively.

#### B. TABULATED SCHECHTER PARAMETERS FOR ALTERNATIVE GSMF ESTIMATES AT $Z = 10.5$

We give the Schechter function parameters for our alternative GSMF fits at  $z \sim 10.5$  in [Table 6](#). These are the Schechter parameters representing the fits shown in [§ 6.5.6](#). These GSMF estimates are equivalent to the fits given in [Table 3](#) for the fiducial GSMF, and are calculated using the same method, simply replacing the redshift and stellar mass PDF used in constructing the GSMF with those derived under the alternate SED fitting assumptions.

#### C. $Z = 12.5$ GSMF WITH NO CONTAMINATION LIMIT

Our fiducial GSMF applies a 50% contamination limit on all galaxies. Given the fields a galaxy is selected in and its stellar mass, our **JAGUAR** contamination simulation computes a likelihood of contamination, based on simulated galaxies with the same stellar mass. The highest contamination is seen in the  $z = 12.5$  GSMF, for the  $10^{7.5} < M_*/M_\odot \leq 10^{8.5}$  bin, and results in several galaxies being removed from our fiducial GSMF estimate. As the predictions of **JAGUAR**

**Table 6.** Schechter function parameters for the GSMF at  $9.5 \leq z \leq 11.5$  for each of the alternative models shown in § 6.5.6. For  $\alpha$ ,  $M^*$  and  $\log_{10} \phi^*$  we give both the median posterior and maximum likelihood values (in brackets). The details of the **Bagpipes** and **Prospector** configurations for each model are given in § 4.1 and § 4.2.

SED Fitting Tool	SFH Model	IMF	$\alpha$	$M^*$	$\log_{10} \phi^*$
Bagpipes	“continuity bursty”	Kroupa (2001)	$-1.93^{+0.21}_{-0.16}$ (−1.80)	$10.70^{+1.21}_{-1.06}$ (9.70)	$-5.94^{+1.33}_{-1.28}$ (−4.70)
Prospector	“continuity bursty”	Kroupa (2001)	$-1.72^{+0.26}_{-0.18}$ (−1.51)	$10.51^{+1.34}_{-0.99}$ (9.54)	$-5.57^{+1.13}_{-1.19}$ (−4.46)
Prospector	delayed- $\tau$	Kroupa (2001)	$-1.98^{+0.22}_{-0.17}$ (−1.89)	$10.67^{+1.22}_{-1.07}$ (9.68)	$-6.22^{+1.37}_{-1.35}$ (−4.98)
Prospector	“continuity bursty”	HOT 45K	$-1.93^{+0.25}_{-0.20}$ (−1.81)	$10.56^{+1.28}_{-1.10}$ (9.53)	$-6.09^{+1.39}_{-1.39}$ (−4.83)
Prospector	delayed- $\tau$	HOT 45K	$-2.19^{+0.25}_{-0.22}$ (−2.18)	$10.54^{+1.14}_{-1.10}$ (9.55)	$-6.67^{+1.63}_{-1.45}$ (−5.31)

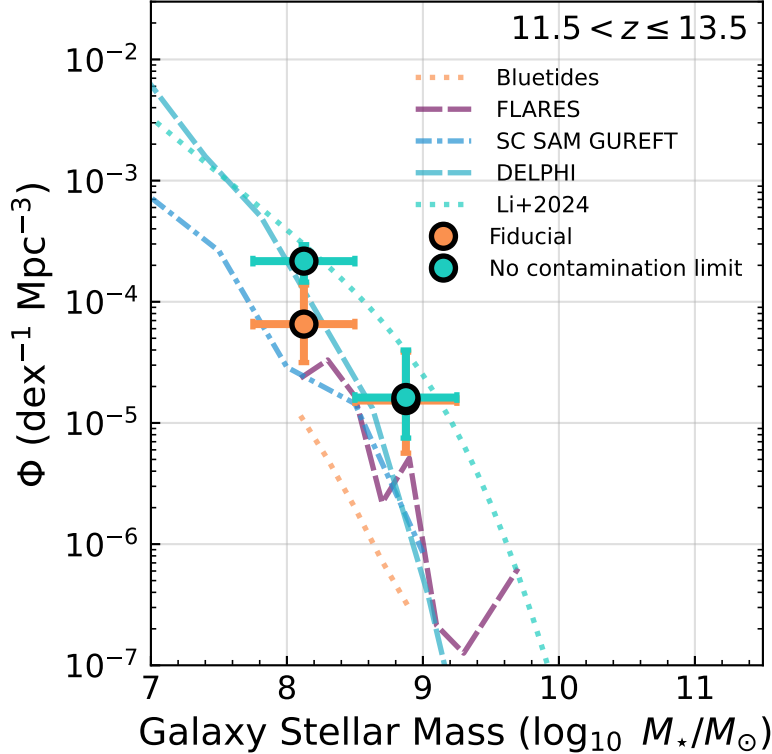


**Figure 15.** Galaxy Stellar Mass Function at  $11.5 < z \leq 13.5$  without a 50% contamination limit, compared to our fiducial **Bagpipes** results.

are uncertain at these redshifts, it is hard to judge how accurate our contamination predictions are. In Figure 15 we have recomputed the  $z = 12.5$  GSMF with no contamination limit, which boosts the lower stellar mass bin by  $\sim 0.3$  dex. This brings it closer to the predictions of Li et al. (2023)’s Feedback Free Model (FFB), which has higher star formation efficiency than most models. The FFB model shown is for  $\epsilon_{\max} = 0.20$  specifically, and the models with higher SFE ( $\epsilon_{\max} = 0.5 - 1$ ) overpredict the GSMF at this redshift compared to our observations. If our contamination is over-estimated in this redshift bin, then the FFB model of Li et al. (2023) or Mauerhofer & Dayal (2023)’s DELPHI model provide the closest predictions, suggesting high but not extreme star formation efficiency is required to produce the observed GSMF at this redshift.



## REFERENCES

- Adams, N. J., Conselice, C. J., Ferreira, L., et al. 2023, *MNRAS*, 518, 4755, doi: [10.1093/mnras/stac3347](https://doi.org/10.1093/mnras/stac3347)
- Adams, N. J., Conselice, C. J., Austin, D., et al. 2023, arXiv preprint arXiv:2304.13721
- Akins, H. B., Casey, C. M., Allen, N., et al. 2023, arXiv preprint arXiv:2304.12347
- Arrabal Haro, P., Dickinson, M., Finkelstein, S. L., et al. 2023, arXiv e-prints, arXiv:2304.05378, doi: [10.48550/arXiv.2304.05378](https://doi.org/10.48550/arXiv.2304.05378)
- Arrabal Haro, P., Dickinson, M., Finkelstein, S. L., et al. 2023, *Nature*, 622, 707
- Arrabal Haro, P., Dickinson, M., Finkelstein, S. L., et al. 2023, arXiv e-prints, arXiv:2303.15431, doi: [10.48550/arXiv.2303.15431](https://doi.org/10.48550/arXiv.2303.15431)
- Asada, Y., Sawicki, M., Abraham, R., et al. 2023, *Monthly Notices of the Royal Astronomical Society*, stad3902
- Astropy Collaboration, Robitaille, T. P., Tollerud, E. J., et al. 2013, *A&A*, 558, A33, doi: [10.1051/0004-6361/201322068](https://doi.org/10.1051/0004-6361/201322068)
- Astropy Collaboration, Price-Whelan, A. M., Sipőcz, B. M., et al. 2018, *AJ*, 156, 123, doi: [10.3847/1538-3881/aabc4f](https://doi.org/10.3847/1538-3881/aabc4f)
- Astropy Collaboration, Price-Whelan, A. M., Lim, P. L., et al. 2022a, *apj*, 935, 167, doi: [10.3847/1538-4357/ac7c74](https://doi.org/10.3847/1538-4357/ac7c74)
- . 2022b, *ApJ*, 935, 167, doi: [10.3847/1538-4357/ac7c74](https://doi.org/10.3847/1538-4357/ac7c74)
- Atek, H., Shuntov, M., Furtak, L. J., et al. 2023, *MNRAS*, 519, 1201, doi: [10.1093/mnras/stac3144](https://doi.org/10.1093/mnras/stac3144)
- Austin, D., Adams, N., Conselice, C., et al. 2023, arXiv preprint arXiv:2302.04270
- Bagley, M. B., Pirzkal, N., Finkelstein, S. L., et al. 2023a, arXiv e-prints, arXiv:2302.05466, doi: [10.48550/arXiv.2302.05466](https://doi.org/10.48550/arXiv.2302.05466)
- Bagley, M. B., Finkelstein, S. L., Koekemoer, A. M., et al. 2023b, *ApJL*, 946, L12, doi: [10.3847/2041-8213/acbb08](https://doi.org/10.3847/2041-8213/acbb08)
- Barro, G., Perez-Gonzalez, P. G., Kocevski, D. D., et al. 2023, arXiv e-prints, arXiv:2305.14418, doi: [10.48550/arXiv.2305.14418](https://doi.org/10.48550/arXiv.2305.14418)
- Behroozi, P., Wechsler, R. H., Hearin, A. P., & Conroy, C. 2019, *MNRAS*, 488, 3143, doi: [10.1093/mnras/stz1182](https://doi.org/10.1093/mnras/stz1182)
- Bertin, E., & Arnouts, S. 1996, *A&AS*, 117, 393
- Bezanson, R., Labbe, I., Whitaker, K. E., et al. 2022, arXiv e-prints, arXiv:2212.04026, doi: [10.48550/arXiv.2212.04026](https://doi.org/10.48550/arXiv.2212.04026)
- Bhatawdekar, R., Conselice, C. J., Margalef-Bentabol, B., & Duncan, K. 2019, *Monthly Notices of the Royal Astronomical Society*, 486, 3805
- Bhowmick, A. K., Di Matteo, T., Feng, Y., & Lanusse, F. 2018, *Monthly Notices of the Royal Astronomical Society*, 474, 5393
- Bhowmick, A. K., Somerville, R. S., Di Matteo, T., et al. 2020, *MNRAS*, 496, 754, doi: [10.1093/mnras/staa1605](https://doi.org/10.1093/mnras/staa1605)
- Bouwens, R., Illingworth, G., Oesch, P., et al. 2023, *Monthly Notices of the Royal Astronomical Society*, 523, 1009
- Bouwens, R., Oesch, P., Labbé, I., et al. 2016, *The Astrophysical Journal*, 830, 67
- Bouwens, R. J., Illingworth, G. D., Oesch, P. A., et al. 2015, *ApJ*, 803, 1, doi: [10.1088/0004-637X/803/1/34](https://doi.org/10.1088/0004-637X/803/1/34)
- Bowler, R. A. A., Inami, H., Sommovigo, L., et al. 2023, arXiv e-prints, arXiv:2309.17386, doi: [10.48550/arXiv.2309.17386](https://doi.org/10.48550/arXiv.2309.17386)
- Bowman, J. D., Rogers, A. E., Monsalve, R. A., Mozdzen, T. J., & Mahesh, N. 2018, *Nature*, 555, 67
- Boylan-Kolchin, M. 2023, *Nature Astronomy*, 1
- Bradač, M., Ryan, R., Casertano, S., et al. 2014, *The Astrophysical Journal*, 785, 108
- Bradley, L., Sipőcz, B., Robitaille, T., et al. 2022, Zenodo, doi: [10.5281/zenodo.6825092](https://doi.org/10.5281/zenodo.6825092)
- Brammer, G. B., van Dokkum, P. G., & Coppi, P. 2008, *The Astrophysical Journal*, 686, 1503
- Brinchmann, J., & Ellis, R. S. 2000, *ApJL*, 536, L77, doi: [10.1086/312738](https://doi.org/10.1086/312738)
- Brown, A. G., Vallenari, A., Prusti, T., et al. 2021, *Astronomy & Astrophysics*, 649, A1
- Bruzual, G., & Charlot, S. 2003, *Monthly Notices of the Royal Astronomical Society*, 344, 1000, doi: [10.1046/j.1365-8711.2003.06897.x](https://doi.org/10.1046/j.1365-8711.2003.06897.x)
- Buchner, J. 2016, *Astrophysics Source Code Library*, ascl
- Bundy, K., Ellis, R. S., Conselice, C. J., et al. 2006, *ApJ*, 651, 120, doi: [10.1086/507456](https://doi.org/10.1086/507456)
- Bunker, A. J., Cameron, A. J., Curtis-Lake, E., et al. 2023a, arXiv e-prints. <https://arxiv.org/abs/2306.02467v1>
- Bunker, A. J., Saxena, A., Cameron, A. J., et al. 2023b, arXiv preprint arXiv:2302.07256
- Bushouse, H., Eisenhamer, J., Dencheva, N., et al. 2022, *JWST Calibration Pipeline*, 1.8.2, Zenodo, doi: [10.5281/zenodo.7325378](https://doi.org/10.5281/zenodo.7325378)
- Calzetti, D., Armus, L., Bohlin, R. C., et al. 2000, *The Astrophysical Journal*, 533, 682
- Cameron, A. J., Katz, H., Witten, C., et al. 2023, *Nebular dominated galaxies in the early Universe with top-heavy stellar initial mass functions.* <https://arxiv.org/abs/2311.02051>
- Caputi, K., Ilbert, O., Laigle, C., et al. 2015, *The Astrophysical Journal*, 810, 73
- Carnall, A. C., Leja, J., Johnson, B. D., et al. 2019, *The Astrophysical Journal*, 873, 44

- Carnall, A. C., McLure, R. J., Dunlop, J. S., & Davé, R. 2018, *Monthly Notices of the Royal Astronomical Society*, 480, 4379, doi: [10.1093/mnras/sty2169](https://doi.org/10.1093/mnras/sty2169)
- Castellano, M., Fontana, A., Treu, T., et al. 2022, *ApJL*, 938, L15, doi: [10.3847/2041-8213/ac94d0](https://doi.org/10.3847/2041-8213/ac94d0)
- Chabrier, G., Baraffe, I., Allard, F., & Hauschildt, P. 2000, *ApJ*, 542, 464, doi: [10.1086/309513](https://doi.org/10.1086/309513)
- Charlot, S., & Fall, S. M. 2000, *The Astrophysical Journal*, 539, 718
- Chevallard, J., & Charlot, S. 2016, *Monthly Notices of the Royal Astronomical Society*, 462, 1415
- Choi, J., Dotter, A., Conroy, C., et al. 2016, *The Astrophysical Journal*, 823, 102
- Clauwens, B., Schaye, J., & Franx, M. 2016, *Monthly Notices of the Royal Astronomical Society*, 462, 2832
- Cleveland, W. S. 1979, *Journal of the American statistical association*, 74, 829
- Conroy, C., & Gunn, J. E. 2010, *Astrophysics Source Code Library*, ascl
- Cullen, F., McLure, R., McLeod, D., et al. 2023, *Monthly Notices of the Royal Astronomical Society*, 520, 14
- Curti, M., d'Eugenio, F., Carniani, S., et al. 2023, *Monthly Notices of the Royal Astronomical Society*, 518, 425
- Curtis-Lake, E., Carniani, S., Cameron, A., et al. 2023, *Nature Astronomy*, doi: [10.1038/s41550-023-01918-w](https://doi.org/10.1038/s41550-023-01918-w)
- Davidzon, I., Ilbert, O., Laigle, C., et al. 2017, *Astronomy & Astrophysics*, 605, A70
- Davis, M., Guhathakurta, P., Konidaris, N. P., et al. 2007, *The Astrophysical Journal*, 660, L1
- Dome, T., Tacchella, S., Fialkov, A., et al. 2024, *Monthly Notices of the Royal Astronomical Society*, 527, 2139
- Donnan, C. T., McLeod, D. J., Dunlop, J. S., et al. 2022, *arXiv*, 000, arXiv:2207.12356. <https://ui.adsabs.harvard.edu/abs/2022arXiv220712356D/abstract>
- Dotter, A. 2016, *The Astrophysical Journal Supplement Series*, 222, 8
- Drakos, N. E., Villaseñor, B., Robertson, B. E., et al. 2022, *ApJ*, 926, 194, doi: [10.3847/1538-4357/ac46fb](https://doi.org/10.3847/1538-4357/ac46fb)
- Dressler, A., Rieke, M., Eisenstein, D., et al. 2023, *arXiv e-prints*. <https://arxiv.org/abs/2306.02469v1>
- Driver, S. P., & Robotham, A. S. G. 2010, *MNRAS*, 407, 2131, doi: [10.1111/j.1365-2966.2010.17028.x](https://doi.org/10.1111/j.1365-2966.2010.17028.x)
- Driver, S. P., Andrews, S. K., da Cunha, E., et al. 2018, *MNRAS*, 475, 2891, doi: [10.1093/mnras/stx2728](https://doi.org/10.1093/mnras/stx2728)
- Duncan, K., Conselice, C. J., Mortlock, A., et al. 2014, *Monthly Notices of the Royal Astronomical Society*, 444, 2960
- Dunlop, J. S., Abraham, R. G., Ashby, M. L. N., et al. 2021, *PRIMER: Public Release IMaging for Extragalactic Research*, JWST Proposal. Cycle 1, ID. #1837
- D'Silva, J. C., Driver, S. P., Lagos, C. D., et al. 2023, *The Astrophysical Journal Letters*, 959, L18
- Eddington, A. 1913, *Monthly Notices of the Royal Astronomical Society*, 73, 359
- Eisenstein, D. J., Willott, C., Alberts, S., et al. 2023a, *arXiv e-prints*, arXiv:2306.02465, doi: [10.48550/arXiv.2306.02465](https://doi.org/10.48550/arXiv.2306.02465)
- Eisenstein, D. J., Johnson, B. D., Robertson, B., et al. 2023b, *arXiv e-prints*, arXiv:2310.12340, doi: [10.48550/arXiv.2310.12340](https://doi.org/10.48550/arXiv.2310.12340)
- Endsley, R., Stark, D. P., Chevallard, J., & Charlot, S. 2021, *Monthly Notices of the Royal Astronomical Society*, 500, 5229
- Endsley, R., Stark, D. P., Whitler, L., et al. 2023a, *MNRAS*, 000, 1. <https://arxiv.org/abs/2306.05295v1>
- Endsley, R., Stark, D. P., Lyu, J., et al. 2023b, *Monthly Notices of the Royal Astronomical Society*, 520, 4609
- Faucher-Giguère, C.-A. 2018, *Monthly Notices of the Royal Astronomical Society*, 473, 3717
- Feng, Y., Di-Matteo, T., Croft, R. A., et al. 2016, *MNRAS*, 455, 2778, doi: [10.1093/mnras/stv2484](https://doi.org/10.1093/mnras/stv2484)
- Ferland, G. J., Chatzikos, M., Guzmán, F., et al. 2017, *RMxAA*, 53, 385, doi: [10.48550/arXiv.1705.10877](https://doi.org/10.48550/arXiv.1705.10877)
- Feroz, F., Hobson, M., & Bridges, M. 2009, *Monthly Notices of the Royal Astronomical Society*, 398, 1601
- Ferreira, L., Adams, N., Conselice, C. J., et al. 2022, *arXiv e-prints*, arXiv:2207.09428. <https://arxiv.org/abs/2207.09428>
- Ferreira, L., Conselice, C. J., Sazonova, E., et al. 2023, *The Astrophysical Journal*, 955, 94
- Finkelstein, S. L., Bagley, M., Song, M., et al. 2022, *The Astrophysical Journal*, 928, 52, doi: [10.3847/1538-4357/ac3aed](https://doi.org/10.3847/1538-4357/ac3aed)
- Finkelstein, S. L., Bagley, M. B., Ferguson, H. C., et al. 2023a, *ApJL*, 946, L13, doi: [10.3847/2041-8213/acade4](https://doi.org/10.3847/2041-8213/acade4)
- Finkelstein, S. L., Leung, G. C. K., Bagley, M. B., et al. 2023b, *arXiv e-prints*, arXiv:2311.04279, doi: [10.48550/arXiv.2311.04279](https://doi.org/10.48550/arXiv.2311.04279)
- Foreman-Mackey, D., Hogg, D. W., Lang, D., & Goodman, J. 2013, *PASP*, 125, 306, doi: [10.1086/670067](https://doi.org/10.1086/670067)
- Fujimoto, S., Finkelstein, S. L., Burgarella, D., et al. 2022, *arXiv preprint arXiv:2211.03896*
- Fujimoto, S., Arrabal Haro, P., Dickinson, M., et al. 2023, *arXiv e-prints*, arXiv:2301.09482, doi: [10.48550/arXiv.2301.09482](https://doi.org/10.48550/arXiv.2301.09482)
- Furlong, M., Bower, R. G., Theuns, T., et al. 2015, *MNRAS*, 450, 4486, doi: [10.1093/mnras/stv852](https://doi.org/10.1093/mnras/stv852)
- Furtak, L. J., Atek, H., Lehnert, M. D., Chevallard, J., & Charlot, S. 2021, *MNRAS*, 501, 1568, doi: [10.1093/mnras/staa3760](https://doi.org/10.1093/mnras/staa3760)

- Furtak, L. J., Shuntov, M., Atek, H., et al. 2023, *MNRAS*, 519, 3064, doi: [10.1093/mnras/stac3717](https://doi.org/10.1093/mnras/stac3717)
- Furtak, L. J., Zitrin, A., Plat, A., et al. 2023, *The Astrophysical Journal*, 952, 142
- Furtak, L. J., Labbé, I., Zitrin, A., et al. 2023, arXiv e-prints, arXiv:2308.05735, doi: [10.48550/arXiv.2308.05735](https://doi.org/10.48550/arXiv.2308.05735)
- Gaia Collaboration, Brown, A. G. A., Vallenari, A., et al. 2018, *A&A*, 616, A1, doi: [10.1051/0004-6361/201833051](https://doi.org/10.1051/0004-6361/201833051)
- Genel, S., Vogelsberger, M., Springel, V., et al. 2014, *MNRAS*, 445, 175, doi: [10.1093/mnras/stu1654](https://doi.org/10.1093/mnras/stu1654)
- Giménez-Arteaga, C., Oesch, P. A., Brammer, G. B., et al. 2023, *ApJ*, 948, 126, doi: [10.3847/1538-4357/acc5ea](https://doi.org/10.3847/1538-4357/acc5ea)
- Giménez-Arteaga, C., Fujimoto, S., Valentino, F., et al. 2024, Outshining in the Spatially Resolved Analysis of a Strongly-Lensed Galaxy at  $z=6.072$  with JWST NIRCam. <https://arxiv.org/abs/2402.17875>
- Gottumukkala, R., Barrufet, L., Oesch, P., et al. 2023, arXiv preprint arXiv:2310.03787
- Grazian, A., Castellano, M., Fontana, A., et al. 2012, *A&A*, 547, A51, doi: [10.1051/0004-6361/201219669](https://doi.org/10.1051/0004-6361/201219669)
- Grazian, A., Fontana, A., Santini, P., et al. 2015, *Astronomy & Astrophysics*, 575, A96
- Greene, J. E., Labbe, I., Goulding, A. D., et al. 2023, arXiv preprint arXiv:2309.05714
- Griffiths, A., Conselice, C. J., Alpaslan, M., et al. 2018, *Monthly Notices of the Royal Astronomical Society*, 475, 2853
- Grogin, N. A., Kocevski, D. D., Faber, S. M., et al. 2011, *ApJS*, 197, 35, doi: [10.1088/0067-0049/197/2/35](https://doi.org/10.1088/0067-0049/197/2/35)
- Gunawardhana, M. L., Hopkins, A. M., Sharp, R. G., et al. 2011, *Monthly Notices of the Royal Astronomical Society*, 415, 1647
- Hainline, K. N., Johnson, B. D., Robertson, B., et al. 2023, arXiv e-prints, arXiv:2306.02468, doi: [10.48550/arXiv.2306.02468](https://doi.org/10.48550/arXiv.2306.02468)
- Hainline, K. N., Helton, J. M., Johnson, B. D., et al. 2023, Brown Dwarf Candidates in the JADES and CEERS Extragalactic Surveys. <https://arxiv.org/abs/2309.03250>
- Harikane, Y., Ouchi, M., Ono, Y., et al. 2016, *The Astrophysical Journal*, 821, 123
- Harikane, Y., Ouchi, M., Oguri, M., et al. 2023, *ApJS*, 265, 5, doi: [10.3847/1538-4365/acaaa9](https://doi.org/10.3847/1538-4365/acaaa9)
- Haslbauer, M., Kroupa, P., Zonoozi, A. H., & Hagi, H. 2022, Has JWST already falsified dark-matter-driven galaxy formation?, arXiv, doi: [10.48550/ARXIV.2210.14915](https://doi.org/10.48550/ARXIV.2210.14915)
- Hoffmann, S. L., Mack, J., Avila, R., et al. 2021, in *American Astronomical Society Meeting Abstracts*, Vol. 53, American Astronomical Society Meeting Abstracts, 216.02
- Hopkins, P. F., Hernquist, L., Cox, T. J., et al. 2005, *ApJ*, 630, 716, doi: [10.1086/432463](https://doi.org/10.1086/432463)
- Hunter, J. D. 2007, *Computing in Science & Engineering*, 9, 90, doi: [10.1109/MCSE.2007.55](https://doi.org/10.1109/MCSE.2007.55)
- Illingworth, G., Magee, D., Bouwens, R., et al. 2016, arXiv e-prints, arXiv:1606.00841, doi: [10.48550/arXiv.1606.00841](https://doi.org/10.48550/arXiv.1606.00841)
- Jaacks, J., Finkelstein, S. L., & Bromm, V. 2019, *Monthly Notices of the Royal Astronomical Society*, 488, 2202
- Jain, S., Tacchella, S., & Mosleh, M. 2024, *Monthly Notices of the Royal Astronomical Society*, 527, 3291
- Jansen, R. A., & Windhorst, R. A. 2018, *PASP*, 130, 124001, doi: [10.1088/1538-3873/aae476](https://doi.org/10.1088/1538-3873/aae476)
- Jermyn, A. S., Steinhardt, C. L., & Tout, C. A. 2018, *Monthly Notices of the Royal Astronomical Society*, 480, 4265, doi: [10.1093/MNRAS/STY2123](https://doi.org/10.1093/MNRAS/STY2123)
- Jespersen, C. K., Steinhardt, C. L., Somerville, R. S., & Lovell, C. C. 2024, On the Significance of Rare Objects at High Redshift: The Impact of Cosmic Variance. <https://arxiv.org/abs/2403.00050>
- Johnson, B., Foreman-Mackey, D., Sick, J., et al. 2023, *Zenodo*
- Johnson, B. D., Leja, J., Conroy, C., & Speagle, J. S. 2021, *ApJS*, 254, 22, doi: [10.3847/1538-4365/abef67](https://doi.org/10.3847/1538-4365/abef67)
- Kartaltepe, J., Casey, C. M., Bagley, M., et al. 2021, COSMOS-Webb: The Webb Cosmic Origins Survey, JWST Proposal. Cycle 1, ID. #1727
- Katz, H., Rosdahl, J., Kimm, T., et al. 2022, *Monthly Notices of the Royal Astronomical Society*, 510, 5603
- Kikuchihara, S., Ouchi, M., Ono, Y., et al. 2020, *The Astrophysical Journal*, 893, 60
- Kocevski, D. D., Onoue, M., Inayoshi, K., et al. 2023, arXiv preprint arXiv:2302.00012
- Koekemoer, A. M., Faber, S. M., Ferguson, H. C., et al. 2011, *ApJS*, 197, 36, doi: [10.1088/0067-0049/197/2/36](https://doi.org/10.1088/0067-0049/197/2/36)
- Kokorev, V., Caputi, K. I., Greene, J. E., et al. 2024, arXiv e-prints, arXiv:2401.09981. <https://arxiv.org/abs/2401.09981>
- Kroupa, P. 2001, *Monthly Notices of the Royal Astronomical Society*, 322, 231
- Kroupa, P. 2002, *Science*, 295, 82, doi: [10.1126/science.1067524](https://doi.org/10.1126/science.1067524)
- Labbé, I., van Dokkum, P., Nelson, E., et al. 2023, *Nature*, 616, 266, doi: [10.1038/s41586-023-05786-2](https://doi.org/10.1038/s41586-023-05786-2)
- Labbe, I., Greene, J. E., Bezanson, R., et al. 2023, arXiv preprint arXiv:2306.07320

- Laigle, C., McCracken, H. J., Ilbert, O., et al. 2016, *The Astrophysical Journal Supplement Series*, 224, 24
- Langeroodi, D., Hjorth, J., Chen, W., et al. 2023, *The Astrophysical Journal*, 957, 39
- Larson, R. L., Hutchison, T. A., Bagley, M., et al. 2022, arXiv, doi: [10.48550/arxiv.2211.10035](https://arxiv.org/abs/10.48550/arxiv.2211.10035)
- Larson, R. L., Finkelstein, S. L., Kocevski, D. D., et al. 2023, *The Astrophysical Journal Letters*, 953, L29
- Laseter, I. H., Maseda, M. V., Curti, M., et al. 2023, arXiv e-prints. <https://arxiv.org/abs/2306.03120v1>
- Leja, J., Carnall, A. C., Johnson, B. D., Conroy, C., & Speagle, J. S. 2019, *The Astrophysical Journal*, 876, 3
- Leja, J., Johnson, B. D., Conroy, C., & van Dokkum, P. 2018, *ApJ*, 854, 62, doi: [10.3847/1538-4357/aaa8db](https://doi.org/10.3847/1538-4357/aaa8db)
- Leung, G. C. K., Bagley, M. B., Finkelstein, S. L., et al. 2023, *ApJL*, 954, L46, doi: [10.3847/2041-8213/acf365](https://doi.org/10.3847/2041-8213/acf365)
- Li, Z., Dekel, A., Sarkar, K. C., et al. 2023, arXiv preprint arXiv:2311.14662
- Looser, T. J., D’eugenio, F., Maiolino, R., et al. 2023, arXiv e-prints. <https://arxiv.org/abs/2306.02470v1>
- Lovell, C. C., Harrison, I., Harikane, Y., Tacchella, S., & Wilkins, S. M. 2023, *Monthly Notices of the Royal Astronomical Society*, 518, 2511
- Lovell, C. C., Vijayan, A. P., Thomas, P. A., et al. 2021, *MNRAS*, 500, 2127, doi: [10.1093/mnras/staa3360](https://doi.org/10.1093/mnras/staa3360)
- Lower, S., Narayanan, D., Leja, J., et al. 2020, *The Astrophysical Journal*, 904, 33
- Ma, X., Hopkins, P. F., Garrison-Kimmel, S., et al. 2018, *MNRAS*, 478, 1694, doi: [10.1093/mnras/sty1024](https://doi.org/10.1093/mnras/sty1024)
- Madau, P. 1995, *The Astrophysical Journal*, 441, 18
- Madau, P., & Dickinson, M. 2014, *Annual Review of Astronomy and Astrophysics*, 52, 415, doi: [10.1146/annurev-astro-081811-125615](https://doi.org/10.1146/annurev-astro-081811-125615)
- Madau, P., & Haardt, F. 2015, *ApJL*, 813, L8, doi: [10.1088/2041-8205/813/1/L8](https://doi.org/10.1088/2041-8205/813/1/L8)
- Marley, M., Saumon, D., Morley, C., et al. 2021, Zenodo, doi: [10.5281/zenodo.5063476](https://doi.org/10.5281/zenodo.5063476)
- Mason, C. A., Trenti, M., & Treu, T. 2023, *Monthly Notices of the Royal Astronomical Society*, 521, 497
- Matthee, J., Naidu, R. P., Brammer, G., et al. 2023, arXiv preprint arXiv:2306.05448
- Mauerhofer, V., & Dayal, P. 2023, *Monthly Notices of the Royal Astronomical Society*, 526, 2196
- McLeod, D. J., Donnan, C. T., McLure, R. J., et al. 2023, *MNRAS*, doi: [10.1093/mnras/stad3471](https://doi.org/10.1093/mnras/stad3471)
- Menanteau, F., Hughes, J. P., Sifón, C., et al. 2012, *ApJ*, 748, 7, doi: [10.1088/0004-637X/748/1/7](https://doi.org/10.1088/0004-637X/748/1/7)
- Mortlock, A., Conselice, C. J., Bluck, A. F. L., et al. 2011, *MNRAS*, 413, 2845, doi: [10.1111/j.1365-2966.2011.18357.x](https://doi.org/10.1111/j.1365-2966.2011.18357.x)
- Mortlock, A., Conselice, C. J., Hartley, W. G., et al. 2015, *MNRAS*, 447, 2, doi: [10.1093/mnras/stu2403](https://doi.org/10.1093/mnras/stu2403)
- Moster, B. P., Somerville, R. S., Maulbetsch, C., et al. 2010, *ApJ*, 710, 903, doi: [10.1088/0004-637X/710/2/903](https://doi.org/10.1088/0004-637X/710/2/903)
- Moster, B. P., Somerville, R. S., Newman, J. A., & Rix, H.-W. 2011, *ApJ*, 731, 113, doi: [10.1088/0004-637X/731/2/113](https://doi.org/10.1088/0004-637X/731/2/113)
- Mowla, L., Iyer, K., Asada, Y., et al. 2024, arXiv e-prints, arXiv:2402.08696, doi: [10.48550/arXiv.2402.08696](https://doi.org/10.48550/arXiv.2402.08696)
- Mutch, S. J., Geil, P. M., Poole, G. B., et al. 2016, *Monthly Notices of the Royal Astronomical Society*, 462, 250
- Naidu, R. P., Oesch, P. A., van Dokkum, P., et al. 2022, *The Astrophysical Journal Letters*, 940, L14
- Naidu, R. P., Oesch, P. A., Setton, D. J., et al. 2022, arXiv e-prints, arXiv:2208.02794. <https://arxiv.org/abs/2208.02794>
- Nanayakkara, T., Glazebrook, K., Jacobs, C., et al. 2022, 11, doi: [10.48550/arxiv.2207.13860](https://doi.org/10.48550/arxiv.2207.13860)
- Narayanan, D., Lower, S., Torrey, P., et al. 2023, Outshining by Recent Star Formation Prevents the Accurate Measurement of High-z Galaxy Stellar Masses. <https://arxiv.org/abs/2306.10118>
- Navarro-Carrera, R., Rinaldi, P., Caputi, K. I., et al. 2023, arXiv preprint arXiv:2305.16141
- Noboriguchi, A., Inoue, A. K., Nagao, T., Toba, Y., & Misawa, T. 2023, *The Astrophysical Journal Letters*, 959, L14
- Norgaard-Nielsen, H. U., & Perez-Gonzalez, P. G. 2017, *The MIRI HUDF Deep Imaging Survey, JWST Proposal. Cycle 1, ID. #1283*
- O’Brien, R., Jansen, R. A., Grogin, N. A., et al. 2024, arXiv preprint arXiv:2401.04944
- Oesch, P., Bouwens, R., Illingworth, G., et al. 2014, *The Astrophysical Journal*, 786, 108
- Oesch, P. A., Bouwens, R. J., Illingworth, G. D., Labbé, I., & Stefanon, M. 2018, *ApJ*, 855, 105, doi: [10.3847/1538-4357/aab03f](https://doi.org/10.3847/1538-4357/aab03f)
- Oke, J. B. 1974, *ApJS*, 27, 21, doi: [10.1086/190287](https://doi.org/10.1086/190287)
- Oke, J. B., & Gunn, J. E. 1983, *ApJ*, 266, 713, doi: [10.1086/160817](https://doi.org/10.1086/160817)
- Ormerod, K., Conselice, C., Adams, N., et al. 2024, *Monthly Notices of the Royal Astronomical Society*, 527, 6110
- Papadopoulos, P. P., Thi, W.-F., Miniati, F., & Viti, S. 2011, *Monthly Notices of the Royal Astronomical Society*, 414, 1705
- Papovich, C., Cole, J., Yang, G., et al. 2022, arXiv preprint arXiv:2301.00027
- Pérez-González, P. G., Costantin, L., Langeroodi, D., et al. 2023, arXiv preprint arXiv:2302.02429

- Pérez-González, P. G., Barro, G., Annunziatella, M., et al. 2023, *ApJL*, 946, L16, doi: [10.3847/2041-8213/acb3a5](https://doi.org/10.3847/2041-8213/acb3a5)
- Pérez-González, P. G., Barro, G., Rieke, G. H., et al. 2024, arXiv preprint arXiv:2401.08782
- Perrin, M. D., Sivaramakrishnan, A., Lajoie, C.-P., et al. 2014, in *Space Telescopes and Instrumentation 2014: Optical, Infrared, and Millimeter Wave*, Vol. 9143, SPIE, 1174–1184
- Perrin, M. D., Soummer, R., Elliott, E. M., Lallo, M. D., & Sivaramakrishnan, A. 2012, in *Space Telescopes and Instrumentation 2012: Optical, Infrared, and Millimeter Wave*, Vol. 8442, SPIE, 1193–1203
- Planck Collaboration, Ade, P. A. R., Aghanim, N., et al. 2016, *A&A*, 594, A13, doi: [10.1051/0004-6361/201525830](https://doi.org/10.1051/0004-6361/201525830)
- Pontoppidan, K. M., Barrientes, J., Blome, C., et al. 2022, *The Astrophysical Journal Letters*, 936, L14
- Popesso, P., Concas, A., Cresci, G., et al. 2023, *Monthly Notices of the Royal Astronomical Society*, 519, 1526
- Retzlaff, J., Rosati, P., Dickinson, M., et al. 2010, *Astronomy & Astrophysics*, 511, A50
- Rieke, M. J., Kelly, D. M., Misselt, K., et al. 2022, arXiv preprint arXiv:2212.12069
- Rieke, M. J., Robertson, B., Tacchella, S., et al. 2023, *The Astrophysical Journal Supplement Series*, 269, 16
- Roberts-Borsani, G., Bouwens, R., Oesch, P., et al. 2016, *The Astrophysical Journal*, 823, 143
- Robertson, B., Johnson, B. D., Tacchella, S., et al. 2023a, arXiv e-prints, arXiv:2312.10033, doi: [10.48550/arXiv.2312.10033](https://doi.org/10.48550/arXiv.2312.10033)
- Robertson, B. E., Tacchella, S., Johnson, B. D., et al. 2023b, *Nature Astronomy*, 7, 611, doi: [10.1038/s41550-023-01921-1](https://doi.org/10.1038/s41550-023-01921-1)
- Robotham, A. S., Norberg, P., Driver, S. P., et al. 2011, *Monthly Notices of the Royal Astronomical Society*, 416, 2640
- Roper, W. J., Lovell, C. C., Vijayan, A. P., et al. 2022, *Monthly Notices of the Royal Astronomical Society*, 514, 1921
- Rowan-Robinson, M., & McCrea, W. 1968, *Monthly Notices of the Royal Astronomical Society*, 138, 445
- Salim, S., Boquien, M., & Lee, J. C. 2018, *ApJ*, 859, 11, doi: [10.3847/1538-4357/aabf3c](https://doi.org/10.3847/1538-4357/aabf3c)
- Salpeter, E. E. 1955, *Astrophysical Journal*, vol. 121, p. 161, 121, 161
- Santini, P., Fontana, A., Castellano, M., et al. 2022, arXiv, arXiv:2207.11379. <https://ui.adsabs.harvard.edu/abs/2022arXiv220711379S/abstract>
- Schaye, J., Crain, R. A., Bower, R. G., et al. 2015, *MNRAS*, 446, 521, doi: [10.1093/mnras/stu2058](https://doi.org/10.1093/mnras/stu2058)
- Schechter, P. 1976, *ApJ*, 203, 297, doi: [10.1086/154079](https://doi.org/10.1086/154079)
- Schlawin, E., Leisenring, J., Misselt, K., et al. 2020, *AJ*, 160, 231, doi: [10.3847/1538-3881/abb811](https://doi.org/10.3847/1538-3881/abb811)
- Schmidt, M. 1968, *The Astrophysical Journal*, 151, 393
- Shen, X., Vogelsberger, M., Boylan-Kolchin, M., Tacchella, S., & Kannan, R. 2023, *Monthly Notices of the Royal Astronomical Society*, 525, 3254
- Shen, X., Vogelsberger, M., Borrow, J., et al. 2024, arXiv preprint arXiv:2402.08717
- Smail, I., Dudzevičiūtė, U., Gurwell, M., et al. 2023, *The Astrophysical Journal*, 958, 36
- Sneppen, A., Steinhardt, C. L., Hensley, H., et al. 2022, *ApJ*, 931, 57, doi: [10.3847/1538-4357/ac695e](https://doi.org/10.3847/1538-4357/ac695e)
- Song, M., Finkelstein, S. L., Ashby, M. L. N., et al. 2016, *ApJ*, 825, 5, doi: [10.3847/0004-637X/825/1/5](https://doi.org/10.3847/0004-637X/825/1/5)
- Speagle, J. S. 2020, *Monthly Notices of the Royal Astronomical Society*, 493, 3132
- Stanway, E. R., & Eldridge, J. 2018, *Monthly Notices of the Royal Astronomical Society*, 479, 75
- Stark, D. P., Schenker, M. A., Ellis, R., et al. 2013, *The Astrophysical Journal*, 763, 129
- Stefanon, M., Bouwens, R. J., Labbé, I., et al. 2021, *The Astrophysical Journal*, 922, 29
- . 2017, *The Astrophysical Journal*, 843, 36
- Steinhardt, C. L., Jespersen, C. K., & Linzer, N. B. 2021, *The Astrophysical Journal*, 923, 8, doi: [10.3847/1538-4357/ac2a2f](https://doi.org/10.3847/1538-4357/ac2a2f)
- Steinhardt, C. L., Kokorev, V., Rusakov, V., Garcia, E., & Sneppen, A. 2023, *The Astrophysical Journal Letters*, 951, L40
- Strait, V., Bradač, M., Coe, D., et al. 2020, *The Astrophysical Journal*, 888, 124
- Tacchella, S., Finkelstein, S. L., Bagley, M., et al. 2022, *The Astrophysical Journal*, 927, 170
- Tang, M., Stark, D. P., Chen, Z., et al. 2023, arXiv e-prints, arXiv:2301.07072, doi: [10.48550/arXiv.2301.07072](https://doi.org/10.48550/arXiv.2301.07072)
- Tomczak, A. R., Quadri, R. F., Tran, K.-V. H., et al. 2014, *ApJ*, 783, 85, doi: [10.1088/0004-637X/783/2/85](https://doi.org/10.1088/0004-637X/783/2/85)
- Treu, T., Calabro, A., Castellano, M., et al. 2022, arXiv, arXiv:2207.13527. <https://ui.adsabs.harvard.edu/abs/2022arXiv220713527T/abstract>
- Trussler, J. A., Adams, N. J., Conselice, C. J., et al. 2023, *Monthly Notices of the Royal Astronomical Society*, stad1629
- Ulm, K. 1990, *American Journal of Epidemiology*, 131, 373, doi: [10.1093/oxfordjournals.aje.a115507](https://doi.org/10.1093/oxfordjournals.aje.a115507)
- Vallenari, A., Brown, A., & Prusti, T. 2022, *Astronomy & Astrophysics*
- van Mierlo, S. E., Caputi, K. I., & Kokorev, V. 2023, *The Astrophysical Journal Letters*, 945, L21

- Virtanen, P., Gommers, R., Oliphant, T. E., et al. 2020, *Nature Methods*, 17, 261, doi: [10.1038/s41592-019-0686-2](https://doi.org/10.1038/s41592-019-0686-2)
- Wang, B., Fujimoto, S., Labbé, I., et al. 2023a, *The Astrophysical Journal Letters*, 957, L34
- Wang, B., Leja, J., Atek, H., et al. 2023b, arXiv preprint arXiv:2310.06781
- Wang, T., Sun, H., Zhou, L., et al. 2024, The true number density of massive galaxies in the early Universe revealed by JWST/MIRI. <https://arxiv.org/abs/2403.02399>
- Weaver, J., Davidzon, I., Toft, S., et al. 2022, arXiv preprint arXiv:2212.02512
- Weidner, C., Ferreras, I., Vazdekis, A., & La Barbera, F. 2013, *Monthly Notices of the Royal Astronomical Society*, 435, 2274
- Weigel, A. K., Schawinski, K., & Bruderer, C. 2016, *Monthly Notices of the Royal Astronomical Society*, 459, 2150, doi: [10.1093/mnras/stw756](https://doi.org/10.1093/mnras/stw756)
- Whitaker, K. E., Ashas, M., Illingworth, G., et al. 2019, *ApJS*, 244, 16, doi: [10.3847/1538-4365/ab3853](https://doi.org/10.3847/1538-4365/ab3853)
- Wilkins, S. M., Feng, Y., Di Matteo, T., et al. 2017, *MNRAS*, 469, 2517, doi: [10.1093/mnras/stx841](https://doi.org/10.1093/mnras/stx841)
- Wilkins, S. M., Turner, J. C., Bagley, M. B., et al. 2023a, arXiv e-prints, arXiv:2311.08065, doi: [10.48550/arXiv.2311.08065](https://doi.org/10.48550/arXiv.2311.08065)
- Wilkins, S. M., Vijayan, A. P., Lovell, C. C., et al. 2023b, *MNRAS*, 519, 3118, doi: [10.1093/mnras/stac3280](https://doi.org/10.1093/mnras/stac3280)
- Williams, C. C., Curtis-Lake, E., Hainline, K. N., et al. 2018, *ApJS*, 236, 33, doi: [10.3847/1538-4365/aabcb](https://doi.org/10.3847/1538-4365/aabcb)
- Willott, C. J., Desprez, G., Asada, Y., et al. 2023a, arXiv e-prints, arXiv:2311.12234, doi: [10.48550/arXiv.2311.12234](https://doi.org/10.48550/arXiv.2311.12234)
- Willott, C. J., Abraham, R. G., Asada, Y., et al. 2023b, CANUCS: The CANadian NIRISS Unbiased Cluster Survey, JWST Proposal. Cycle 3, ID. #4527
- Windhorst, R. A., Cohen, S. H., Jansen, R. A., et al. 2023, *AJ*, 165, 13, doi: [10.3847/1538-3881/aca163](https://doi.org/10.3847/1538-3881/aca163)
- Withers, S., Muzzin, A., Ravindranath, S., et al. 2023, *The Astrophysical Journal Letters*, 958, L14
- Woodrum, C., Rieke, M., Ji, Z., et al. 2023, arXiv preprint arXiv:2310.18464
- Xiao, M., Oesch, P., Elbaz, D., et al. 2023, arXiv preprint arXiv:2309.02492
- Yan, H., Ma, Z., Ling, C., Cheng, C., & Huang, J.-S. 2023, *ApJL*, 942, L9, doi: [10.3847/2041-8213/aca80c](https://doi.org/10.3847/2041-8213/aca80c)
- Yan, H., Cohen, S. H., Windhorst, R. A., et al. 2022, arXiv, arXiv:2209.04092. <https://ui.adsabs.harvard.edu/abs/2022arXiv220904092Y/abstract>
- Yung, L. Y. A., Somerville, R. S., Finkelstein, S. L., Wilkins, S. M., & Gardner, J. P. 2023, arXiv e-prints, arXiv:2304.04348, doi: [10.48550/arXiv.2304.04348](https://doi.org/10.48550/arXiv.2304.04348)
- Yung, L. Y. A., Somerville, R. S., Popping, G., et al. 2019, *MNRAS*, 490, 2855, doi: [10.1093/mnras/stz2755](https://doi.org/10.1093/mnras/stz2755)